technische universität
dortmund

Low-Field NMR Spectroscopy for Samples with Restricted Mobility

Dissertation

zur Erlangung des Doktorgrades
der Naturwissenschaften
der Fakultät Physik
der Technischen Universität Dortmund

vorgelegt von
Ahmed Bahti

2025

Angenommen von der Fakultät Physik der Technischen Universität Dortmund.

Tag der mündlichen Prüfung: 20.05.2025

Prüfungskommission:

Prof. Dr. Dieter Suter (Erstgutachter)

Dr. Roland Hergenröder (Zweitgutachter)

Prof. Dr. Doris Reiter

Dr. Jörg Debus

Dedication

To My Loving Father and Marvelous Mother

Acknowledgment

I would like to express my deepest gratitude to Prof. Dr. Dieter Suter from the Fakultät Physik, Experimentelle Physik 3 at TU Dortmund, for his inspiring guidance, constructive criticism, and invaluable suggestions throughout my research. This work would not have been possible without his help and constant encouragement. The experience gained under his supervision has been immensely beneficial for my future endeavors.

I am also sincerely thankful to my second supervisor, Dr. Roland Hergenröder, and his group members at the Leibniz-Institut für Analytische Wissenschaften (ISAS) in Dortmund, Germany. Their support during my thesis research and training, along with access to advanced instruments and laboratories, was crucial for completing my work. Dr. Hergenröder's guidance and support are greatly appreciated.

Special thanks to Dr. Ahmad Telfah from Dr. Hergenröder's group at ISAS for his substantial assistance with Nuclear Magnetic Resonance (NMR) measurements, spectral interpretations, and advanced training in NMR, which paved the way for my PhD thesis on low-field NMR systems.

I am grateful to Dr. Lubaba Migdadi, Dr. Ayten Kalfe-Yildiz, Dr. Michael Gogiashvili, Mahmoud Telfah and Qais Al Bataineh for their scientific discussions and friendship.

I extend my thanks to the Leibniz-Institut für Analytische Wissenschaften (ISAS) and TU Dortmund for the opportunity to pursue my higher education. I appreciate the support of all my current and former lab members.

Finally, I am deeply grateful to my wonderful father and mother for their unwavering support and encouragement, as well as to my wife, Nur El-Houda, for her constant love and belief in me. My sincere appreciation goes to my siblings and extended family for their unforgettable support and the warm atmosphere they have provided. I cannot adequately express my gratitude to my precious sons, Adam and Elias, for their patience, resilience, and delightful comments. This dissertation reflects the love, support, and belief my family has shown me, for which I will always be grateful.

Thank you!

Ahmed Bahti

Table of Contents

List of figures

List of tables

List of symbols and notations

Symbols	Description
NMR	Nuclear Magnetic Resonance
MRI	Magnetic Resonance Imaging
FID	Free Induction Decay
^{1}H-NMR	Proton nuclear Magnetic Resonance
χ	Magnetic susceptibility
$\hbar$	Reduced Planck constant $\hbar = \frac{h}{2\pi} = 1.0547 \times 10^{-34} J \cdot s$
m_p	Proton mass, 1.6726×10^{-27} kg
E	Elementary charge = $1.602\ 176\ 487 \times 10^{-19}$ coulombs
I	Spin quantum number
μ	Magnetic permeability of matter
γ	Nuclear gyromagnetic ratio
m_I	Spin state
B_0	External magnetic field in NMR
ΔE	The energy difference between the two states of nucle $\Delta E = \gamma \hbar B_0$
ω_0	The resonance frequency, or Larmor frequency in radians per second
k_B	Boltzmann constant
T	Tesla
$°C$	Temperature in Celsius
RF	Radio frequency
M_0	Equilibrium magnetization
$\vec{B}$	A longitudinal field of amplitude B_0
$\overrightarrow{M}$	Nuclear magnetization
T_1	Spin lattice relaxation time constant
TI	The inversion time in the inversion recovery pulse sequence for measuring T_1
TR	The waiting time after the 90° pulse in the inversion recovery pulse sequence for measuring T_1
T_2	Spin-spin relaxation time constant
τ_c	Correlation Time
$M_{x,y}$	Magnetization component in x-y plane

B'	The additional magnetic field induced by the magnetic field B_0 and the electric current in the electron cloud surrounding the nucleus
σ	Shielding constant (dimensionless number)
δ	NMR chemical shift
ρ (t)	Density operator
ρ_0	Equilibrium spin state
ρ_D	Desired Target Spin State
TSP	3-(trimethylsilyl)-propionic acid-d4 sodium salt
TMS	Tetramethylsilane
D_2O	Deuterium oxide (heavy water)
D	Diameter
ID	Inner diameter
OD	Outer diameter
^{31}P	Isotope of Phosphorus
^{15}N	Isotope of Nitrogen
^{13}C	Isotope of Carbon
BBO	Room temperature broad band frequency NMR probe head (Bruker)
HRMAS	High Resolution Magic Angle Spinning
1D NMR	One dimensional Nuclear Magnetic Resonance
2D NMR	Two-dimensional Nuclear Magnetic Resonance
TOCSY	Total Correlation Spectroscopy
DOSY	Diffusion Ordered Spectroscopy
COSY	Coherence Correlation Spectroscopy
Zgpr	Pre-saturation pulse sequence of 1D ^1H to suppress water signal
Ppm	Parts Per Million
Rpm	Revolutions per minute
SNR	Signal-To-Noise Ratio
Lw	Linewidth
BA	Benzoic acid
Ala	Alanine
Phe	phenylalanine
Tau	Taurine
Cyc	Cyclopentenone
LF	Low Field
OCP	Optimal Control Pulses

GRAPE	Gradient Ascent Pulse Engineering
HP	Hard Pulse
Λ	penalty factor
$\emptyset$	final cost
H(t)	Hamiltonian
SFI	Static field inhomogeneity
RFI	Radio Frequency field inhomogeneity
r_{ij}	The internuclear distance
$\Omega_{ij}^{PL,dip}$	The set of Euler angles
DPFGSE	Double Pulsed Field Gradient Spin Echo
PURGE	Pre-saturation Utilizing Relaxation Gradients and Echoes
SAR	Saturation Attenuation Recovery
CSA	chemical-shift anisotropy
MLHM	Multilayer Halbach Magnet
I	Electrical Current
R	Ohmic resistance
O_1	Central Resonance Frequency
EF	Excitation Factors
SF	Suppression Factors
GP	Gaussian pulses

Abstract

This study introduces a low-field NMR spectrometer (LF-NMR) featuring a multilayer Halbach magnet supported by a combined mechanical and electrical shimming system. This setup offers improved field homogeneity and sensitivity compared to spectrometers relying on typical Halbach and dipole magnets. The multilayer Halbach magnet was designed and assembled using three nested cylindrical magnets, with an additional inner Halbach layer that can be rotated for mechanical shimming. The coils and shim-kernel of the electrical shimming system were constructed and coated with layers of zirconia, thermal epoxy, and silver-paste to facilitate passive heat dissipation and ensure mechanical and thermal stability. Furthermore, the 7-channel shim coils were divided into two parts connected in parallel, resulting in a reduction of joule heating temperatures from 96.2 °C to 32.6 °C. Without the shimming system, the Halbach magnet exhibits a field inhomogeneity of approximately 140 ppm over the sample volume. The probehead was designed to incorporate a solenoidal mini coil, integrated into a single planar board. This design choice aimed to enhance sensitivity, minimize B_1 inhomogeneity, and reduce impedance discrepancies, transmission loss, and signal reflections. Consequently, the resulting linewidth of water within a 3 mm length and 2.4 mm inner diameter sample volume was 4.5 Hz. To demonstrate the effectiveness of spectral editing in LF-NMR applications at 29.93 MHz, we selectively excited hydroxyl and/or methyl protons in neat acetic acid using optimal control pulses calculated through the Krotov algorithm.

Additionally, the use of optimal control pulses is demonstrated to be feasible at a field strength as low as 0.5-0.7 T. The optimal control pulse shapes were calculated using the Krotov algorithm. Downsizing the complexity of the algorithm from exponential to polynomial is shown to be possible in a mixture of non-coupled spin systems by using a system approach with each system corresponding to a (small) molecule. In this way compound selective excitation pulses can be calculated. The signals of substructures of the cyclopentenone molecule were excited using optimal control pulses calculated by the Krotov algorithm demonstrating the feasibility of subspectral editing. Likewise, for a mixture of benzoic acid and alanine, editing of the signals of either benzoic acid or alanine employing optimal control pulses was shown to be possible. The results are very promising and can be extended to the targeted analysis of complex mixtures such as biofluids or metabolic samples at low field strengths opening access for benchtop NMR to point of care settings.

Spectral dispersion in low-field NMR is limited and that can severely affect the analysis of mixtures. Therefore, spectral editing employing optimal control pulses is a suitable approach to cope with the signal superposition in complex mixture spectra. In this work, implementation of optimal control pulses at a field strength as low as 0.5-0.7 T is proven to be feasible and the compound selective excitation pulses shapes were calculated using the Krotov algorithm. The excitement and elimination of phenylalanine (Phe) and Taurine (Tau) spectra as individual or both were shown to be possible using the Krotov algorithm. The multiple-pulse WAHUHA sequence was implemented at high and low field NMR to eliminate the dipolar terms in the average spin Hamiltonian up to the first order. Customizing the multiple-pulse WAHUHA sequence in low- and high-field NMR and applying to Phe-Tau with agarose (1.5%) led to a reduction of homonuclear dipolar coupling to 85% (or by 15%). Accordingly, the linewidth was reduced from 20 Hz to 15 Hz in the overlapped NMR signal at low field NMR and was reduced from 15 Hz to 9 Hz in the high-resolution signal. The implementation of WAHUHA sequence corresponds to magic angle spinning NMR at speed of 2000-3000 rpm. Water suppression through optimal control pulses was implemented by inclusion of the water molecule in the Hamiltonians of a multicomponent mixture. The obtained results can be extended to the targeted analysis of complex mixtures such as biofluids or metabolic samples at low field strengths.

Zusammenfassung

Diese Studie stellt ein Niedrigfeld-NMR-Spektrometer (LF-NMR) vor, welcher über einen mehrschichtigen Halbach-Magneten verfügt, der von einem kombinierten mechanischen und elektrischen Shim-System unterstützt wird. Diese Einrichtung bietet eine verbesserte Feldhomogenität und Empfindlichkeit im Vergleich zu Spektrometern, die auf Halbach- und Dipolmagneten basieren. Der mehrschichtige Halbach-Magnet enthält drei ineinander verschachtelte zylindrische Magnete, wobei eine zusätzliche innere Halbach-Schicht für mechanisches Shimmen gedreht werden kann. Die Spulen und Shim-Kerne des elektrischen-Systems sind mit Zirkoniumoxid, thermischem Epoxid und Silberpaste beschichtet, um passive Wärmeableitung zu ermöglichen und mechanische sowie thermische Stabilität zu gewährleisten. Darüber hinaus sind die 7-Kanal-Shim-Spulen in zwei Teile aufgeteilt, die parallel verbunden sind, was zu einer Reduzierung der Jouleschen Erwärmung von 96,2 °C auf 32,6 °C führte. Ohne das Shim-System zeigt der Halbach-Magnet eine Feldinhomogenität von etwa 140 ppm über dem Probenvolumen. Der Probenkopf ist so konzipiert, dass er eine solenoidale Minispule enthält, die in eine einzelne planare Platine integriert ist. Diese Designwahl zielt darauf ab, die Empfindlichkeit zu verbessern, B_1-Inhomogenität zu minimieren sowie Impedanzunterschiede, Übertragungsverluste und Signalreflexionen zu reduzieren. Infolgedessen beträgt die resultierende Linienbreite von Wasser 4,5 Hz, bei einem Probenvolumen von 3 mm Länge und 2,4 mm innerem Durchmesser. Um die Wirksamkeit der spektralen Bearbeitung in LF-NMR-Anwendungen bei 29,934 MHz zu demonstrieren, wurden hydroxylierte und/oder methylhaltige Protonen in reiner Essigsäure selektiv angeregt, wobei die optimalen Steuerimpulse durch den Krotov-Algorithmus berechnet wurden.

Zusätzlich wurde gezeigt, dass die Verwendung von optimalen Steuerimpulsen bei einer Feldstärke von nur 0,5-0,7 T machbar ist. Die Formen der optimalen Steuerimpulse wurden mit dem Krotov-Algorithmus berechnet. In einer Mischung von nicht gekoppelten Spinsystemen war eine Vereinfachung der Komplexität des Algorithmus von exponentiell auf polynomial möglich. Hierbei wurde ein systemischer Ansatz verwendet, wobei jedes System einem (kleinen) Molekül entspricht. Auf diese Weise können verbindungsspezifische Anregungsimpulse berechnet werden. Die Signale von Substrukturen des cyclopentenone Moleküls wurden unter Verwendung von optimalen Steuerimpulsen angeregt, was die Machbarkeit der Subspektralbearbeitung zeigt. Ebenso wurde für eine Mischung von Benzoesäure und Alanin nachgewiesen, dass durch Verwendung optimaler Steuerimpulse die Signale von entweder Benzoesäure oder Alanin

bearbeitet werden können. Die erhaltenen Ergebnisse sind sehr vielversprechend und können auf die gezielte Analyse komplexer Gemische wie Bioflüssigkeiten oder Stoffwechselproben bei niedrigen Feldstärken ausgedehnt werden, was den Zugang zu Benchtop-NMR in Point-of-Care-Umgebungen ermöglicht. Die spektrale Auflösung in der Niedrigfeld-NMR ist begrenzt, welches die Analyse von Mischungen erheblich beeinträchtigen kann. Daher ist die spektrale Bearbeitung unter Verwendung optimaler Steuerimpulse ein geeigneter Ansatz, um mit der Überlagerung von Signalen in komplexen Mischspektren umzugehen. In dieser Arbeit wurde nachgewiesen, dass die Implementierung von optimalen Steuerimpulsen bei einer Feldstärke von nur 0,7 T machbar ist und die Formen der verbindungsspezifischen Anregungsimpulse mithilfe des Krotov-Algorithmus berechnet werden können. Unter Verwendung dieses Algorithmus konnte gezeigt werden, dass die Spektren von Phenylalanin (Phe) und Taurin (Tau) jeweils einzeln oder beide gemeinsam angeregt oder eliminiert werden. Die Multipuls-WAHUHA-Sequenz wurde in der Hoch- und Niedrigfeld-NMR implementiert, um die dipolaren Terme im durchschnittlichen Spin-Hamiltonian bis zur ersten Ordnung zu eliminieren. Die Anpassung der Multipuls-WAHUHA-Sequenz in der Niedrig- und Hochfeld-NMR und die Anwendung auf Phe-Tau mit Agarose (1,5%), führten zu einer Reduzierung der homonuklearen dipolaren Kopplung auf 85% (oder um 15%). Entsprechend wurde die Linienbreite bei der Niedrigfeld-NMR von 20 Hz auf 15 Hz im überlappten NMR-Signal reduziert und die Linienbreite bei der Hochfeld-NMR von 15 Hz auf 9 Hz verringert. Die Implementierung der WAHUHA-Sequenz entspricht der Magic-Angle-Spinning NMR (MAS-NMR) bei einer Geschwindigkeit von 2000-3000 U/min. Die Unterdrückung von Wasser durch optimale Steuerimpulse wurde durch Einbeziehung des Wassermoleküls in die Hamiltonians einer Mehrkomponenten-Mischung erreicht. Die erhaltenen Ergebnisse können auf die gezielte Analyse komplexer Gemische wie Bioflüssigkeiten oder Stoffwechselproben bei niedrigen Feldstärken ausgedehnt werden.

1 Introduction and literature review

Nuclear magnetic resonance (NMR) spectroscopy is a quantitative, highly reproducible, and non-destructive method used for diagnostics, monitoring disease progression, therapeutic interventions, and various other applications [1]. However, high-field NMR spectrometers are extremely heavy and very costly. Low-field NMR spectroscopy has garnered significant interest for analyzing the physical, chemical, and structural properties of substances, including small molecules, lipids, and rigid solids [2-18]. These spectrometers offer advantages such as affordability, ease of maintenance, and portability [6, 19], along with lower operational costs compared to high-field NMR spectrometers [15]. This technique is commonly employed for identifying and quantifying small molecules [7, 9, 11, 20-23], larger molecules like lipids [13, 24], polymers [25], and rigid solids [2, 14, 16]. Furthermore, it holds promise for predicting, diagnosing, monitoring, and prognosticating diseases, as well as optimizing medication dosages. Metabolite concentrations obtained through LF-NMR enable predictions of a patient's health status and potential health risks [17, 18, 26]. LF-NMR can simultaneously determine many metabolites in body fluids such as saliva, urine, and cerebrospinal fluid [27].

Despite its advantages, LF-NMR faces challenges, particularly in sensitivity and signal overlap due to reduced frequency dispersion. This overlap leads to significant signal superposition in NMR spectra of complex mixtures, complicating identification and quantification. Low spectral dispersion further hinders molecular assignment and quantification in complex biological mixtures, such as biofluids and soft tissue samples [28]. Various techniques, including pure shift NMR and diffusion-ordered spectroscopy, have been developed to address signal superposition in NMR studies [29, 30]. The long-lived-coherence correlation spectroscopy (LLC-COSY) method also addresses challenges related to inhomogeneities in local static fields and homogeneous broadening caused by dipole-dipole interactions [31]. However, these methods may suffer from drawbacks like reduced signal-to-noise ratio (SNR) or the need for specialized equipment, limiting their efficacy in low-field NMR experiments.

Several strategies have been explored to tackle the challenges of poor magnetic field homogeneity and limited spectral dispersion in NMR spectroscopy [32, 33].

Pure-shift NMR enhances spectral resolution by suppressing multiplet structures in ^{1}H-NMR spectra, effectively converting all signals into singlets [34, 35]. While predominantly utilized in high-field NMR, recent advancements have extended pure-shift methodologies to

benchtop NMR spectrometers, addressing the inherent challenge of peak overlap. At 43 MHz, techniques such as PSYCHE and Zangger-Sterk (ZS) have been implemented, with PSYCHE demonstrating superior sensitivity and ZS offering greater robustness against strong couplings and broad signals [29]. Despite its advantages, the inherent sensitivity loss, resulting from signal averaging and decoupling strategies, poses challenges for detecting dilute samples. Additionally, extended acquisition times and the complexity of pulse sequence optimization limit its practicality for routine analysis. While effective in resolving peak overlap, pure-shift methods may not fully disentangle highly congested spectra, particularly in complex mixtures or macromolecules. Furthermore, their susceptibility to pulse imperfections, hardware constraints, and relaxation effects can compromise spectral quality, especially at low field strengths [36].

Another technique, Diffusion-Ordered Spectroscopy (DOSY), has been employed to address issues of spectral overlap, though it has shown limited effectiveness in improving resolution [8, 30]. To further enhance magnetic field homogeneity and spectral quality, novel advancements are needed. In this context, the development of Halbach arrays presents a promising solution. Halbach arrays, a specialized arrangement of permanent magnets that enhance the magnetic flux on one side while reducing or eliminating it on the opposite side, have significantly advanced low-field NMR technology [37, 38]. Originally proposed by Mallinson in 1971 [39], these arrays can generate strong and homogeneous magnetic fields in various geometries, including linear, circular, and spherical [40]. Their application has led to the development of portable NMR spectrometers capable of achieving magnetic field strengths greater than 3T with field inhomogeneity below 100 ppm [40-44]. However, despite these advancements, the typical field homogeneity of Halbach magnets which is defined as the ratio of magnetic field variation to the mean field strength at the magnet's "sweet spot" ranges from 20 to 2000 ppm [45, 46]. This level of homogeneity is insufficient for high-resolution NMR spectroscopy, which requires even greater field uniformity.

To address the challenges of low-field NMR, this thesis presents the design and construction of a multilayer Halbach magnet. This magnet is a key component aimed at enhancing the feasibility of high-resolution NMR at low field strengths. The design incorporates a concentric, rotatable Halbach array, which functions as an integrated mechanical shim system. This system allows for variable magnetic field amplitudes in the z-y plane (B_0 in the z-direction), significantly improving the homogeneity of the NMR magnetic field (B_{z_0}) [47]. In addition to the mechanical shim system, passive shimming was achieved by introducing a ferromagnetic cylinder into the magnet bore. This modification reduces the

primary NMR magnetic field (B_0) and facilitates adjustments for lower frequencies. The overall design is further enhanced with a layer of quadrupole ferromagnetic cubic elements that create a closed-loop magnetic field configuration, thereby stabilizing the field. Quadrupole triangular focusers are also included to concentrate the magnetic field at the sweet spot, which greatly improves field homogeneity [48].

Optimal control theory was employed to design pulses for various tasks in NMR spectroscopy, including selective excitation, inversion, decoupling, coherence transfer, and Hadamard encoding [49, 50]. In this context, optimizing pulse sequences is crucial for enhancing NMR experiments, particularly in multidimensional NMR, where the aim is to improve coherence transfer while minimizing relaxation effects and signal losses [49].

Additionally, optimal control theory addresses the challenge of low spectral dispersion, enabling effective NMR spectroscopy at low magnetic fields [51]. This method also facilitates subspectral editing experiments, allowing for component-selective excitation [52-56].

The Krotov algorithm was employed to generate pulse sequences that guide spins to a desired final state while accounting for chemical shifts, RF inhomogeneities, and couplings. In the LF-NMR spectrometer developed for this work, optimal control pulses (OCPs) can be customized for specific applications, such as real-time monitoring of target molecules and suppression of interfering species. This technique enables contactless identification and quantification of chemical compounds in complex mixtures using pre-calculated OCP sequences. While traditional methods such as DANTE sequences [57], and shaped pulses [58] can stimulate only a single frequency band, they lack the component selectivity needed for metabolite signals spanning multiple frequency windows.

The Krotov algorithm, tailored for large spin systems, reduces the computational complexity of pulse design from exponential to polynomial [59, 60]. making it particularly effective in low-field NMR. This approach allows for selective excitation of metabolites from mixtures, resolving signals in overlapped spectra. Figure 1.1 demonstrates how the Krotov algorithm enables optimal control pulses to selectively target specific metabolites while excluding others.

Robust pulse designs framed as optimal control problems have demonstrated significant sensitivity improvements at the spectrum's edge compared to conventional pulses in both 1D and 2D NMR experiments [61]. Furthermore, the introduction of the Krotov Python package by M. Goerz et al. [62] facilitates the determination of time-dependent external fields for

various quantum control problems, including state-to-state transfer and quantum gate implementation.

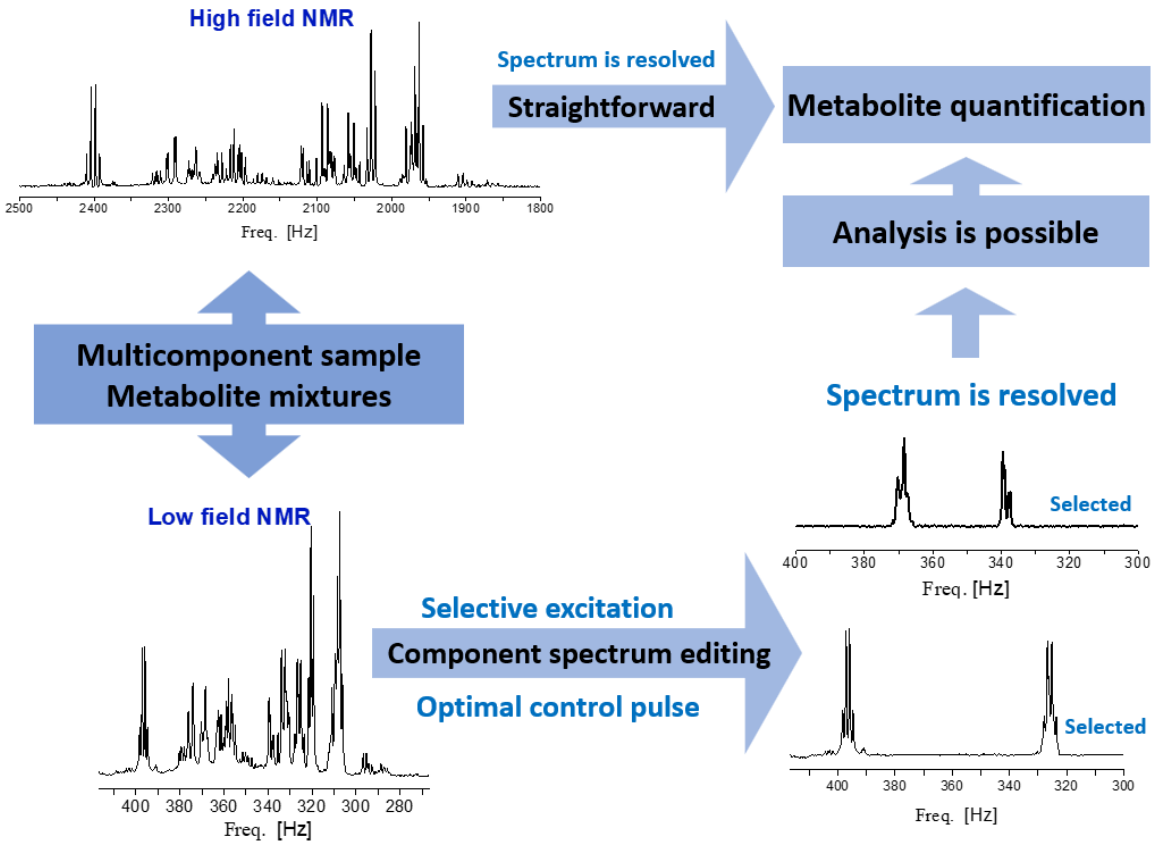

Figure 1.1: Schematic illustration customized from [63] of metabolite-specific spectral editing using optimal control pulses in low-field NMR.

High-Resolution Magic Angle Spinning (MAS) is commonly used to analyze tissue samples in high-field NMR [64, 65]. In MAS, the sample is rotated at a magic angle (54.7 degrees) relative to the external magnetic field to diminish line-broadening effects of the anisotropy of chemical shift and dipolar coupling. Various methods have been employed to decrease the linewidths of NMR peaks resulting from dipolar couplings, including HRMAS, homonuclear dipolar decoupling, and broadband heteronuclear decoupling [66-69]. While the HRMAS technique is effective for mitigating variations in macroscopic magnetic susceptibility in biological samples, it requires specialized hardware such as zirconia rotors and Teflon disposable samples, and rapid spinning can compromise sample integrity. There is a growing demand for high-resolution methods applicable to intact biological samples and adaptable to standard NMR spectrometer hardware. This work re-implements the multiple-pulse WAHUHA sequence with modifications that improve the elimination of dipolar terms

in the average spin Hamiltonian up to the first order, enabling more efficient decoupling of homonuclear dipolar couplings in both high- and low-field NMR spectroscopies [59, 60]. Unlike other techniques, the WAHUHA approach for dipolar decoupling does not require spinning or specialized hardware. Remarkably, the WAHUHA pulse sequence can reduce broadening by 15-20%, making it suitable for viscous samples and biological tissues, especially when combined with optimal control selective excitations [70, 71].

Water NMR signals in biological samples must be suppressed, even when using D_2O (99.98% ^2H), due to residual water signals that can mask solute signals and hinder quantitative analysis. To address this, we implemented a robust water suppression technique using optimal control pulses [72]. This method enables the acquisition of high-quality ^1H-NMR spectra in both high- and low-field NMR spectroscopy settings without requiring specialized pulse sequences or additional equipment.

Although post-processing techniques such as line broadening and zero-filling can enhance the signal-to-noise ratio and spectral resolution, they may introduce artifacts. Optimal control pulses, however, offer a straightforward solution by precisely targeting and suppressing the water signal. This approach enhances spectral quality, ensuring a flat baseline around the suppressed resonances and adjustable phase corrections for improved quantitative accuracy. Additionally, excitation sculpting using arbitrary waveforms and pulsed-field gradients provides highly effective water suppression but requires specialized pulse sequences and equipment [53-56, 73]. The combined use of these techniques contributes significantly to the advancement of low-field NMR capabilities, making it a valuable tool for applications such as point-of-care diagnostics and metabolic analysis of intact soft tissue biopsies or viscous synovial fluid. Our implementation of optimal control pulses enhances the reliability and accuracy of water suppression, demonstrating the promise of optimal control theory in spectral editing and signal processing for low-field NMR spectroscopy [53, 54].

2 Theoretical backgrounds

2.1 Nuclear magnetic resonance (NMR) spectroscopy

The Zeeman effect, discovered by Pieter Zeeman, refers to the splitting of optical spectral lines in the presence of magnetic field. This phenomenon, observed in the late 19th century, led to the identification of magnetic resonances associated with energy level splitting proportional to an external magnetic field. Jevgeni Konstantinovitch Savoiski first observed electron paramagnetic resonance, followed closely by the nearly simultaneous demonstration of nuclear magnetic resonance (NMR) by Edward Mills Purcell in Boston and Felix Bloch in Stanford [74].

Nuclear Magnetic Resonance (NMR) has since become a cornerstone technique in various fields of basic and applied sciences, facilitating the analysis of molecular and supramolecular structures in both organic and inorganic substances. NMR spectroscopy is particularly effective for nuclei with odd mass number (A) or odd atomic number (Z), such as hydrogen (^{1}H), boron (^{11}B), carbon (^{13}C), fluorine (^{19}F), and phosphorus (^{31}P) [75]. Various types of NMR spectroscopy exist, including solid-state, liquid-state, gel phase, comprehensive multiphase (CMP), low-field, and portable NMR spectroscopy. Solid-state and liquid-state NMR spectroscopy are widely employed for molecular structure determination across diverse fields, including materials chemistry, protein structure elucidation, food science, and medicinal and biochemistry [76].

2.1.1 The nuclear resonance effect

The spin of atomic nuclei is characterized by the nuclear spin quantum number I. The spin angular momentum L is expressed as:

$$|L| = \hbar\sqrt{I(I+1)}. \tag{2.1}$$

The component aligned with an applied magnetic field (typically defined along the z-axis) is determined by the equation.

$$L_z = I_z\hbar = m\hbar, \tag{2.2}$$

where the magnetic quantum number, denoted by I_z or m, can have $2I + 1$ values.

$$I_z \equiv m = -I, -I+1, \ldots, I-1, I. \tag{2.3}$$

The values of I are half-integer for odd mass numbers, integer for even mass numbers. Atomic nuclei with spin generate a magnetic moment μ due to their electric charge and rotation, acting as a circular current.

The magnetic induction B_0, expressed in Tesla (T = Vs.m^{-2}), will be utilized to quantify the magnetic fields rather than the magnetic field strength H in units of A.m^{-1}. The magnetization M corresponds to the aggregate of magnetic dipole moments μ per unit volume.

The gyromagnetic ratio (γ) is defined by ($\mu = \gamma L$) [rad s^{-1}T^{-1}] [77, 78] and the z-component of the nuclear magnetic moment can be expressed by ($\mu_z = \gamma L_z$) which is equivalent to $\mu_z = \gamma I_z \hbar \equiv \gamma m \hbar$.

The energy levels of a nucleus with a nuclear spin I are split when subjected to an external magnetic field (B_0) in the z-direction, resulting in $2I + 1$ Zeeman levels. These energy differences are observable and can be expressed in the equation:

$$E_m = \mu_z B_0 = -\gamma m \hbar \, L \, B_0. \tag{2.4}$$

The macroscopic magnetization, which aligns itself in the same direction solely under the influence of an external field, is represented by.

$$M_0 = \chi_0 H_0 = \chi_0 B_0 / \mu_0, \tag{2.5}$$

where χ_0 is the magnetic susceptibility.

When $I =$ ½, m = ± ½, two levels are obtained with an energy difference of

$$\Delta E_{(-\frac{1}{2}, \frac{1}{2})} = \gamma \hbar B_0 = \hbar \omega_L = h \nu_L. \tag{2.6}$$

In Equation (2.6), the energy difference is replaced by the resonant frequency, denoted as the Larmor frequency (ν_L) or Larmor angular frequency (ω_L), named after Joseph Larmor. The Larmor frequency represents the precession of the magnetic moment around an external magnetic field and is proportional to the magnetic field strength [78]. If the rotation is defined by a vector pointing in the same direction as the rotation axis, the relationship can be expressed as:

$$\omega_0 = -\gamma B_0, \tag{2.7}$$

where ω_0 is Larmor precession (Figure 2.1). The frequency (Hz) can be expressed as:

$$\nu_0 = -\frac{1}{2\pi} \gamma B_0, \tag{2.8}$$

where ν_0 is the Larmor frequency [77].

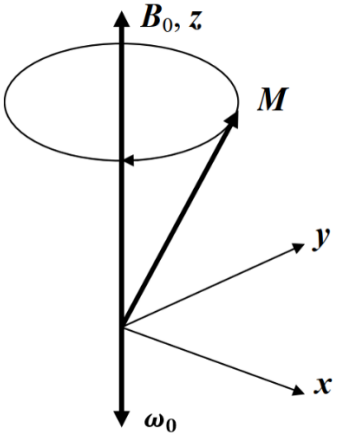

Figure 2.1: Larmor precession in the presence of an external magnetic field [79].

Nuclear with spin quantum number characterized by $I = -1/2$ exhibit magnetic quantum numbers $m_I = +1/2$ (spin up) and $m_I = -1/2$ (spin down) [77, 80]. Figure 2.2 shows the splitting associated with the magnetic field (B_0) according to Zeeman effect [80].

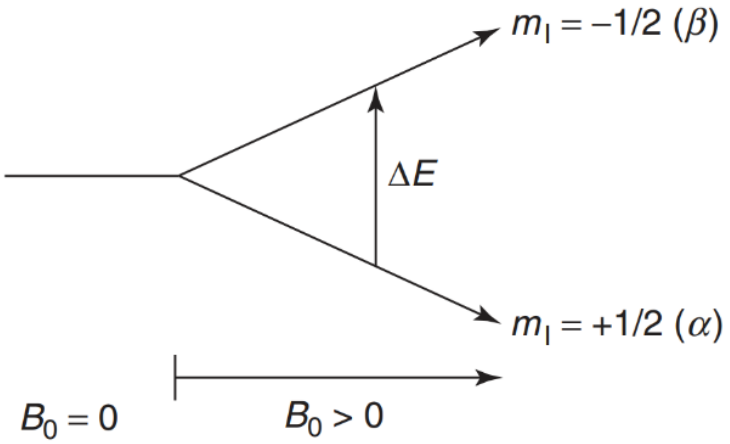

Figure 2.2: Separation of the energy between nuclear spin states in the absence of a magnetic field $\boldsymbol{B_0}$ and in the presence of an increasing magnetic field $\boldsymbol{B_0}$ [81].

The energy difference between the states can be expressed as:

$$\Delta E = \gamma \hbar B_0. \tag{2.9}$$

Other local field differences can be introduced by changing the electron spatial densities in a molecule through chemical bonding. The increased electron density results in an increased shielding. Typically, shielding protects the nucleus from external influence. NMR experiments are performed by placing the sample into the magnet's center and positioned in the NMR probe, ensuring that the sample is located in the magnet's strongest field and most homogeneous region [80, 82].

2.1.2 NMR relaxations

Relaxation in NMR refers to the process by which nuclear spins return to their equilibrium states after being disturbed by an external magnetic field [83]. This process involves both longitudinal relaxation (T_1) and transverse relaxation (T_2).

The torque (T) acting on a magnetic dipole is defined as the time derivative of the angular momentum (L). Given that ($\mu = \gamma L$), we can express this as:

$$T = \frac{dL}{dt} = \frac{1}{\gamma}\frac{d\mu}{dt}. \tag{2.10}$$

By equating this to ($T = \mu \times B$), where B is the external magnetic field, we obtain:

$$\frac{d\mu}{dt} = \gamma\, \mu \times B. \tag{2.11}$$

The magnetization M, representing the sum of nuclear dipoles within a unit volume, follows the equation of motion:

$$\frac{dM}{dt} = \gamma\, M \times B. \tag{2.12}$$

In a static magnetic field $B = (0, 0, B_0)$ with initial magnetization $M(t = 0) = |M|\,(sin(\alpha), 0, cos(\alpha))$ the precession of magnetization components M_x, M_y, and M_z is described by [84]:

$$\frac{dM_x}{dt} = \gamma\left(M_y B_0 - \frac{M_x}{T_2}\right) \tag{2.13}$$

$$\frac{dM_y}{dt} = \gamma\left(M_x B_0 - \frac{M_y}{T_2}\right) \tag{2.14}$$

$$\frac{dM_z}{dt} = \frac{M_0 - M_z}{T_1}. \tag{2.15}$$

Here, T_1 denotes the longitudinal relaxation time, and T_2 is the transverse relaxation time. These equations incorporate both precession and relaxation processes, providing a comprehensive description of the dynamics:

- Transverse Relaxation (T_2): The decay of transverse magnetization is exponential:

$$M_x(t) = e^{-t/T_2}\left(M_x(0)\cos(\omega_0 t) + M_y(0)\sin(\omega_0 t)\right) \tag{2.16}$$

$$M_y(t) = e^{-t/T_2}\left(M_y(0)\cos(\omega_0 t) - M_x(0)\sin(\omega_0 t)\right). \tag{2.17}$$

- Longitudinal Relaxation (T_1): The recovery of longitudinal magnetization is also exponential:

$$M_z(t) = M_z(0)e^{-t/T_1} + M_0\left(1 - e^{-t/T_1}\right). \quad (2.18)$$

There are two primary relaxation processes in NMR:

- Longitudinal Relaxation (T_1): This process involves the return of nuclear spins to thermal equilibrium with the magnetic field. It is characterized by the recovery of the longitudinal magnetization, M_z, towards its equilibrium value M_0 [85].
- Transverse Relaxation (T_2): This process involves the decay of transverse magnetization M_x and M_y, which diminishes due to interactions among spins, leading to dephasing [86, 87].

In solid and semi-solid materials, T_2 values are typically shorter than T_1 values because transverse magnetization decays more rapidly than longitudinal magnetization (Figure 2.3). The correlation time (τ_c) characterizes the time scale over which fluctuations in the local magnetic environment of a nucleus occur. It is not directly related to the Larmor frequency (ω_0). Instead, τ_c reflects the dynamics of molecular motion, particularly the frequency of molecular tumbling or rotation. τ_c plays a crucial role in determining the nuclear spin relaxation rates (T_1 and T_2) in NMR, where relaxation is influenced by the interaction between the nuclear spins and the fluctuating local magnetic fields [88, 89].

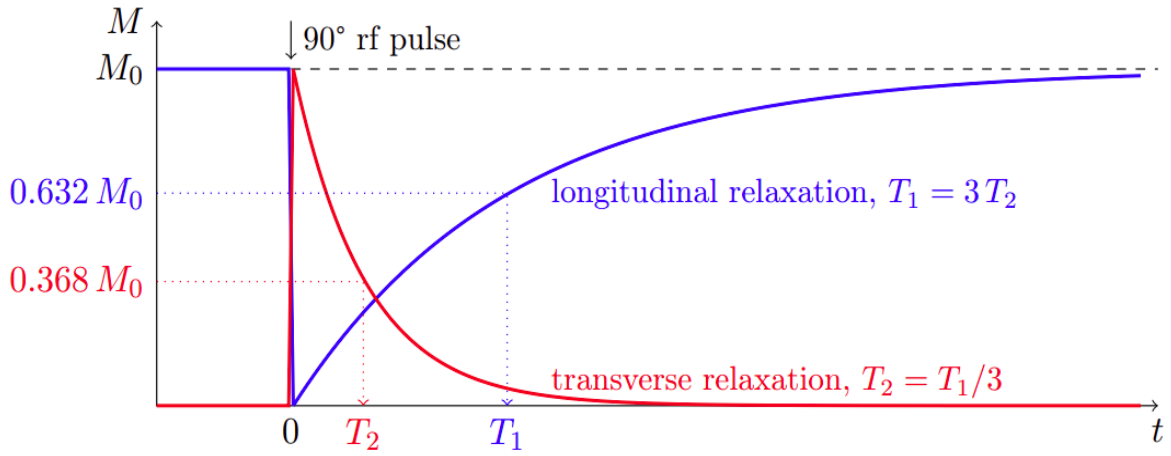

Figure 2.3: Comparison of spin-lattice (T_1) and spin-spin (T_2) relaxation times. In solid and semi-solid materials, T_2 is typically shorter than T_1 due to faster decay of transverse magnetization. Adapted from reference [90].

As τ_c increases, the longitudinal relaxation rate (T_1) typically increases to a maximum value. This is because longer correlation times imply slower fluctuations in the local magnetic field, which can more effectively drive the longitudinal magnetization back to its equilibrium state.

In contrast, the transverse relaxation time (T_2) reflects the decay of transverse magnetization. T_2 is influenced not only by spin-spin interactions but also by dephasing due to fluctuations in the local magnetic field, molecular motions, and other interactions. These factors generally lead to a faster decay of transverse magnetization compared to longitudinal relaxation (T_1) [83].

2.1.3 Free induction decay (FID) and NMR signal

The Free Induction Decay (FID) is the oscillating electric current produced by the precession of transverse nuclear magnetization (Figure 2.4a) [91, 92]. After a π/2 pulse is applied, nuclear moments can be inverted, aligning the magnetization perpendicular to the static magnetic field B_0. The FID decays as the magnetization returns to equilibrium, reflecting relaxation processes.

The NMR spectrum is obtained by Fourier transforming the FID and can be displayed on a chemical shift scale ($\delta = (\nu_{ref} - \nu)/\nu_L$) rather than frequency (ν). The FID signals also decay over time due to relaxation processes such as spin-spin relaxation (T_2 relaxation). Each component's rate of decay in the FID is inversely proportional to the T_2 relaxation time, and this decay rate is reflected in the linewidth of the corresponding NMR signal in the spectrum, as shown in Figure 2.4a.

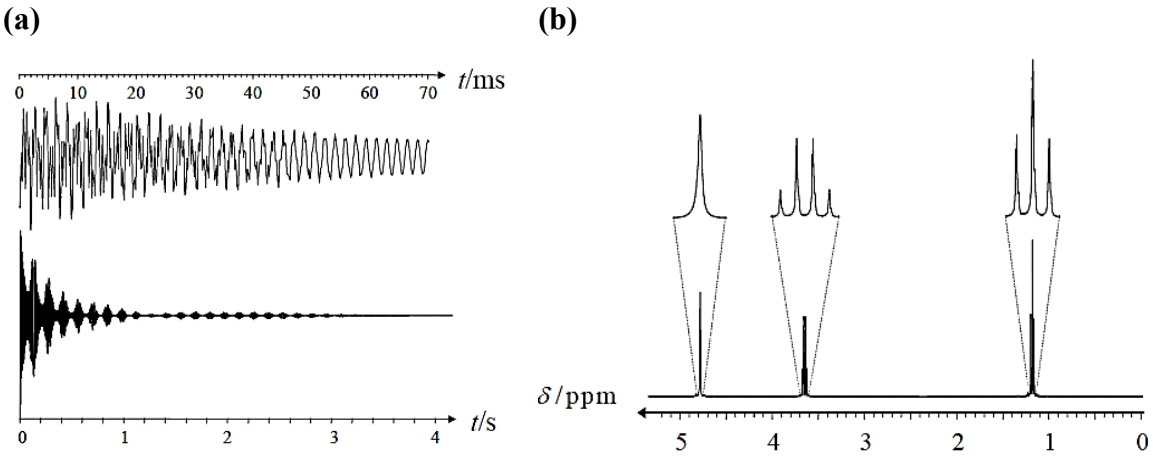

Figure 2.4: **(a)** Free Induction Decay (FID) at a Larmor frequency of 400 MHz and the corresponding Fourier-transformed ^{1}H-NMR spectrum of ethanol (EtOH) in deuterated water. **(b)** The Fourier transformation of the FID to obtain the NMR spectrum. The singlet corresponds to the OH groups, which exchange with solvent hydrogen nuclei and therefore exhibit no splitting. The quartet represents the CH_2 groups, and the triplet corresponds to the CH_3 group of ethanol [93].

The spectrum in Figure 2.4 was acquired at a frequency of $\nu_L = 400$ MHz and displays lines spaced approximately 8 Hz apart, which is about 2×10^{-8} times the Larmor frequency. Such high resolution requires sample homogeneity and a stable magnetic field over time [94]. Enhancing the homogeneity of the static magnetic field can be achieved by adjusting currents in several shim coils surrounding the sample.

2.1.4 The chemical shift (δ)

NMR spectroscopy is used to discern the characteristics of specific nuclei within their molecular environments. The resonance frequency of a nucleus shifts due to electron distribution in chemical bonds, which depends on the molecular structure [71]. Different peaks in the spectrum correspond to various chemical shifts experienced by the nucleus, aiding in molecule identification [77, 80].

Chemical shift, the phenomenon of different NMR signals arising from diverse chemical groups, results from the varying chemical environments of protons in a molecule. Under an applied magnetic field B_0 of 2.35 T, proton resonances occur not at the typical ν_0= 100 MHz, but at $\nu_0 \pm \nu$, where ν for protons is generally less than 1 kHz. This effect is observed in other magnetic nuclei as well and forms the foundation for applied NMR spectroscopy [95].
B_0 induces circulations in the electron cloud around the nucleus, generating a magnetic moment μ that opposes B_0, according to Lenz's law. This results in magnetic shielding, reducing B_0 by a factor σ, the shielding constant [96]:

$$B_{local} = B_0(1 - \sigma). \tag{2.19}$$

Here, σ is proportional to the electron density of the 1s orbital, and σB_0 represents the secondary field induced at the proton. This reduction in the local field causes the resonance condition to occur at a lower frequency. The perturbation of the spherical symmetry of the electron distribution reduces the diamagnetic effect by other nuclei, behaving as a paramagnetic moment that reinforces B_0. Consequently, the σ-value in molecules is the sum of diamagnetic and paramagnetic components of the induced electronic motion [97]:

$$\sigma = \sigma_{dia} + \sigma_{para}. \tag{2.20}$$

Theoretical calculations of chemical shifts typically use advanced quantum chemical methods, often limited to small molecules. NMR chemical shifts are crucial for determining the structures of unknown compounds, such as metabolites.

Figure 2.5 shows the characteristic ranges for signals of key types of protons in organic molecules. The shielding of C– H bonds decreases in the following order: $CH_3 > CH_2 > CH$. The chemical shift of methyl group protons is 0.9 ppm, while the chemical shift of cyclohexane protons is 1.4 ppm. Olefinic protons have shifts in the 4.0–6.5 ppm range. Acrolein ($CH_2 = CHCHO$) protons have shifts larger than 6.5 ppm, and aromatic molecules have shifts in the 7.0–9.0 ppm range.

Electronegative elements like nitrogen, oxygen, and halogens induce high-frequency shifts for neighboring protons, and multiple neighboring bonds have a similar effect. Aldehyde and carboxylic acid protons typically have very high frequency shifts (δ > 8 ppm). The NMR signals of protons in OH, NH, NH_2, and CO_2H groups strongly depend on concentration, temperature, and solvent. For instance, the OH signal is at a chemical shift of 1.4 ppm in purified methanol but shifts to 4.0 ppm in an impure sample.

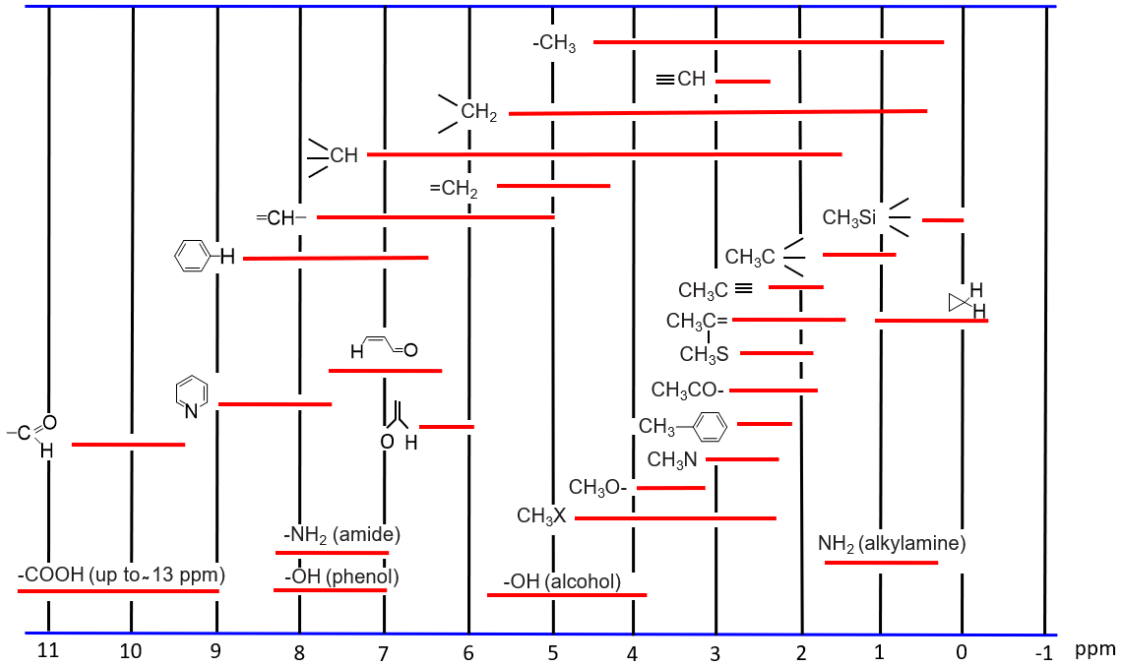

Figure 2.5: The δ-Scale of chemical shifts of proton resonances in organic compounds [98].

2.1.5 Spin–Spin coupling

Spin-spin coupling in NMR spectra, represented by *J* and measured in Hz, arises from the interaction of spins through bonding electrons. This interaction, discovered independently in several laboratories in 1950, results in line splitting of resonances [99]. For various couplings such as $^1H–^1H$, $^1H–X$, and X–X, *J* provides characteristic molecular structure information [100]. When two protons are magnetically inequivalent, each proton's resonance splits into two peaks. Protons with a spin of 1/2 exhibit two energy levels (+1/2, -1/2), resulting in two

split lines, while nuclei with a spin of one ($I = 1$) show three lines due to three energy levels (+1, 0, -1). Strong coupling between two spins leads to a frequency separation comparable to the coupling constant, causing intensity changes in the doublets. This intensity perturbation, where outer peaks become lower and inner peaks become higher, is known as 'roofing' [101].

2.1.6 Linewidth and broadening

The linewidth of an NMR peak, often quantified by the Full Width at Half Maximum (FWHM), reflects various contributing factors [102, 103]. These contributions can be categorized into coherent and incoherent components, along with effects arising from sample inhomogeneity. The coherent contribution primarily stems from the spin-system's Hamiltonian and is predominantly influenced by homonuclear dipolar couplings, isotropic, and anisotropic chemical shifts. Conversely, the incoherent contribution arises from stochastic processes, primarily driven by relaxation and chemical exchange. Additionally, the sample's inhomogeneity, resulting from interactions between the sample and magnetic field heterogeneity, contributes to line broadening.

For solid samples, the linewidth due to both coherent and incoherent factors can be mitigated by Magic Angle Spinning (MAS). Increasing the MAS spinning rate typically reduces these contributions, leading to narrower linewidths categorized as homogeneous. However, addressing the effects of sample inhomogeneity requires interventions such as refined sample preparation techniques, optimized probe designs, or adjustments to shim coil currents.

In liquid-state samples, MAS is not typically employed, as the molecular motion averages out dipolar couplings and chemical shift anisotropies, resulting in naturally narrow linewidths. Instead, linewidth optimization in liquid-state NMR focuses on factors such as solvent purity, temperature control, and proper shimming to correct magnetic field inhomogeneities. For viscous biological samples, which exhibit properties intermediate between liquids and solids, specialized approaches are required. Techniques such as spinning the sample at lower speeds or employing methods like high-resolution magic angle spinning (HR-MAS) can be useful. Additionally, careful temperature regulation and the use of specialized probes designed for viscous samples can help manage linewidth broadening and achieve clearer NMR spectra.

2.2 Low-field NMR spectroscopy

2.2.1 Introduction

NMR experiments typically utilize large magnetic fields to improve chemical shift resolution and signal intensity [104]. Low-field NMR, defined as fields below 2T generated by permanent magnets, presents specific challenges, such as temperature stability due to magnetic field drift, which can vary between 0.03% per 1°C in SmCo and 0.1% per 1°C in NdBFe. Precise temperature control is essential to minimize frequency drift. Additionally, shimming is crucial for enhancing the resolution of NMR spectra and MRI imaging, especially when using spectrometers based on permanent magnets [105]. Despite these challenges, low-field NMR has found applications in rapid quality control methods, focusing mainly on NMR relaxation processes like T_1 and T_2 relaxation times, as well as Magnetic Resonance Imaging (MRI) [2, 9, 106]. However, low-field NMR faces specific challenges, such as broader lines, lower resolution, and reduced sensitivity compared to high-field NMR. The energy separation between nuclear spin states, as described by the Zeeman equation, is directly proportional to the magnetic field strength (B_0), though the total energy separation in NMR spectra also depends on other interactions, such as chemical shifts and spin-spin couplings [107, 108].

However, the limited spectral range in low-field NMR, resulting from the direct proportionality between energy separation of nuclear spin states and magnetic field strength (B_0) as described by the Zeeman equation, leads to significant spectral overlap. This overlap results in a loss of distinct spectral features crucial for chemical analysis, thereby hindering metabolic profiling and the accurate identification of specific metabolites [109].

2.2.2 Optimal design of magnet array (Halbach magnet)

The Halbach array, introduced by John C. Mallinson in 1973 and independently developed by Klaus Halbach in the 1980s for particle accelerator beam focusing, features a distinctive magnet arrangement that enhances the magnetic field on one side while canceling it on the other (Figure 2.6a). This is achieved through a strategic layout of permanent magnets, which concentrates magnetic flux on one side and minimizes it on the other, allowing for stronger and more directed magnetic fields compared to conventional setups. This configuration enables the use of smaller magnets while focusing field strength and reducing stray fields. The Halbach array has since revolutionized magnetic field engineering, finding applications in electric motors, generators, magnetic levitation (Maglev) systems, Magnetic Resonance

Imaging (MRI), Nuclear Magnetic Resonance (NMR), and particle accelerators, thereby increasing efficiency and performance.

In magnetic resonance (MR) technology, Halbach arrays have been crucial in developing advanced benchtop and handheld MR instruments, achieving field strengths exceeding 3T with inhomogeneity levels below 0.01% (100 ppm). Notably, the Halbach cylinder generates a stronger and more homogeneous magnetic field per unit mass than dipolar permanent magnets [3, 110]. Furthermore, the magnetic field of the Halbach cylinder is oriented perpendicular to its axis (Figure 2.6b), which facilitates the integration of solenoidal RF coils and allows for versatile NMR experiments where the magnetic field direction can be adjusted relative to the sample [2, 16].

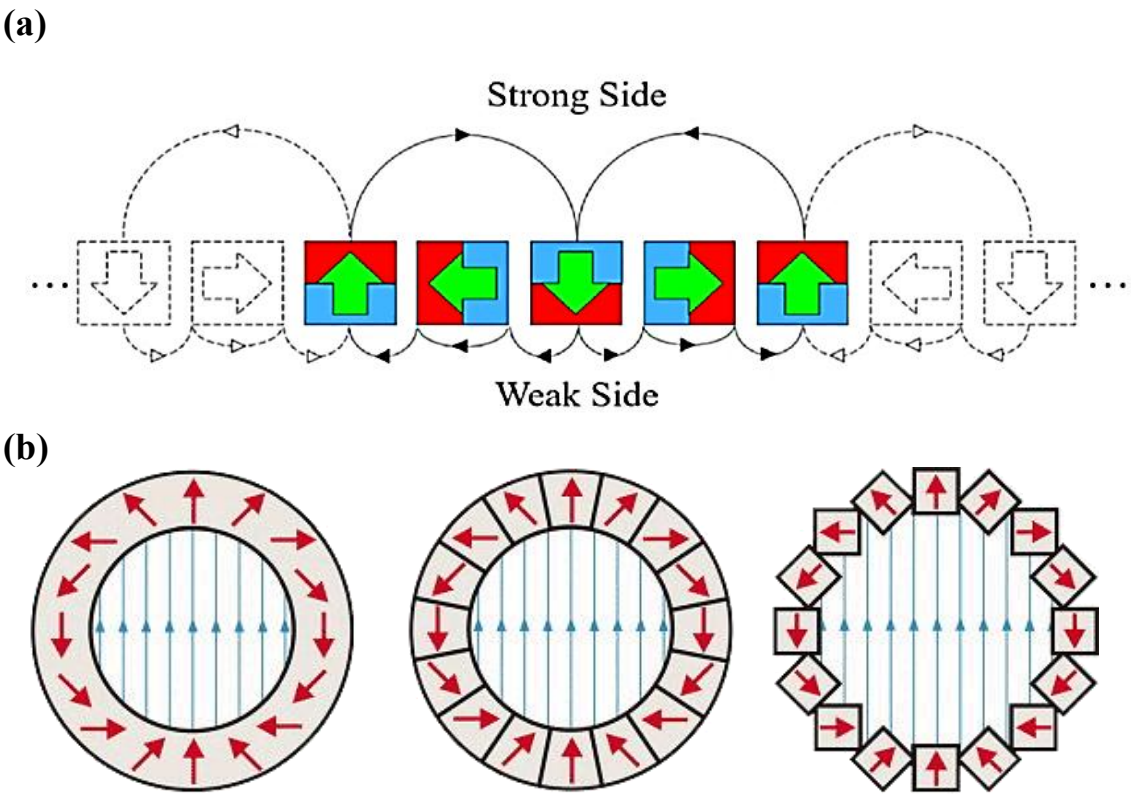

Figure 2.6: (a) Schematics representation of a Halbach array [111]. **(b)** Schematic illustration of how magnets can be arranged to result in circular Halbach array ring [112].

Halbach cylindrical configurations are highly effective for low-field magnetic resonance, particularly in NMR and MRI. These configurations generate a strong, homogeneous, radially oriented magnetic field inside the cylinder, while maintaining zero field outside, assuming an infinitely long cylinder. Typically constructed from several trapezoidal or arc-shaped magnet segments, the magnetic orientation vectors in these segments rotate systematically to focus the field. The uniformity of the magnetic field improves with an increasing number of discrete magnets used in the assembly. A notable construction

technique for Halbach circular dipolar arrays, known as NMR-Mandhalas, was introduced by H. Raich and P. Blümler (2004) using identical magnets [40]. Nested Halbach arrays, arranged concentrically, are frequently employed in NMR to generate different magnetic field strengths and distributions along the cylindrical axis. The advent of advanced 3D printing technology has facilitated the precise fabrication of these structures, ensuring accurate arrangement and orientation of the magnets.

2.2.3 Ideal Halbach dipoles: Single and nested

This section focuses on cylindrical Halbach arrays that produce uniform dipolar magnetic fields, often referred to as Halbach dipoles, as illustrated in Figure 2.7. In the case of an ideal Halbach dipole, which can be visualized as an infinitely long tube with a continuously rotating magnetization within its wall, the resulting magnetic field is uniform within a cross-sectional plane [38, 40, 110, 113]. The strength of this field is given by

$$B_{Outer} = B_{rem}\left(\frac{r_1}{r_2}\right), \tag{2.21}$$

where B_{rem} is the remanence of the permanent magnetic material, and r_1 and r_2 are the outer and inner radii of the tube, respectively [38] as shown in Figure 2.7a which is adapted from the literature [114]. Now consider a configuration where two concentric, nested Halbach dipoles are used, as depicted in Figure 2.7b. In this case, the inner dipole generates a uniform magnetic field with strength given as following formula.

$$B_{outer} = B_{rem}\left(\frac{r_3}{r_4}\right). \tag{2.22}$$

If the inner dipole's radii are set such that $r_3 = r_2$ and $r_3 = \frac{r_2^2}{r_1}$, it follows that $|B_{outer}| = |B_{inner}|$. The total field in the center of the two dipoles is the vector sum of B_{outer} and B_{inner}. resulting in $B_{tot} = B_{outer} + B_{inner}$. For this specific geometric arrangement, if the two nested dipoles rotate in equal and opposite directions, any desired field strength within the range of $\mp|B|_{\text{tot}}^{\max}$ can be achieved.

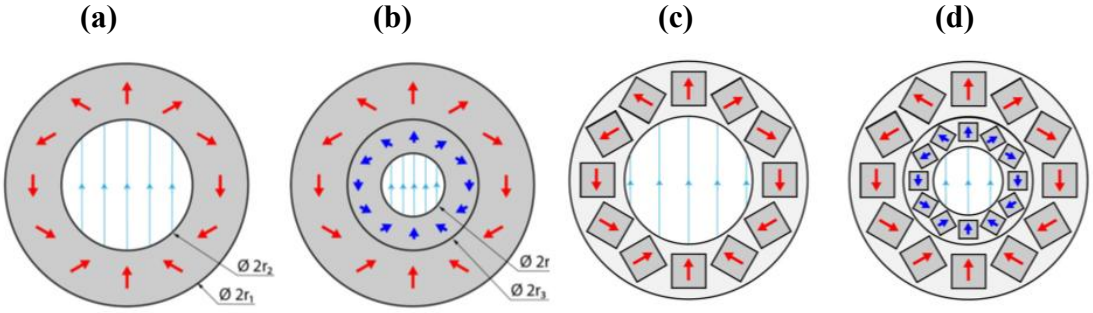

Figure 2.7: Schematic illustration of ideal cylindrical Halbach dipoles: **(a)** single and **(b)** nested. Schematic illustration of discretized cylindrical Halbach dipoles: **(c)** single and (d) nested. The magnetization of each structure is represented by the red and blue arrows. In the discretized case, the arrows denote the magnetization orientation of cuboid magnets.

Continuing from the previous explanation, consider the arrangement of nested Halbach dipoles along a single axis, as illustrated in Figure 2.8 which is adapted from the literature [114]. This configuration offers significant flexibility in selecting the operating alternating frequency and tuning the magnetic field [115, 116] . However, while this design allows for the generation of variable magnetic fields along a single axis, it does not offer the same degree of flexibility for 3D optical and mechanical access. The system is limited to single-axis control, restricting its use in applications where multi-dimensional manipulation is required.

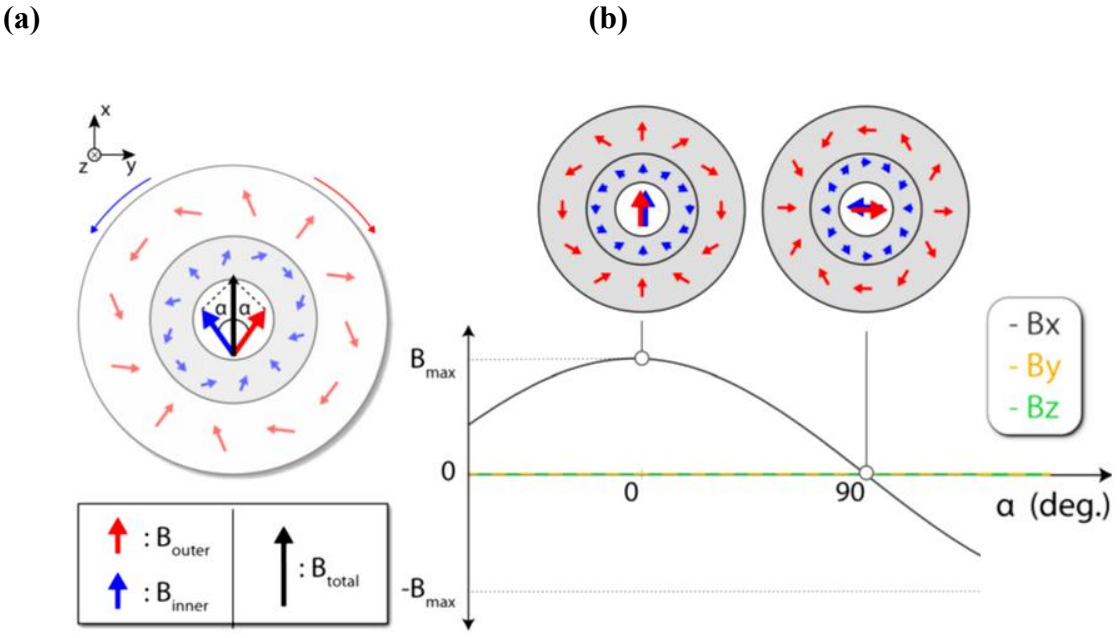

Figure 2.8: (a) The magnetic field created by two cylindrical Halbach dipoles, with the field changing based on the angle between them. The outer cylindrical Halbach is shown with red arrows, while the inner cylindrical Halbach is shown with blue arrows. **(b)** By rotating the nested dipoles in opposite directions, the angle between them can be adjusted to produce a single-axis magnetic field that oscillates uniformly.

2.2.4 Discretized Halbach dipole

The ideal model must be adjusted to turn the idea of nested Halbach dipoles into a feasible design. Practically, it is not possible to create an infinitely long tube with continuously varying magnetized material. Instead, different discrete models have been suggested to approximate this ideal [115]. The simplest approach divides the cylindrical structure into sections that all have the same shape and magnetization but point in different directions [40, 45].

In this thesis, we focus on cylindrical arrays of square-shaped permanent magnets, which act as a discrete version of the ideal Halbach dipoles. These are like the ones shown in Figure 2.7c for a single Halbach dipole and Figure 2.7d for nested Halbach dipoles. For a single discretized Halbach dipole (Figure 2.7c), we can estimate the magnetic field both inside and outside the magnetization plane (the x-y plane, as shown in Figure 2.7). The feasible way to model this cylindrical array consisting of N square-shaped magnets is by treating it as an array of N point dipoles. In this case, the magnetic field (B_{array}) at any point, with radius vector R, is then the sum of the magnetic field B_i from each of the N dipoles at positions r_i.

$$B_{array}(R) = \sum_{i=1}^{N} B_i(R - r_i). \tag{2.23}$$

Based on the approximation presented above, the strength of the magnetic field along the x-axis of the discretized Halbach array can be estimated as a function of the distance from its central plane (i.e., along the z-axis, as shown in Figure 2.8).

$$B_x(x = 0, y = 0, z) = \frac{3}{8} N \mu_0 \frac{mr^2}{\pi(r^2+z^2)^{5/2}}, \tag{2.24}$$

where $\mu_0 = 4\pi \times 10^{-7}\ T\ m/A$ is μ_0 represents the permeability of free space, m is the magnetic dipole moment of each individual dipole (assuming all dipoles, corresponding to each magnet, have the same dipole moment), r refers to the effective radius of the dipole array, and z is the distance from the x-y plane of the Halbach array.

By selecting the optimal configuration, including the dimensions and orientation of the two arrays in a nested Halbach dipole, the strength and uniformity of the resulting magnetic field can be precisely adjusted within the magnetic bore. This feature is essential for designing a device that generates adjustable, uniform magnetic fields in a 3D space, suitable for NMR experiments.

This thesis presents a prototype Halbach magnet suitable for low-field NMR spectroscopy, consisting of three nested Halbach cylindrical arrays. Detailed design and calculations are provided in Chapter 4, Section 4.1: Multilayer Halbach Magnet.

2.3 Optimal control theory

2.3.1 Introduction

Optimal Control (OC) theory, initially developed for optimizing complex dynamic systems in engineering and economics [117], is a powerful tool for designing and optimizing pulse sequences in NMR spectroscopy. This approach, which uses numerical optimization, has proven effective in both liquid- and solid-state NMR [49]. It enhances energy transfer efficiency between specific spin states and allows for shaping the nuclear spin Hamiltonian to desired forms, leading to the development of novel and high-performance pulse sequences [33]. The foundation of OC theory lies in the classical Euler-Lagrange formalism, attributed to Leonhard Euler and Joseph-Louis Lagrange. By employing Lagrange multipliers, this theory reduces a functional subject to constraints, providing a strategic framework for optimizing radiofrequency pulses in NMR [50].

Optimal control methods fall into two categories: gradient-free and gradient-based algorithms. Gradient-based methods, such as Gradient Ascent Pulse Engineering (GRAPE) [118], and the Krotov method [119] typically converge faster and solve a set of coupled equations involving forward and backward propagation of states. GRAPE is suitable for concurrent updates with discrete control parameters, whereas the Krotov method ensures monotonic convergence with sequential updates and avoids the need for line search [120]. The choice of control method depends on the number of control parameters (n) and the nature of the control fields. For piecewise-constant controls, the parameters correspond to values in each time interval [121]. Analytical controls follow a fixed formula parameterized by control parameters [122] while non-analytical methods, such as CRAB, involve random spectral components with adjustable coefficients [123].

Gradient-free methods are preferable when the number of parameters is small, or gradients are difficult to compute. They are often used to generate initial pulses for gradient-based methods. GRAPE is utilized when control parameters are discrete, and gradients are computable, while Krotov's method suits time-continuous controls with calculable functional derivatives. Figure 2.9 [124] illustrates a decision tree for choosing an optimization method based on the number of control parameters and the nature of the controls.

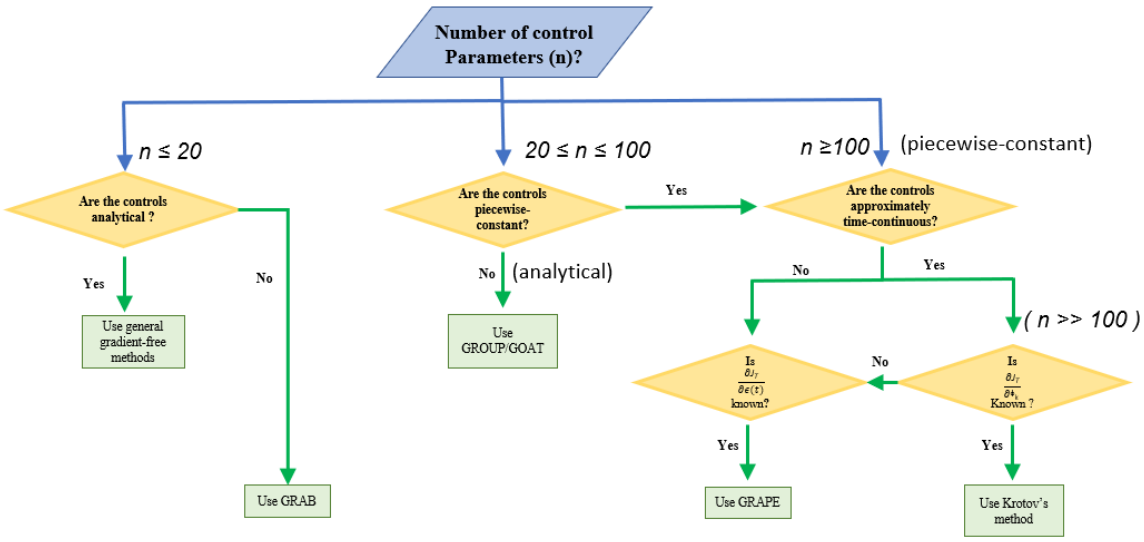

Figure 2.9: Decision tree employed in this dissertation to guide the selection of a numerical open-loop optimization method, ultimately leading to the selection of the Krotov method.

Krotov's method is generally employed for critical tasks like mapping system design landscapes or determining quantum speed limits, assuming time-continuous controls without inherent constraints [53].

Optimal Control (OC) techniques can then be applied to optimize RF pulse shapes for two main objectives: maximizing the efficiency of coherence transfer from an initial spin state ρ_0 to a desired target spin state ρ_D (state-to-state transfer) or achieving a specific effective Hamiltonian. The Liouville-von Neumann equation plays a fundamental role in determining RF pulses applied to coupled spin systems. This equation provides a way to describe the evolution of the spin system using the density operator $\rho(t)$. When relaxation effects are disregarded, the behavior of nuclear spin systems can be modeled effectively by this equation.

$$\frac{d\rho(t)}{dt} = -i[H(t), \rho(t)], \tag{2.25}$$

with the nuclear spin Hamiltonian $H(t)$ and the density matrix $\rho(t)$.

$$\frac{dU(t)}{dt} = -iH(t)U(t), \tag{2.26}$$

where $U(t)$ is the unitary propagator, the nuclear spin Hamiltonian is given by

$$H(t) = H_0 + \sum_k \omega_k I_k\,, \tag{2.27}$$

where H_0 is the system Hamiltonian describes the internal spin interactions and $\sum_k \omega_k I_k$ is the control Hamiltonian, and I_k is the spin operator (typically I_x, I_y, S_x, S_y, etc.) at time *t*. The equation of motion can be expressed as

$$\frac{d}{dt}U_n(t) = -i\left[H_0 + \sum_k \omega_{k,n} I_k\right]U_n(t). \tag{2.28}$$

The Liouville equation is introduced as a constraint using a complex valued operator $B(t)$ (back propagation function) as a Lagrange multiplier. Then, the necessary conditions for its maximum are found by variational principles. The optimal solution of the problem should satisfy

$$\frac{d}{dt}B(t) = -iH(t)B(t) \tag{2.29}$$

$$B(T) = \frac{\partial \emptyset_j}{\partial U(T)} \tag{2.30}$$

$$\omega_k(t) = \frac{1}{\lambda}\mathrm{Im}\{\mathrm{Tr}[B^{\dagger}(t)I_k U(t)]\}. \tag{2.31}$$

By combining Equations 2.29-2.31 with Equation 2.26, only a stationary point whether an extremum or a saddle point of the functional is described. However, these equations alone do not guarantee that the global optimum is reached. Therefore, additional steps are required to verify the location of this extremum.

2.3.2 Krotov-based algorithm

In this work, we employ a Krotov-based optimal control (OC) approach, previously utilized in NMR [53, 54] which is grounded in the global optimal control framework developed by V. F. Krotov [125]. This methodology was initially demonstrated in quantum control by Zhu and Rabitz [126], and subsequently adapted for NMR by Maximov et al., using a density operator formulation [53, 54]. Vinding et al. [127] later extended its application to MRI, employing the Bloch equations. The specific algorithm implemented in this study incorporates stabilized monotonic convergence and pulse shape smoothing [54].

The Krotov algorithm is based on the optimization of a function of the type

$$J_j(\omega_k) = \emptyset_j - \lambda \int_0^T \sum_k \omega_k^2(t)dt, \tag{2.32}$$

where $\emptyset_j$ is the efficiency (fidelity) to be maximized and the second term penalties the deposited power scaled with the weighting factor λ, and T is the duration of the pulse.

$$\emptyset_j = |\mathrm{Tr}(U'_D U)|^2. \tag{2.33}$$

The functional $J_j(\omega_k)$ must be optimized under the constraint of the Liouville Equation 2.25 As $J_j(\omega_k)$ has to remain real valued, the complex conjugate of the Lagrange multiplier term has to be added as well,

$$J_j(\omega_k) = \emptyset_j - \lambda \int_0^T \sum_k \omega_k^2(t)dt - \int_0^T Tr\left\{ B^+(t)\left[\frac{d}{dt}U(t) + iH(t)U(t)\right]\right\} dt$$
$$- \int_0^T Tr\left\{\left[\frac{d}{dt}U^+(t) - iU^+(t)H(t)\right] B(t)\right\} dt. \quad (2.34)$$

The optimization requires derivatives of the functional $J_j(\omega_k)$ with respect to the control parameters to be zero at a stationary point, resulting in the following equations:

$$\frac{d}{dt}B(t) = -iH(t)\, B(t) \quad (2.35)$$

$$B(t) = \frac{\partial \emptyset_j}{\partial U(T)} \quad (2.36)$$

$$\omega_k(t) = \frac{1}{\lambda} ImTr\{[B^+(t)\, I_k\, U(t)]\}. \quad (2.37)$$

As the functional $J_j(\omega_k)$ is supposed to increase with each iteration n, the following expression must be positive,

$$\emptyset_{n+1} = \phi_n - \lambda \sum_k \int_0^T \left[\omega_{k,n+1}^2(t) - \omega_{k,n}^2(t)\right] dt. \quad (2.38)$$

Importing the stationary point conditions and evolving the propagators through a Strang-second-order split-operator method [128, 129], one arrives at

$$f_j(\omega_j') = 2Re\left[Tr\left\{\left(\exp\left(i\Delta t \sum_k \omega_{k,j-1} H_k\right) \exp\left(-i\Delta t \sum_k \omega'_{k,j-1} H_k\right) - E\right) A U'_{j-1} B_{j-1} A^+\right\}\right]$$
$$- \Delta t \lambda \sum_k (\omega'_{k,j-1} - \omega_{k,j-1})(\omega'_{k,j-1} + \omega_{k,j-1}), \quad (2.39)$$

which must be optimized to keep the functional difference positive. Here the primed and unprimed variables refer to iteration number $n+1$ and n, respectively, j denotes the number of the time step of length Δt, $A = e^{-i0.5\Delta t H_0}$ and E is the identity operator. The minimization of $f_j(\omega'_j)$ is started with an appropriate initial guess for the ω_j, using a quasi-Newton optimizer. To take static and RF field inhomogeneity into account, the final cost term $\emptyset$ of the optimal control functional can be replaced by a sum $\sum_j \phi_j$ over a range of conditions,

$$J(\omega_k) = \sum_i |\mathrm{Tr}(U'_D U_i)|^2 - \lambda \int_0^T \sum_k \omega_k^2(t)dt\,, \quad (2.40)$$

where U_D is the desired propagator, U'_D being the adjoint of U_D and the U_i are the propagators corresponding to Hamiltonians (H_i) which characterize the transformation properties of the robust pulse. The H_i are derived as follows: The static field inhomogeneity (SFI) is considered by the introduction of additional chemical shift terms with higher and/or lower resonance frequencies in the system's Hamiltonian, while the control Hamiltonian is left

unchanged. On the other hand, to consider radio-frequency field inhomogeneity (RFI) pre-factors for the control amplitudes are introduced, while the system Hamiltonians are left unchanged. The Hamiltonians H_i are then used for the forward propagation of the U_i and the backward propagation of the B_i in every step of the iteration. The term $AU'_{j-1}B_{j-1}A^{+}$ in Equation (2.33) for the update of the control amplitudes (ω_k) has to be replaced by a sum $\sum_i A_i U'_{i,j-1}B_{i,j-1}A_i^{+}$ over all SFI and RFI conditions, yielding,

$$f_i(\omega'_j) = 2Re\left[Tr\left\{(\exp\,(i\Delta t\sum_k \omega_{k,j-1}H_k)\exp\,(-i\Delta t\sum_k \omega'_{k,j-1}H_k) - E)\sum_i A_i\, U'_{i,j-1}B_{i,j-1}A_i^{+}\right\}\right] - \Delta t\lambda\sum_k(\omega'_{k,j-1} - \omega_{k,j-1})(\,\omega'_{k,j-1} + \omega_{k,j-1}). \quad (2.41)$$

To reduce the exponential growth in computational complexity, which becomes burdensome when calculating pulses for systems with more than 8 spins, the spin system of each chemical compound (I) is modeled with a distinct Hamiltonian ($H_{0,1}$), a distinct propagator ($U_{D,I}$) for the system's evolution, and a set of SFI/RFI propagators ($U_{i,I}$) and back propagators ($B_{i,1}$). The sums over all SFI/RFI conditions, as described in Equations (2.42) and (2.43), are expressed as follows:

$$J = \sum_i |\mathrm{Tr}(U'_{D,l}U_{i,l})|^2 - \lambda\int_0^T \sum_k \omega_k^2(t)dt\,. \quad (2.42)$$

And

$$f_i(\omega'_j) = 2Re\left[Tr\left\{(\exp\,(i\Delta t\sum_k \omega_{k,j-1}H_k)\exp\,(-i\Delta t\sum_k \omega'_{k,j-1}H_k - E)\sum_i A_{i,l}\, U'_{i,j-1,l}B_{i,j-1,l}A_{i,l}^{+}\right\}\right] - \Delta t\lambda\sum_k(\omega'_{k,j-1} - \omega_{k,j-1})(\,\omega'_{k,j-1} + \omega_{k,j-1}). \quad (2.43)$$

2.4 Dipolar coupling

In NMR spectroscopy, the primary interaction is the Zeeman interaction, while chemical shielding and dipolar interactions are considered perturbations [130]. Dipolar coupling represents the direct magnetic interaction between dipoles and is described by a Hamiltonian that includes secular terms, which survive time averaging in the rotating frame, and non-secular terms, which oscillate rapidly and average out [131].

For homonuclear coupling (same isotopes), flip-flop terms cause transitions between states of coupled spins, leading to peak splitting or multiplet formation. This effect can be mitigated by increasing the external field strength or the magic angle spinning (MAS) rate

The dipolar Hamiltonian for identical spins is given by Equation (2.44) [132, 133]:

$$H^{dip} = \sum_{i>j} \omega_{ij}^{D,dip} \; D_{00}^2(\Omega_{ij}^{PL,dip}) \left(2I_{iz}I_{jz} - \frac{1}{2}(I_{i+}I_{j-} + I_{i-}I_{j+})\right), \tag{2.44}$$

in which the sum over all pairs of nuclei, $\omega_{ij}^{D,dip} = -\mu_0 \gamma_I^2 \hbar / 4\pi r_{ij}^3$ is the homonuclear coupling, in which r_{ij} is the internuclear distance, and $\Omega_{ij}^{PL,dip}$ is the set of Euler angles for the transformation from the principal axis system of the dipolar interaction tensor to the laboratory frame. The term $\frac{1}{2}(I_{i+}I_{j-} + I_{i-}I_{j+})$ represents spin-flip interactions for spin i, accounting for non-secular terms in the dipolar Hamiltonian. The I_{i+}, I_{j+} and I_{i-}, I_{j-} are the spin raising and lowering operators for spin i and j respectively.

The Zeeman Hamiltonian is defined as:

$$H_Z = -\gamma \hbar B_0 \left(I_{z_1} + I_{z_2}\right), \tag{2.45}$$

where B_0 represents the static field. The Hamiltonian of the local field (B_{loc}) created by spin 1 at the location of spin 2 can be approximated as:

$$B_{loc} \cong \frac{\gamma \hbar}{r^3} m_1, \tag{2.46}$$

where m_1 is $\pm 1/2$. In the case of nuclei, $\gamma_n, r = a \sim 3A$, and the magnitude of the local field is in the order of $\sim 10^{-4}$ T . The line broadening $\Delta\omega$ resulting from the dipolar coupling with the surrounding spin bath can be expressed as:

$$\frac{\Delta\omega}{\omega} = \frac{B_{loc}}{B_0} \cong 10^{-4}. \tag{2.47}$$

2.5 Dipolar decoupling: multiple-pulse NMR line narrowing

The J-coupling interaction, represented by the tensor J, has the Hamiltonian:

$$H_J = I \cdot 2\pi \cdot J. \tag{2.48}$$

For identical spins, the dipolar Hamiltonian governing magnetic coupling is:

$$H_D = -\frac{\gamma^2 \hbar^2}{r^3} I_{z_1} I_{z_2} (3\cos^2\theta - 1), \tag{2.49}$$

where γ is the nuclear magnetogyric ratio of the spins, r is the internuclear distance, θ is the angle between internuclear vector r and the static magnetic field B_0 along the z-axis in the laboratory frame. By applying a sequence of four $\pi/2$ pulses, dipolar coupling can be reduced or eliminated under appropriate conditions [59, 134, 135].

Various methods, such as magic angle spinning (MAS), homonuclear dipolar decoupling, and broadband heteronuclear decoupling, are used to decrease the linewidth of NMR peaks caused by dipolar couplings. While MAS can theoretically eliminate homonuclear dipolar couplings, practical constraints often limit its effectiveness, especially with strong ^{1}H–^{1}H interactions. In biological systems, MAS can be invasive. An alternative method is multiple-pulse line narrowing, using pulse sequences like WAHUHA to average out dipolar interactions.

The WAHUHA sequence, proposed in [66, 136] removes first-order dipolar terms in the average spin Hamiltonian, achieving efficient decoupling :

$$H_{eff} = \frac{\gamma^2\hbar^2}{r^3} I_{z_1} I_{z_2} . \frac{1}{6r} [1 \times 2\tau + 1 \times \tau - 2 \times 2\tau + 1 \times \tau] = 0, \quad (2.50)$$

where τ represents the time interval between pulses. During the sequence, the magnetic moments spend equal amounts of time along each of the three principal axes. The NMR signal is sampled during one of the 2τ windows. This sequence can be combined with its mirror image to suppress angle errors, forming the MREV-8 pulse sequence [137].

2.6 Water suppression

Various techniques are employed in NMR spectroscopy to suppress the signal from water molecules, allowing for clearer observation of other components. Common water suppression techniques [72, 138-141] include:

- Pre-saturation [142]: This technique involves applying a continuous wave of radiofrequency energy at the resonance frequency of water before the actual NMR experiment. It saturates the water signal, reducing its intensity during subsequent scans.
- Excitation Sculpting [72]: This commonly used method significantly diminishes the water signal, sometimes by a factor of up to 10,000 or more. It selectively excites and dephases the water signal through a series of RF pulses.
- Watergate [140]: This technique uses a combination of pulsed field gradients and selective excitation to suppress the water signal. By introducing gradients and selective excitation pulses.
- PURGE [141]: PURGE (Pre-saturation Utilizing Relaxation Gradients and Echoes) is a straightforward method that requires adjustments only in solvent frequency and pre-saturation power. Known for its high selectivity, preferential phase properties, and stable baselines, PURGE operates with just four scans and integrates smoothly with multidimensional techniques like TOCSY.

Each technique has its strengths and limitations, and the choice often depends on the specific requirements of the experiment and the nature of the sample being analyzed.

3 Experimental methodology and procedures

The chapter gives a description of the experimental methodology and procedures of NMR spectrometer, materials, chemicals, and sample preparations.

3.1 Materials and chemicals

- **Acetic acid**, also known as ethanoic acid, has the chemical formula CH_3COOH (also represented as $C_2H_4O_2$). This organic compound has a molar mass of 60.052 g/mol and a melting point of 16–17 °C (289–290 K). Its chemical structure (Figure 3.1) consists of a methyl group ($-CH_3$) bonded to a carboxyl group ($-COOH$) [143]. Acetic acid is an important building block in organic chemistry, [144] with the methyl group contributing hydrophobic properties and the carboxyl group enabling hydrogen bonding, acid-base reactions, and nucleophilic acyl substitution. Acetic acid (100% purity) was obtained from Sigma-Aldrich (CAS No. 64-19-7, Germany) and was used as received for NMR analysis.

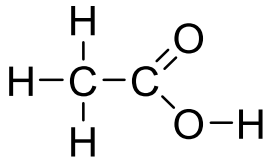

Figure 3.1: Chemical structure of acetic acid ($CH_3 - COOH$).

- **Alanine (Ala)** (2-Aminopropanoic acid) is an α-amino acid used in the biosynthesis of proteins. It has a molar mass of 89.094 g/mol and a melting point of 258°C (531 K). Its chemical formula is $C_3H_7NO_2$, and its chemical structure, shown in Figure 3.2, consists of an amino group ($-NH_2$) bonded to a carboxyl group ($-COOH$). Alanine is an important building block in protein synthesis. It was obtained from Sigma-Aldrich (CAS No. 56-41-7, Germany) and used without further processing.

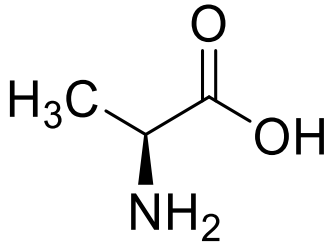

Figure 3.2: Chemical structure of Alanine ($CH_3 - CH(NH_2) - COOH$).

- **Benzoic acid (BA)** (benzenecarboxylic acid) has a molar mass of 122.123 g/mol and a melting point of 122°C (395 K). Its chemical formula is C_6H_5COOH, and its chemical structure, shown in Figure 3.3, consists of a benzene ring bonded to a carboxyl group (-

COOH). Benzoic acid is an important intermediate in various metabolic pathways, especially in the biosynthesis of aromatic compounds. It was obtained from Sigma-Aldrich (CAS No. 65-85-0, Germany) and used without further processing.

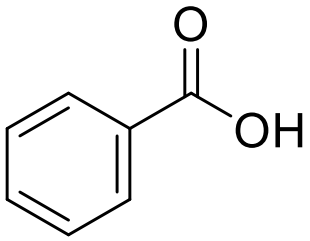

Figure 3.3: Chemical structure of Benzoic acid ($C_6H_5 - COOH$).

- **Cyclopentenone** is a ketone with a chemical formula of C_5H_6O and a molar mass of 94.10 g/mol. It contains two functional groups: a ketone group and an alkene group (Figure 3.4). Cyclopentenone is an important intermediate in organic synthesis, particularly in the formation of more complex organic compounds. It is used in the synthesis of pharmaceutical compounds and can also be found in certain biological processes. It was obtained from Sigma-Aldrich (CAS No. 930-30-3, Germany) and used without further processing.

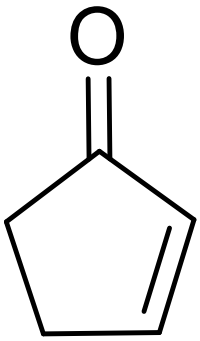

Figure 3.4: Chemical structure of cyclopentenone (C_5H_6O).

- **Phenylalanine (Phe)** is an essential α-amino acid, with the L-isomer known as (S)-2-amino-3-phenylpropanoic acid, chemical formula $C_9H_{11}NO_2$, and a molar mass of 165.19 g/mol. It features a nonpolar, hydrophobic benzyl side chain and is crucial for protein synthesis. Additionally, phenylalanine serves as a precursor for tyrosine, dopamine, norepinephrine, epinephrine, and melanin. It was obtained from Sigma-Aldrich (CAS No. 63-91-2, Germany) and used without further processing. The chemical structure is shown in Figure 3.5.

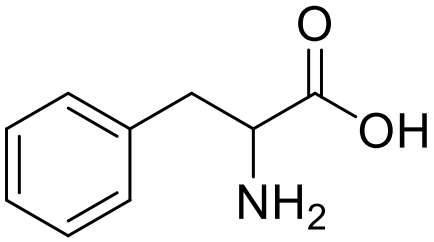

Figure 3.5: Chemical structure of Phenylalanine ($C_6H_5 - CH_2 - CH(NH_2) - COOH$).

- **Taurine (Tau)**, or 2-aminoethanesulfonic acid, has the chemical formula $C_2H_7NO_3S$ and a molar mass of 125.14 g/mol. It was obtained from Sigma-Aldrich (CAS No. 107-35-7, Germany) and used without further processing. Taurine is a non-proteinogenic amino sulfonic acid found in animal tissues. It is a major component of the bile and is present in the large intestine, where it accounts for up to 0.1% of total human body weight. The melting point is 305.11°C (578.26K), and the chemical structure is shown in Figure 3.6.

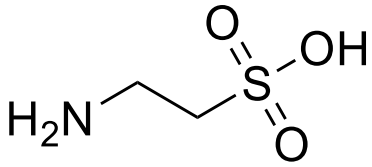

Figure 3.6: Chemical structure of Taurine ($H_2N— CH_2— CH_2— SO_3H$).

- **Agarose gel:** We used Agarose (A2929, Sigma Aldrich; low electroendosmosis (EEO)-type (≤ 0.08), sulfate content ≤ 0.20%) [145], typically derived from red algae, such as *Gelidium* and *Gracilaria*. Chemically, agarose is a linear polysaccharide of repeating D-galactose and 3,6-anhydro-L-galactose units, linked by β-(1→4) and α-(1→3) glycosidic bonds [146]. This structure enables agarose to form a stable gel matrix when dissolved in water and cooled, making it ideal for NMR experiments. The gel mimics the viscosity and consistency of biological fluids and tissues, immobilizing metabolites, reducing diffusion, and enabling dipolar coupling during NMR measurements [147].

Mimicking real biological fluids and tissue-like environments that more closely replicate their native state within biological systems [148]. Dipolar coupling, which arises from the interactions between nuclear spins, causes broadening in NMR spectra. This broadening leads to a reduction in spectral resolution, which can obscure fine details in the NMR line shape. In this work, by using agarose gels, dipolar coupling is introduced and sustained, allowing for the development and testing of NMR pulse sequences designed to mitigate its effects. The viscosity of agarose gels, which can be adjusted by varying the concentration (typically between 0.5% to 2%), replicates the rheological properties of biofluids and tissues

[149]. The preparation of agarose for NMR applications involves dissolving agarose powder in water, heating it to fully dissolve, and allowing the solution to cool and solidify into a gel. The concentration and other experimental parameters, such as pH and temperature, are optimized based on the specific viscosity required and the nature of the metabolites under investigation.

- **Solvents: i)** Deuterium oxide (D_2O) was obtained from Sigma-Aldrich (CAS No. 7789-20-0, Germany). **ii)** Dimethylsulfoxid-d6 (DMSO-d6), also known as Hexadeuterodimethylsulfoxid, with the chemical formula $(CD_3)_2SO$, has a molar mass of 78.14 g/mol. It was obtained from Sigma-Aldrich (CAS No. 2206-27-1, EG No. 218-617-0, Germany) and used without further processing. DMSO-d6 is primarily used as a solvent in NMR spectroscopy due to its deuterated form.

- **NMR references: i)** Tetramethylsilane (TMS), with the chemical formula $(CH_3)_4Si$, has a molar mass of 88.22 g/mol. It was obtained from Sigma-Aldrich (CAS No. 75-76-3, Germany) and used without further processing. Tetramethylsilane is primarily used as a reference standard in NMR spectroscopy, including in the analysis of cyclopentenone, due to its non-reactivity and chemical inertness. **ii)** 3-(Trimethylsilyl)-propionic-2,2,3,3-d_4 acid sodium salt (TSP), with the chemical formula $(CH_3)_3SiCD_2CD_2CO_2Na$, has a molar mass of 172.27 g/mol. It was obtained from Sigma-Aldrich (CAS No. 24493-21-8, Germany) and used without further processing. TSP is primarily used as a reference standard in NMR spectroscopy due to its stable and inert nature.

- **NMR tubes:** High-resolution 5 mm borosilicate glass NMR tubes (Boro-600-5-8) were sourced from Deutero GmbH, Kastellaun, Germany. Borosilicate glass capillary tubes with an outer diameter (OD) of 1.7 mm, an inner diameter (ID) of 1.3 mm, and a length of 100 mm were provided by Hilgenberg (Art.-Nr. 2001710, Essen, Germany).

3.2 NMR samples

3.2.1 Sample preparation

The cyclopentanone NMR sample was prepared by mixing 1 mL of cyclopentanone with 5% DMSO-d6 (v/v), adding 50 µL of DMSO-d6 to the 1 mL of cyclopentanone. The sample was mixed well and 500 µL was transferred to the 600 MHz high-resolution NMR tube. For low-field NMR measurements, 20 µL of the sample was used.

An equimolar mixture of Phe and Tau was prepared in D_2O with a total volume of 500 µL. Each component was initially prepared at a concentration of 10 mM (0.05 moles per 100 mL). For the final mixture, 200 µL of phenylalanine was combined with 200 µL of taurine. Additionally, 1 mg of TSP was dissolved in 100 mL of D_2O, and 10 µL of this TSP solution was added to the sample.

For low-field NMR samples, Phe-Tau was prepared with phenylalanine and taurine at a concentration of 0.1 mole per 100 mL (10 mM). Subsequently, 10 µL of phenylalanine was mixed with 10 µL of taurine. Additionally, 1 mg of TSP was dissolved in 100 mL of D_2O, resulting in a 10 mL TSP solution. The sample was mixed externally using a microsyringe and then injected into a standard borosilicate 3 mm outer diameter (OD) and 2.8 mm inner diameter (ID) NMR tube.

Similarly, an equimolar mixture of benzoic acid and alanine was prepared using the same procedure as for Phe and Tau, with the same concentration of 10 mM for each component, and 1 mg of TSP dissolved in 100 mL of D_2O. The sample was prepared and injected into the same NMR tube as described above.

3.2.2 Agarose gel preparation

Agarose (A2929, Sigma Aldrich; low electroendosmosis (EEO)-type (≤ 0.08), sulfate content ≤ 0.20%) was used to prepare agarose gels to increase solution viscosity and reduce molecular diffusion, enabling improved NMR dipolar coupling measurements for the WAHUHA experiment in this study. Solutions with agarose concentrations of 0.05 wt.%, 0.1 wt.%, 0.15 wt.%, 2 wt.%, 2.5 wt.%, 3 wt.%, and 4 wt.% were tested. Agarose powder was gradually added to D_2O while stirring at 500 rpm on a magnetic stirrer. The mixture was then heated in a microwave at 700 W for 12 seconds to dissolve the agarose completely, ensuring uniformity while preventing overboiling to maintain the D_2O ratio.

A concentration of 1.5 wt.% was selected as optimal for achieving a balance between viscosity, dipolar coupling, and spectral broadening, as shown in Figure 5.15. This concentration provided sufficient viscosity to mimic biological fluids and reduce molecular diffusion, enhancing the localization of dipolar coupling in NMR measurements.

3.3 NMR experiments

3.3.1 High-field NMR spectrometer

A broadband high-resolution NMR spectrometer (Bruker Avance III 600, operating at 600.13 MHz, $B_0 = 14.1\,T$, equipped with a Bruker ASCEND 600 magnet) was used to

acquire ^{1}H-NMR spectra. The setup included room-temperature probes (PA BBO 600S3 BBF-H-D-05 Z SP) and HRMAS probe-heads for high-resolution analysis. These multipurpose probes feature an inner coil tunable for nuclei within a frequency range spanning ^{31}P and ^{15}N, while the outer coil is optimized for ^{1}H decoupling and observation. This configuration supports automated acquisition on protons and a variety of X-nuclei through a broadband frequency channel. Samples were analyzed in high-resolution 5 mm NMR tubes (Wilmad, Boro-600-5-8, 7”), compatible with the specified probe-heads. NMR data acquisition and spectral processing were performed using the TopSpin® software package (version 3.7).

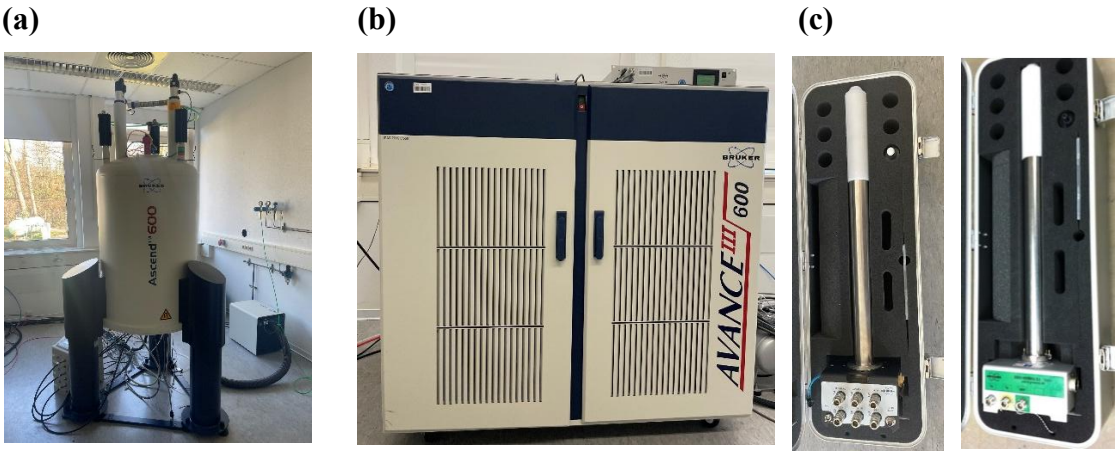

Figure 3.7: High resolution 600.13 MHz ($B_0 = 14.1\ T$) NMR Bruker spectrometer (Avance III 600) with the **(a)** Bruker magnet ASCEND 600, **(b)** Avance III 600 console and **(c)** room temperature (PA BBO 600S3 BBF-H-D-05 Z SP) and HRMAS probeheads.

3.3.2 Magic angle spinning (MAS)

MAS NMR is used for heterogeneous samples and those with restricted molecular motion, such as semi-solids. In these samples, spatial variations in magnetic susceptibility cause position-dependent differences in magnetization, leading to signal broadening. Additionally, dipolar couplings between nuclear spins [150] and chemical-shift anisotropy (CSA) contribute to the broadening [150]. MAS NMR reduces these dipolar couplings and anisotropic interactions by rapidly rotating the sample around an axis tilted at 54.74° relative to B_0. This averaging of dipolar couplings and CSA results in narrower peaks, transforming the NMR spectrum to resemble that of liquid-state NMR [151]. Furthermore, MAS mitigates inhomogeneities caused by variations in magnetic susceptibility [152-154].

NMR data acquisition, processing, and analysis were performed using TopSpin 3.7 software package [155] and results were plotted and arranged using OrginLab2022.

4 Low-field NMR spectrometer

In this dissertation, a low-field NMR spectrometer (LF-NMR) was developed using a multilayer Halbach magnet equipped with mechanical and electrical shimming systems, resulting in improved field homogeneity and sensitivity over conventional Halbach and dipole magnets. The magnet design incorporates three nested cylindrical magnets with an inner Halbach layer, which allows for rotational adjustments to facilitate precise mechanical shimming.

Chapter 4 provides an in-depth analysis of the design, fabrication, validation, and operational principles of the LF-NMR spectrometer. This chapter details the manufacturing process, along with the challenges and solutions involved in optimizing the spectrometer for low-field NMR spectroscopy. Additionally, the integration of control pulses for selective molecular excitation in aqueous metabolite solutions was implemented to address signal overlaps and enhance quantification accuracy in low-field NMR spectra. This methodology improves spectral resolution, thus providing a more reliable tool for metabolite analysis under low magnetic field conditions.

The design and fabrication of the multilayer Halbach magnet are discussed in later chapters, along with the radiofrequency and thermally isolated enclosure, which ensures both the thermal stability of the magnet and the precise positioning of the probehead at the sweet spot within the magnet bore.

4.1 Multilayer Halbach magnet

4.1.1 Prototype version 1: Initial development and testing

In this work, we developed a customized design for the Halbach magnets, informed by literature on multilayer Halbach arrays [112, 156]. Our design incorporates new developments, culminating in a three-layer Halbach array configuration. This initial design does not include mechanical or electrical shimming and was for the low-field NMR spectrometer.

The first operating low-field spectrometer was equipped with an early prototype of a custom-built multilayer Halbach magnet, generating a field strength of 0.486 T, corresponding to an operating frequency of 21.25 MHz for protons. Figure 4.1 shows the initial prototype, featuring a two-layered Halbach design with additional quadrupole magnets to bolster the magnetic field strength. The completed magnet is annotated with magnetic field directions and the resultant magnetic field within the magnet bore.

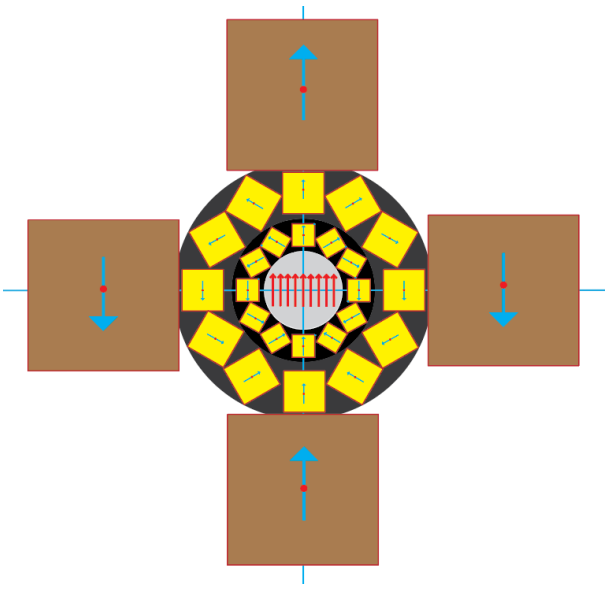

Figure 4.1: The assembled multi-layered Halbach magnet with annotations indicating the magnetic field direction of the magnetic elements and the resultant magnetic field within the magnet bore. The design was created using Inkscape 0.90.

The Halbach magnet layout design was replicated using a computerized grinding machine located at ISAS, Dortmund, as shown in Figure 4.2 (a and b). Subsequently, this pattern was etched onto 12 aluminum plates, each measuring 150×150 mm (Figure 4.2c).

(a) **(b)** **(c)**

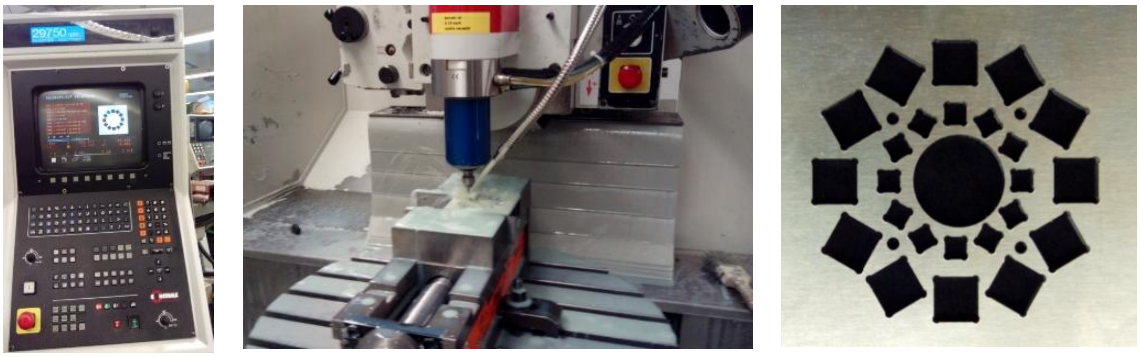

Figure 4.2: (**a** and **b**) Computerized grinding machine located in ISAS demonstrating the process of preparing one aluminum plate with the Halbach array pattern as depicted in (**c**).

Subsequently, the plates were stacked together and fixed with rectangular $40 \times 40\ mm$ slots on each side to accommodate the four quadrupole magnet elements, as illustrated in Figure 4.3. This early prototype of a custom-built multilayer Halbach magnet was not supported by mechanical or electrical shimming systems. However, the wide bore of the magnet allowed for adjusting the position of the NMR detector to achieve homogeneity within the magnet bore.

The early prototype of a custom-built multilayer Halbach magnet was finalized by arranging

the magnet elements in the first layer with dimensions of $5 \times 5 \times 5\ mm$, following the Halbach array pattern as shown in Figure 4.1. Similarly, the second layer was arranged with elements sized $10 \times 10 \times 10\ mm$. Additionally, the four quadrupole magnet elements were positioned in the quadrupole slots on the sides of the stacked aluminum plates, as illustrated in Figure 4.1.

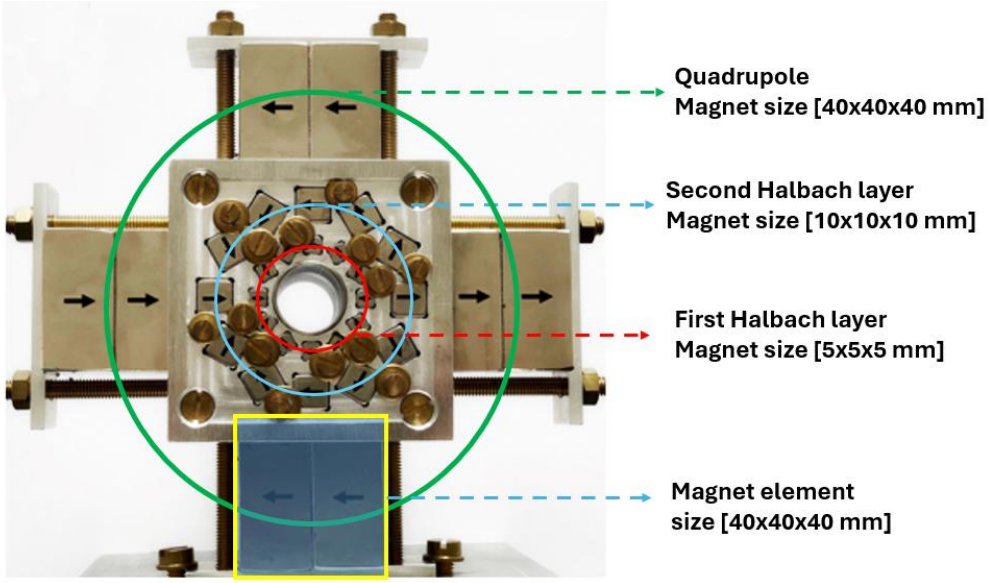

Figure 4.3: Early prototype of a custom-built multilayer Halbach magnet generating a field strength of 0.486 T. The diagram illustrates the two Halbach layers, quadrupole magnets [$40 \times 40 \times 40\ mm$], color-coded Halbach layers and magnet elements for clarity.

The Halbach magnet characterization and sweet point determination was determined by using a water sample enclosed within a glass capillary measuring 1.7 mm in diameter and 1.3 mm in length, employing the same method as described in Section 4.1.4 and B_0 homogeneity of the early prototype of a custom-built multilayer Halbach magnet is $\frac{\Delta B_0}{B_0} = 10^{-4}$. This characterization was performed utilizing a home-built on-board NMR probe, which was also utilized for subsequent NMR measurements. The on-board NMR probehead (Figure 4.4c) is custom-built and incorporates non-magnetic and multi-turn tuning and matching trim capacitors from Voltronics Corp., Salisbury, MD, USA. These capacitors were utilized to achieve resonance at 21.25 MHz. Additionally, the probehead features a 12-turn solenoidal micro-coil wound around a high-resolution glass capillary with an outer diameter (OD) of 1.7 mm and an inner diameter (ID) of 1.3 mm. The specifics of the home-built on-board NMR probe are outlined in Section 4.2.1.

To ensure RF shielding and stable temperature conditions, the NMR setup was housed in a home-built thermal isolation metallic aluminum box with a wall thickness of 2 mm. Temperature control was facilitated by a programmable standalone commercial temperature

controller. Mechanical vibrations with frequencies exceeding 0.6 Hz were suppressed using an active vibration isolation system from Halcyonics GmbH, Göttingen, Germany, while ultra-low vibrations were mitigated using a passive vibration isolation table. The portable NMR spectrometer was controlled using the NMR console from SpinCore Technologies, Inc., and the entire setup is depicted in Figure 4.4b. The details of the home-built thermal isolation metallic aluminum box and the 3D-axis micrometers are outlined in Section 4.2.2.

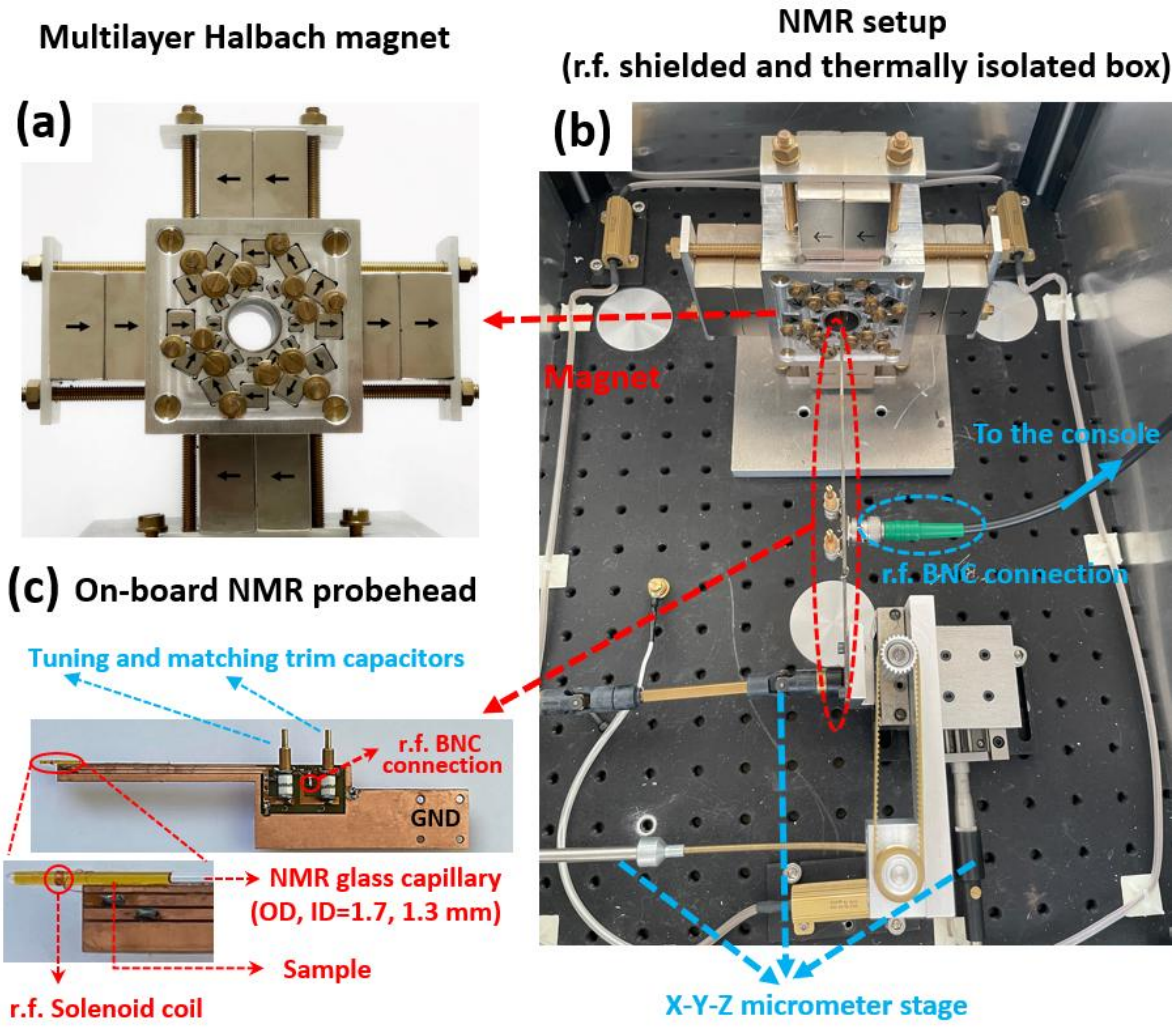

Figure 4.4: (a) Early prototype of a custom-built multilayer Halbach magnet. **(b)** NMR setup with RF shielded thermally isolated box. **(c)** On-board NMR probehead comprising tuning and matching trim capacitors, RF BNC connection, RF solenoid coil, NMR glass capillary ($OD = 1.7\ mm$, $ID = 1.3\ mm$), and ground coupling (GND).

4.1.2 Prototype version 2: Advanced features and performance

The new multi-layered Halbach magnet design is based on three Halbach arrays, with each layer constructed by arranging identical cubic magnets in a circular configuration. This arrangement results in the constructive summation of magnetic fields within the interior of the ring, generating a dipolar field [5]. The design builds upon the concept of the NMR

Halbach cylinder by incorporating three nested Halbach arrays (Figure 4.5a). To enhance precision, 3D printing technology was employed to fabricate the magnet matrix, the rotatable shimming Halbach array, and the electrical shimming kernel. A key innovation in this design is the integration of a rotatable shim cylinder, which provides an adjustable compensating magnetic field to improve field homogeneity [46].

The cubic magnet elements (i) within the Halbach cylinder are positioned at an angle $\alpha_i = 2\pi i/n$ (i = 0, 1, .., n − 1), with their magnetization axis rotated relative to the z-axis (Figure 4.5a). Identical magnets with edge length a_l (where l corresponds to the layer number, ranging from 1 to 3) are placed with their center vectors (${}^{c}P_i$), representing the vector from the center of the Halbach layer to the center of each magnet element (expressed in Equation 4.1 and illustrated in Figure 4.5). These magnets are positioned at an angle α_i on a circle of radius r. The Halbach cylinder's characteristics are defined by parameters such as the ring radius r (indirectly related to magnet size), the number of cubic magnets (n), and the remanent magnetization [3, 5]. Each corner is represented by a vector ${}^{j}\boldsymbol{P}_i$, j ranges from 1 to 4 (representing the cube vertices), and i varies from 0 to $n-1$, where n corresponds to the number of magnets. These vectors are numbered clockwise from the center of each magnet and are defined as [40, 157, 158].

$$ {}^{j}\boldsymbol{P}_i = {}^{c}\boldsymbol{P}_i + \frac{a}{\sqrt{2}} \cdot \begin{pmatrix} \cos\left[\frac{2j-1}{4}\pi - \frac{4\pi}{n}\right] \\ \sin\left[\frac{2j-1}{4}\pi - \frac{4\pi}{n}\right] \end{pmatrix} \text{ and } {}^{c}\boldsymbol{P}_i = r \cdot \begin{pmatrix} \sin(\alpha_i) \\ \cos(\alpha_i) \end{pmatrix}, \tag{4.1} $$

The inner (r_{inner}), and outer (r_{outer}) radii, measured from the center of each cube positioned at a radius (r) within a specific layer, are determined by Equation 4.2:

$$ r_{inner} = r \cdot (1 - \sqrt{2}\ \Xi(n)),\ r_{outer} = r \cdot (1 + \sqrt{2}\ \Xi(n)), \tag{4.2} $$

where n is the number of the magnetic elements, r is the radius of the central cylinder line of each layer (r_1: radius of layer 1, r_2: radius of layer 2, r_3: radius of layer 3). The parameter $\Xi(n)$ relates to the geometry and volume of the Halbach cylinder and can be approximated as $\Xi(n) \approx 2.26/(n-1.6)$ for $n > 4$ [40, 45].

The vertex coordinates (V_c) in polar coordination is given by

$$ V_c = {}^{c}P_i + \sqrt{2}\ r\ \Xi(n) \cdot \begin{pmatrix} \cos\left[\frac{2j-1}{4}\pi - \frac{4\pi}{n}i\right] \\ \sin\left[\frac{2j-1}{4}\pi - \frac{4\pi}{n}i\right] \end{pmatrix}, \tag{4.3} $$

The assembled three-layered Halbach magnet annotated with the magnetic field direction of the magnetic elements and the resultant magnetic field in the magnet bore is visualized in Figure 4.5b.

(a)

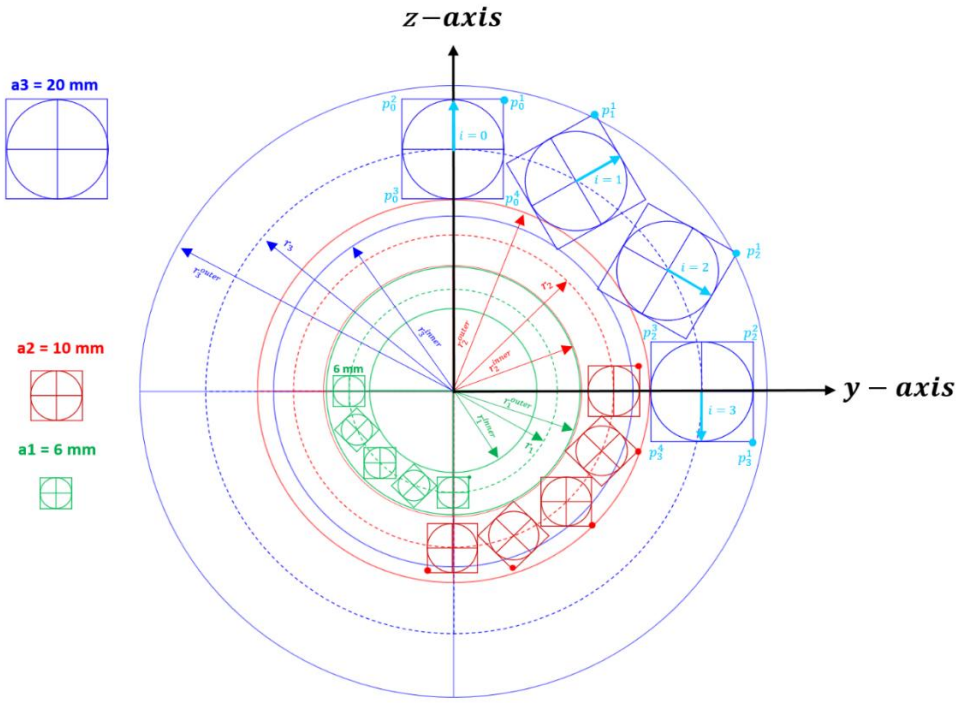

(b)

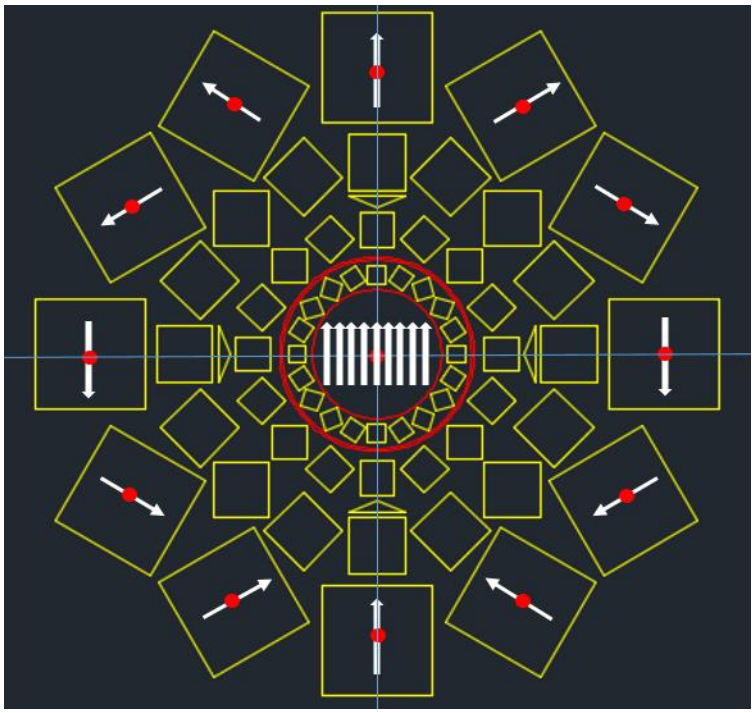

Figure 4.5: (a) Construction principle of Halbach cylinder where identical magnets of size a are located with their center vectors, ${}^{c}P_i$ at an angle α_i on a circle of radius r. The three-layered Halbach magnet was designed with AutoCAD based on the Halbach condition for every individual layer to add constructively to (B_z) and eliminate other directional magnetic components. **(b)** The visualization of the assembled three-layered Halbach magnet annotated with the magnetic field direction of the magnetic elements and the resultant magnetic field in the magnet bore.

The magnetic moment (m) of the multilayer Halbach magnet is calculated as $m = M \cdot V$, where M and V correspond to the magnetization and the volume of a single cube magnet, respectively. For cube magnets, the volume of a cylindrical Halbach array can be expressed as $2r\Xi(n)$, leading to $m = M(2\,r\,\Xi(n))^3$.

For the multilayer Halbach magnet, the z-component of the magnetic field along the x-axis (aligned with the magnet bore and referred to here as x) is calculated as the summation of the contributions from all three layers at a specific x-point on the centerline of the magnet bore (see Figure 4.7c).

$$B_z(x) = B_R \sum_{l=1}^{3} \frac{\left(\frac{3}{\pi} n_l\, \Xi(n_l)\right)^3}{\left(1+\left(\frac{x}{r_l}\right)^2\right)^{3/5}}\ , \tag{4.4}$$

l denotes the layer order, starting from the concentric point of the layers (n_l: $n_1 = 16, n_2 = 16, n_3 = 12$) and $B_R = \mu_0 \cdot M$ represents the remanence of the individual magnets. To calculate the magnetic field of the multilayer Halbach magnet, which consists of multiple stacks in the x-direction, each Halbach stack (comprising 3 rings) can be treated as a dipole. The superposition of these terms leads to the following expression:

$$B_z(x) = \frac{6B_R}{\pi} \sum_{K=0}^{\infty} \sum_{l=1}^{3} \frac{n_l((\Xi(n_l))^3}{(1+((\Xi(n_l))^2(1+2k)^2)^{5/2}}\ . \tag{4.5}$$

Figure 4.6 shows the numerical solution of Equation 4.5 for the field along the x-axis (x as we denoted. The numerical solution is obtained for the studied finite stack, which is oriented in the x- direction of the multilayer Halbach magnet comprising the three layers.

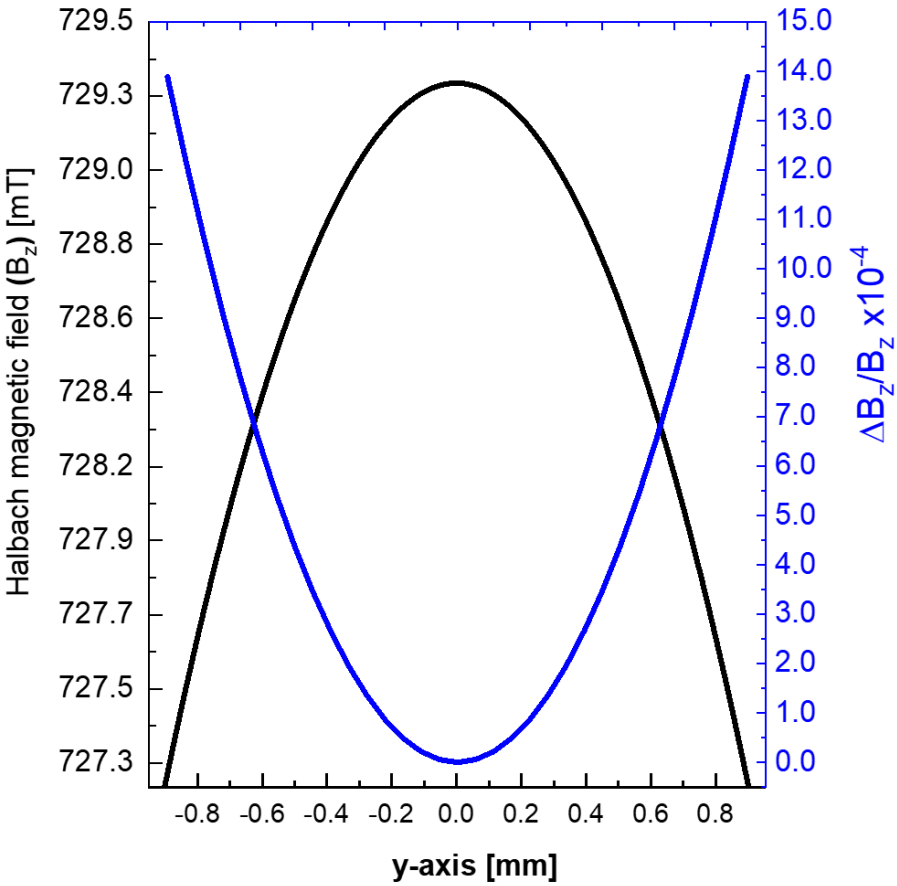

Figure 4.6: The absolute z-component of the magnetic field (B_z) along the x-axis (black curve), which is aligned with the magnet bore, is analyzed for a three-layer concentric Halbach magnet configuration. This design results in the summation of the z-component of the magnetic field to form B_z, while the magnetic field components in the $x-$ and $y-$directions are minimized at the sweet spot. The blue curve illustrates the relative field inhomogeneity, represented as $\Delta B_z/B_z$. The axes are illustrated in Figure 4.7b.

The relative field inhomogeneity ($\Delta B_z/B_z$) along the x-axis was analytically calculated, following the comprehensive description by H. Soltner and P. Blümler [110]. Consequently, the Multilayer Halbach Magnet (MLHM) exhibits a field inhomogeneity of approximately 140 ppm across the sample volume in the absence of the combined shimming system. Specific parameters, including, r_{inner}, r_{outer}, and r for the completed Halbach magnet, are provided in Table 4.1.

Table 4.1: The key parameters for the 3-Halbach layers and the rotatable shimming layer, including r_{inner}, r_{outer} and r values. Additionally, it lists the sizes and magnetic remanence (B_R) of the cubic magnet elements within each layer, along with the magnetic field $B_z\ (x)$at the coordinates $(x, y, z\ =\ 0)$.

Layer ***(l)*** **[#]**	***n*** [#]	r_{inner} [mm]		r_{outer} [mm]		r [mm]		***size*** [mm]	B_R [mT]	$B_z\ (x)$ $at\ (x, y, z = 0)$ [mT]
		Cal.	Mea.	Cal.	Mea.	Cal.	Mea.	As received		Cal.
1	16	15.9	16.0	25.1	25.2	20.5	20.5	6×6	1350	230.6
2	16	24.8	25.0	37.95	37.75	31.0	31.0	10×10	1350	215.3
3	12	35.5	36.0	60.0	60.2	47.0	47.0	20×20	1350	282.9
Mini-ring Halbach mechanical shimming [layer 0]										
0	20	11.2	11.4	18.3	18.7	13.8	14.1	3×3	1320	123.98

Cal.: Calculated, Mea.: Measured.

4.1.3 Fabrication and validation

The Multilayer Halbach Magnet (MLHM) developed in this study is a three-layer cylindrical magnet with a nested, rotatable inner layer (Halbach array) for mechanical shimming (Figure 4.7a). The design of the rotatable mechanical shimming layer was carried out using 3D CAD and finalized using a high-resolution 3D printer (FelixPrinter FFF 3D Printer). Sintered magnet elements of Neodymium-Iron-Boron (NdFeB) grade N42 were purchased (Ningbo Permanent Magnetic Materials Ltd.-NGYC, Yinxian Ningbo). The individual magnets are nickel-coated cubes with side dimensions of $20, 10, 6, \text{and } 3$ mm ± 0.05 mm.

The remanence is $B_R = 1350$ mT, coercivity $H_c = 923\ kA/m$ and maximum energy product $(BH)_{max} = 318.3$ KJ/m^3 , $= 42$ MGOe). Furthermore, the completed Halbach array includes a quadrupole layer comprising four ferromagnetic cubes, each with a side dimension of 40 mm, made of ferromagnetic steel and coated with nickel.

This quadrupole layer is designed to manipulate magnetic field lines, concentrating and bending them to strengthen the magnetic field and minimize magnetic stray fields [159] (Figure 4.7b). The focusers are an simple an approach to design an anti-bend magnet based on a quadrupole [160]. The focusers, in the form of triangular cavities with a 20 mm base and 3 mm height, are oriented as shown in Figure 4.7a and filled with iron powder to enhance the magnetic field at the sweet spot. The arrangement of magnetic elements in each layer follows a cubic void alignment based on Equation 4.1 and is illustrated in Figure 4.7a.

A field strength of 0.5 and 0.7 T and a B_0 homogeneity of $\Delta B_0/B_0 = 10^{-4}$ over a cylindrical volume of 3 mm with diameter and length of 3 mm by 3 mm was developed and employed for NMR measurements.

To facilitate mechanical shimming, the completed magnet was enclosed with a 5 mm thick aluminum frame, allowing the mounting of a micrometer screw. The magnetic field strength at the nominal sweet spot within the magnet bore was fine-tuned by inserting an ultrafine polished ferromagnetic cylinder made of ferritic steel. This cylinder serves as a filler to normalize the stray magnetic field lines and reduce the magnetic field strength [161, 162].

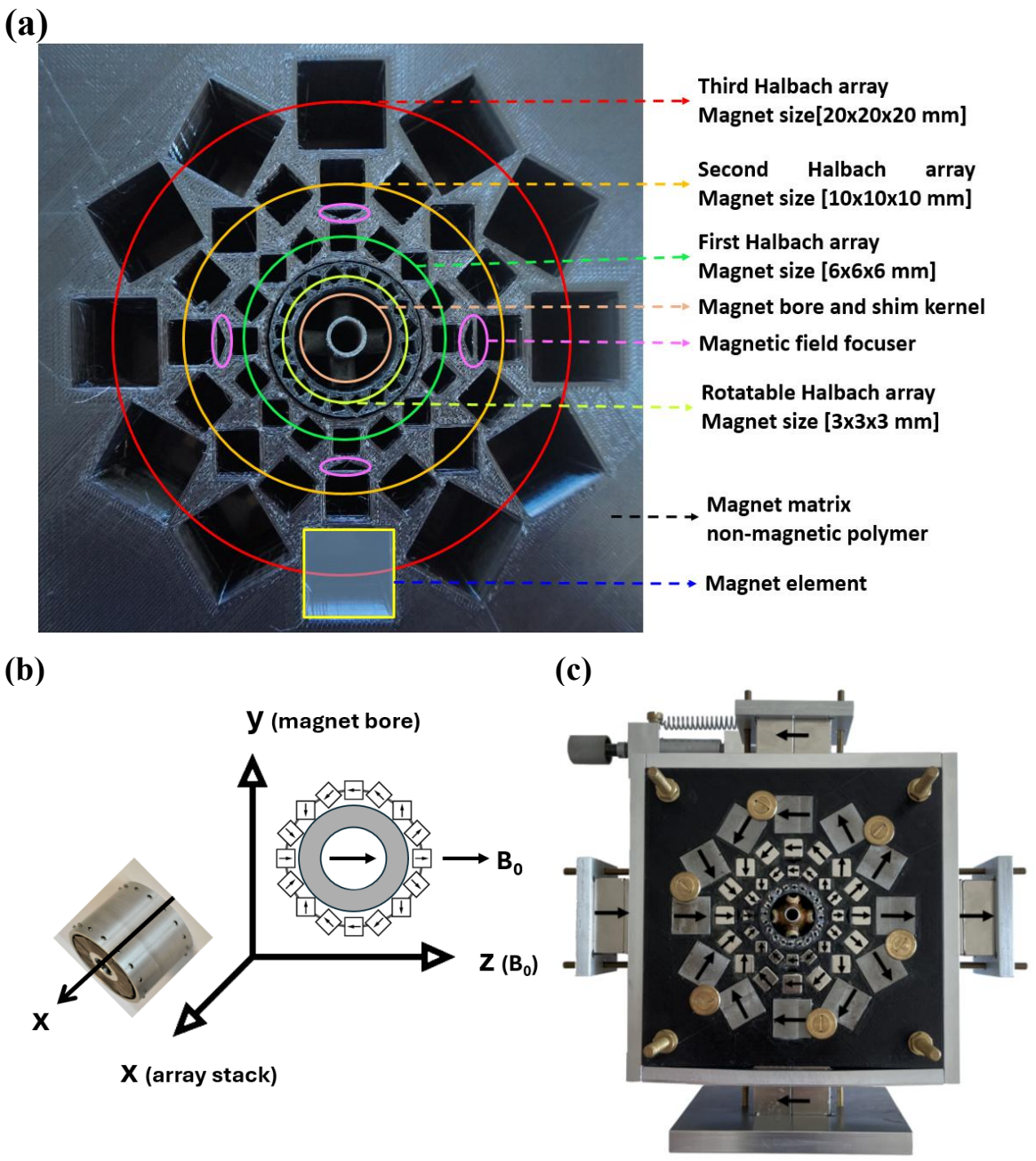

Figure 4.7: (a) The multilayer Halbach magnet designed using 3D CAD and finalized with a 3D printer. Three layers, rotatable components, magnetic focusers, and magnet elements are color-coded for clarity. **(b)** Schematic diagram illustrating the Halbach magnet with 3D Cartesian axes, showing the magnetic field (B_0) in the z-direction, the magnet bore in the z-y plane, and the Halbach array stack in the x-direction. **(c)** The fully assembled Halbach magnet includes the mechanical and electrical shimming components, along with the shimming kernel.

A 14-pin socket connection was specially designed to supply electrical power to the seven channels from the current source, as visually represented in Figures 4.8a and 4.8b. The current source was meticulously constructed using state-of-the-art electronic components and adhering to international standards prevalent in the field of electronic devices. Although we did not conduct measurements specifically to assess the ripple coefficient of the current source, it is worth noting that this parameter did not significantly impact our experiments. In our case, the shimming coil acts as a robust inductor, and any potential rippling from the current source was relatively minor in comparison. It's important to emphasize that NMR measurements were initiated only after achieving stable shimming conditions. Furthermore, a similar design concept is employed in room temperature shimming within Bruker NMR spectrometers, a well-established and respected practice in the field.

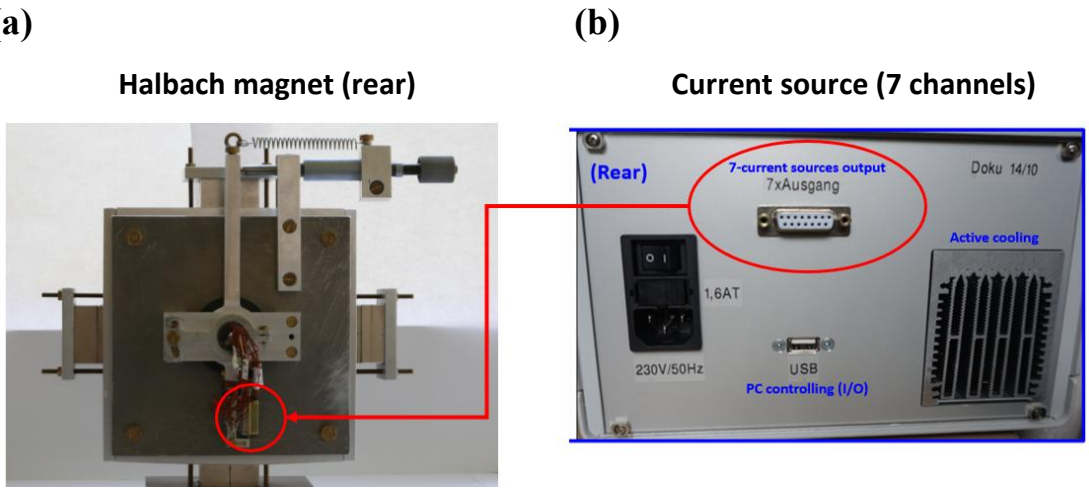

Figure 4.8: (a) The rear view of the finalized Multilayer Halbach magnet in Figure 4.3b, showing the mechanical shimming driving micrometer mechanism and the 14-pin socket connection to the **(b)** the home-built current source that offers ultra-precise electrical current for the 7 shimming axes within a step of 50 mA and current fluctuation of less than ±2 mA. Moreover, the current source can be operated locally by the front buttons and remotely via a USB connection.

4.1.4 Mapping the magnetic field (B_0)

The absolute B_0 field strength of the MLHM magnet, before equipping it with the shim system, was mapped by placing a directional magnetometer (gaussmeter) inside the magnet bore, aligned parallel to the $z-$ axis. Precise positioning of the magnetometer was achieved using a high-precision 3-axis stage micrometer (Thorlabs, Inc.). The B_0 mapping process encompassed the entire usable volume (D = 6 mm, L= 6 mm) (indicated by the red circles in Figure 4.9). Furthermore, B_0 mapping was performed at three specific slices located at -1.5 mm, 0 mm, and 1.5 mm within the confined volume later occupied by the solenoid coil

(marked by green circles). The mapping initiated from the nominal sweet spot of the magnet and systematically moved to cover 250 data points within the $z-y$ plane for each of the volume slices. These measurements were carried out by inserting a magnetometer attached to a 3-axis stage micrometer into the magnet bore. The absolute mapping, conducted prior to inserting the shim system, offers valuable insights into the overall field inhomogeneity of the magnet. This information is crucial for identifying a shim-usable volume, which corresponds to the range of electrical shimming capabilities. The distribution of magnetic field strengths, calculated from the measured data points, is represented in the density plot shown in Figure 4.9 (a-f). These plotted points cover the $z-y$ plane at $x = -1.5$ mm, 0 mm, and 1.5 mm.

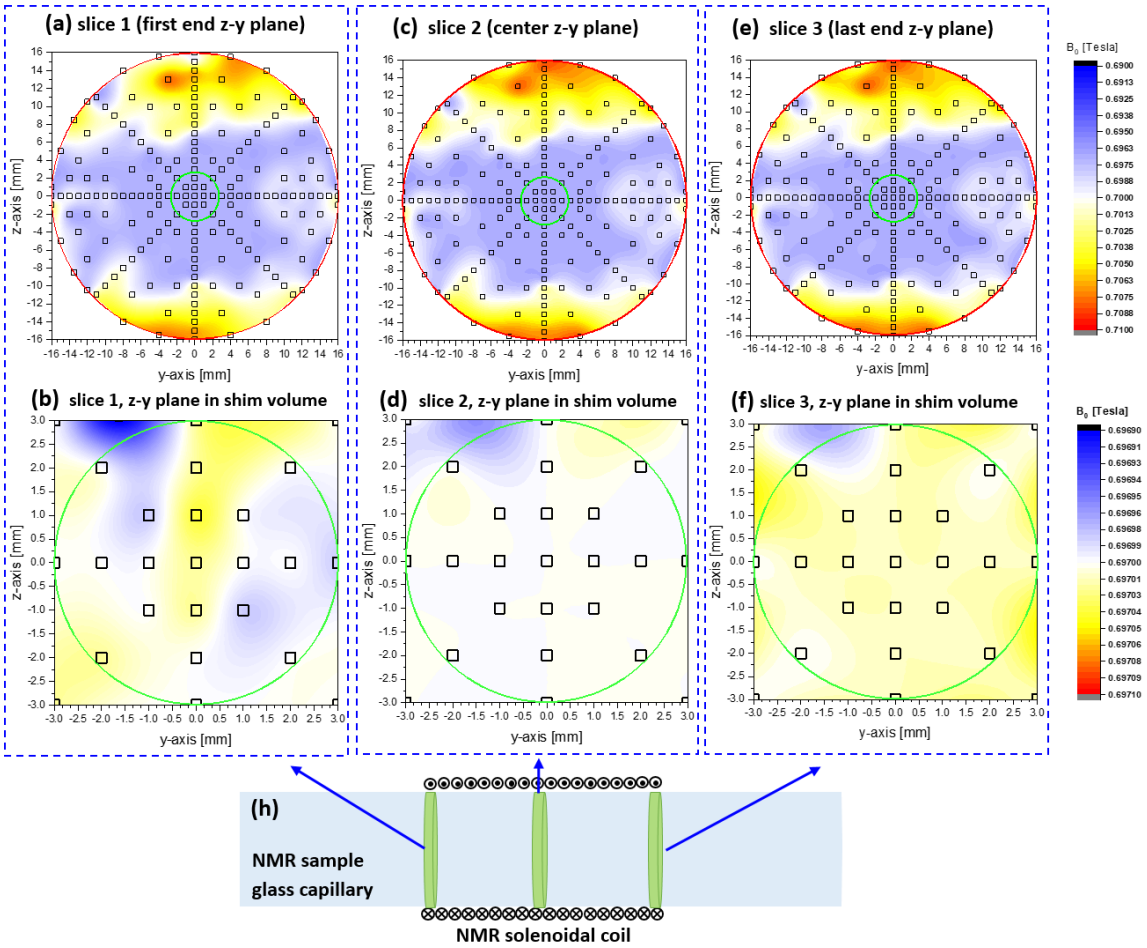

Figure 4.9: Absolute B_0 mapping was conducted within the 3.4 mm bore of the MLHM magnet without activating the shim system, with the green circle indicating the complete mapped volume. This process involved three discrete slices within the $z-y$ plane, corresponding to the two end slices and the central slice [**(a)**, **(c)**, and **(e)**, respectively]. The subsequent mapping encompassed the usable cylindrical cavity (D = 6 mm, L = 6 mm) after the shim system was introduced, with the green circles representing the shim-optimized volume [**(b)**, **(d)**, and **(f)**]. **(h)** Illustrates the glass capillary (ID = 2.4 mm, OD = 3 mm) containing the NMR sample, with the solenoidal NMR coil wound concentrically around it to maximize field homogeneity and sensitivity.

The shim process aimed at rectifying the magnetic field inhomogeneities within the available cylindrical cavity of the MLHM magnet (D = 6 mm, L = 6 mm, as denoted by the inner green circles in Figure 4.9) (refer to Section 4.1.5 and 4.1.6). The effective shim was applied to the volume fraction occupied by the sample within the solenoidal coil, which was approximately 3 mm in length and had a 3 mm inner diameter (ID). However, the entire cylindrical cavity (D = 6 mm, L = 6 mm) was shimmable. The probehead's positioning capabilities within the $y - z$ plane had a range of 1.2 mm, which proved entirely adequate for identifying the most homogeneous volume to encompass the sample, thereby achieving the narrowest line width and optimal signal shape.

4.1.5 Mechanical shim system

A rotatable homemade magnetic layer, configured in the Halbach form (Figure 4.10), was installed as the initial layer of the MLHM magnet (highlighted in yellowish-green and labeled in Figure 4.7a) to change the orientation of the magnetic field vector within the $z - y$ plane.

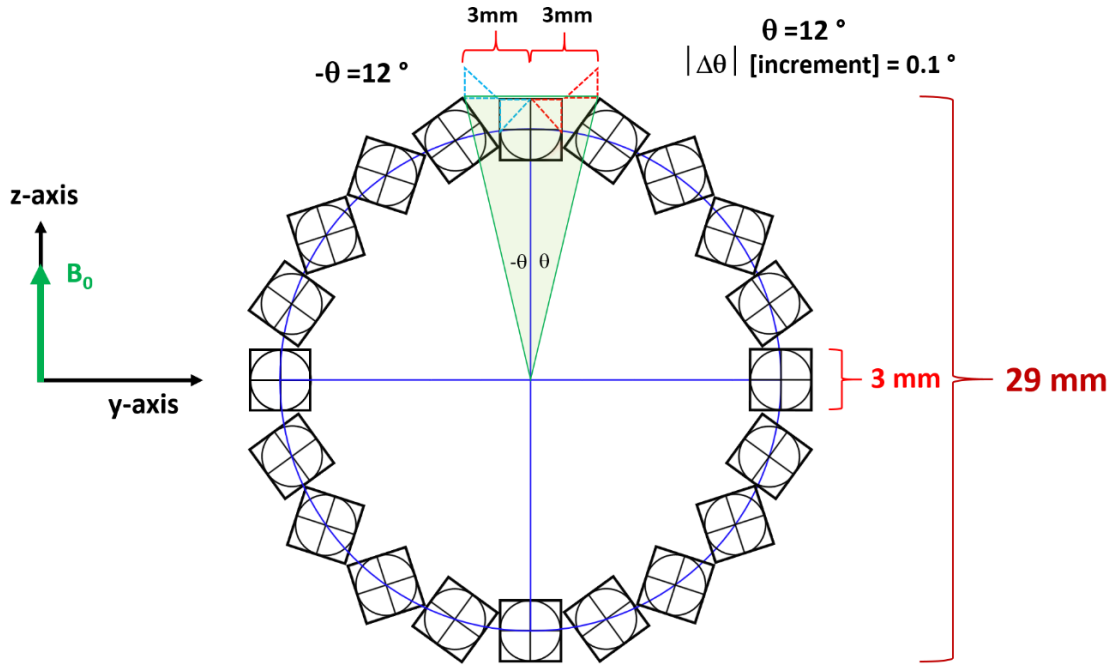

Figure 4.10: The rotatable Halbach layer served as an integrated mechanical shim system for adjusting $B_{z(z\text{-}y\ plane)}$ through a limited rotation within the z-y plane ranging from $-12°$ to $+12°$.

The rotatable shim layer is secured to a custom-made spring-loaded micrometer, enabling a reversible and precise rotational adjustment of 1⁄120 of the cubic element's dimension within the shim ring (3 mm). The mechanical shimming system contributes to the magnetic

components of $B_{z(mechanical)}$ and enhances the B_z-component of B_0. To achieve greater B_z homogeneity, fine shimming is necessary in X, Y, Z, ZX, ZY, XY and Z^2 channels. Therefore, we incorporated an electrical shim system to meet these requirements.

4.1.6 Electrical shim system

The wide-bore magnet was designed to accommodate the electrical shimming system, as shown in Figure 4.11. This 7-channel shim system includes a shim kernel in a Helmholtz configuration, which supports the standard gradient shim coil design.

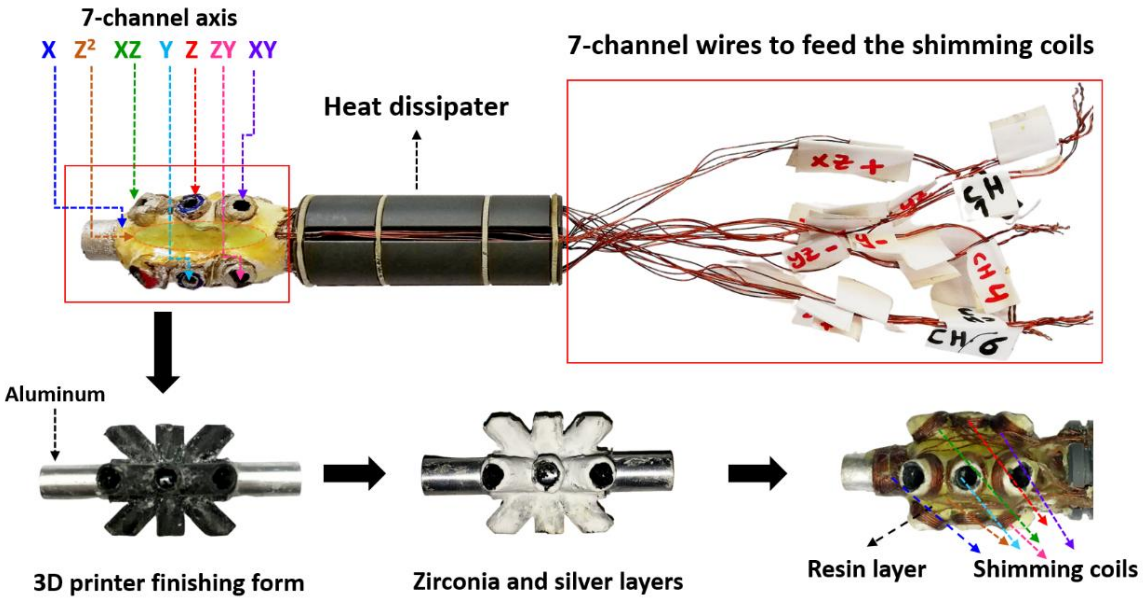

Figure 4.11: The shimming kernel featuring 7-Helmholtz axis coils, designed using 3D CAD and produced through 3D printing. Each axis's coils are divided into 4 parallel paths to minimize ohmic heating.

The electrical component of the shim kernel is connected to a programmable homebuilt digital 7-channel current source, capable of providing up to ± 2 A per channel with a resolution of 0.05 A. To fit within the narrow bore of the Halbach magnet used in this work. Instead, we replaced the typically used flexible printed circuit board (PCB, FR-4) with copper shim coils wound on hollow tubes, integrated as part of the shim kernel, as depicted in Figure 4.11. The design of the shim kernel was created using 3D CAD and was finalized by employing a 3D printer (Dremel DigiLab 3D45 3D Printer). In the original shim system, the addressed shim coils included only X, Y, Z, ZX, ZY, XY and Z^2 shim coils. This choice was made for i) These axes are the most influential in achieving a uniform magnetic field at the sweet spot. ii) The available space within the extremely small cavity needed to accommodate the sample, shim kernels, wires, and passive heat dissipation. iii) Higher-order harmonic shims would have required lithographic patterns on a PCB, which could not be mounted

within the shim kernel. Therefore, we selected the higher order of Z^2, which could be managed with 5 copper wires in an elliptical form connecting all channels, forming the second order as described in the literature [163]. For other channels, a reference was established with respect to the X shim coil axis. The X shim coil, mounted such that the magnetic field at the coil center forms a 90° angle with the z-axis, was subsequently designated as the Y shim coil, with the z-axis fixed in the direction of the Halbach magnet's B_0. The XZ shim coil is positioned that the magnetic field at the coil center forms a 45° angle with the Y-axis. Similarly, the coil where the magnetic field forms a 45° angle with the z-axis was labeled as the YZ shim coil [164, 165].

The copper shimming coils were coated with three layers. First, a layer of zirconia, an excellent electrical insulator with high thermal conductivity (thermal conductivity of 8.1 W/m K [166]) was applied to provide both electrical insulation and mechanical protection for the coils. Second, an epoxy layer was added on top of the zirconia due to its high heat conduction and low heat capacity. Finally, a silver-based resin was applied to enhance thermal conductivity, facilitating greater passive heat dissipation. These three layers were coated with thicknesses ranging from 200 to 500 µm to prevent thermal storage that could lead to temperature overshoot.

The generated magnetic fields of the 7-channels shimming kernel versus electrical currents at the nominal sweet spot using a magnetometer attached to a 3-axis stage micrometer at a fixed position are shown in Figure 4.12. The measurements were performed with the shimming kernel out of the magnet to avoid saturation of the magnetometer.

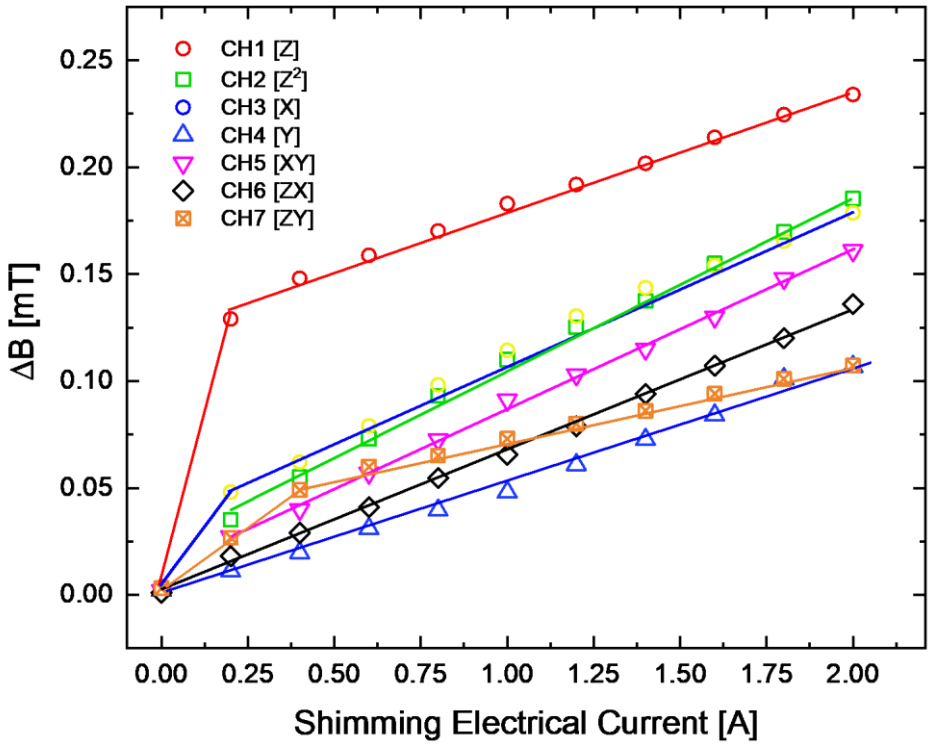

Figure 4.12: Induced magnetic fields of the 7-channels shim-kernel versus electrical currents at the nominal sample spot (rotary of the 7-axis).

Passive heat dissipation and transfer mechanisms were implemented using the shim kernel, which also serves as the core of the electrical shimming system. By extending the shim kernel body 3 cm beyond the magnet cavity, excess heat is effectively transferred out of the magnet. The shim kernel, being sufficiently large and constructed from thermoplastic material coated with zirconia—an excellent thermal conductor—facilitates efficient heat dissipation while maintaining its primary function in the shimming process. The shim kernel has a volume of approximately 55 cm^3, a mass of approximately 18 g, and an effective surface area, including internal components, of 105 cm^2.

To address the Joule heating generated by the shimming system while maintaining the same number of coil turns, particularly when operating the shimming current at maximum levels (±2 A per channel), each shimming coil was divided into four separate coils connected in parallel. This configuration reduces electrical resistance and minimizes heat generation. The four coils were wound on top of each other within a compact assembly, enabling the use of a shorter stage (approximately 5 mm) of the stages within the shimming kernel) for coil winding on the shimming channel. This design allows the magnetic fields from each coil to sum effectively, avoiding the need for a single coil carrying high electrical current, which would otherwise result in excessive heat and energy loss.

Consequently, the running electrical currents were reduced to a quarter of the main channel current, resulting in a fourfold reduction in dissipated heat ($E_{dis}=I^2$ R, where I= electrical current, and R= Ohmic resistance) at the sample spot. The measurement of Joule heating generated by the electrical shimming system was conducted using the setup configuration illustrated in Figure 4.13. Here, the shimming current source was connected to the modified 7-axis shimming coils within the shimming kernel, with the thermal coupling positioned at the sweet spot of the shimming kernel. The temperature measurement results showed a reduction in temperature from 96.2°C to 32.6°C at full operation currents (14 A for all channels) as illustrated.

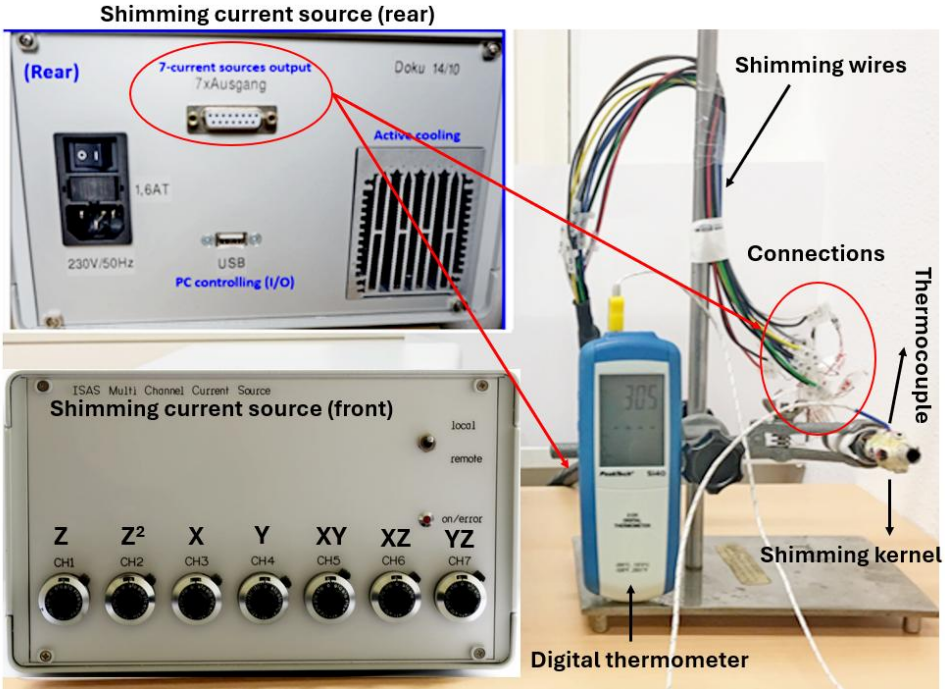

Figure 4.13: Measurement of Joule heating generated by the electrical shimming system during the operation of all shimming axes, with a maximum electrical current (±2 A for each channel). The diagram illustrates the setup of the shimming current source connected to the 7-axis shimming coils, with the thermal coupling located at the optimal position within the shimming kernel.

In conclusion, by implementing the two modifications, the electrical shim system was able to operate at typical shim currents of around 0.1 A per channel without causing a significant increase in sample temperature (approximately 0.1°C), as illustrated in Figure 4.14 (blue data points). While operating the 7-axes shimming coils at maximum current is rare, testing under extreme conditions involve operating all shim channels at half of the maximum and full maximum currents (1 A and 2 A, respectively) for validation purposes. Under these conditions, the shim-kernel system exhibited stability, with temperature increases above

room temperature measured at 0.3°C, 3.0°C, and 5.0°C for currents of 0.1 A, 1 A, and 2 A, respectively.

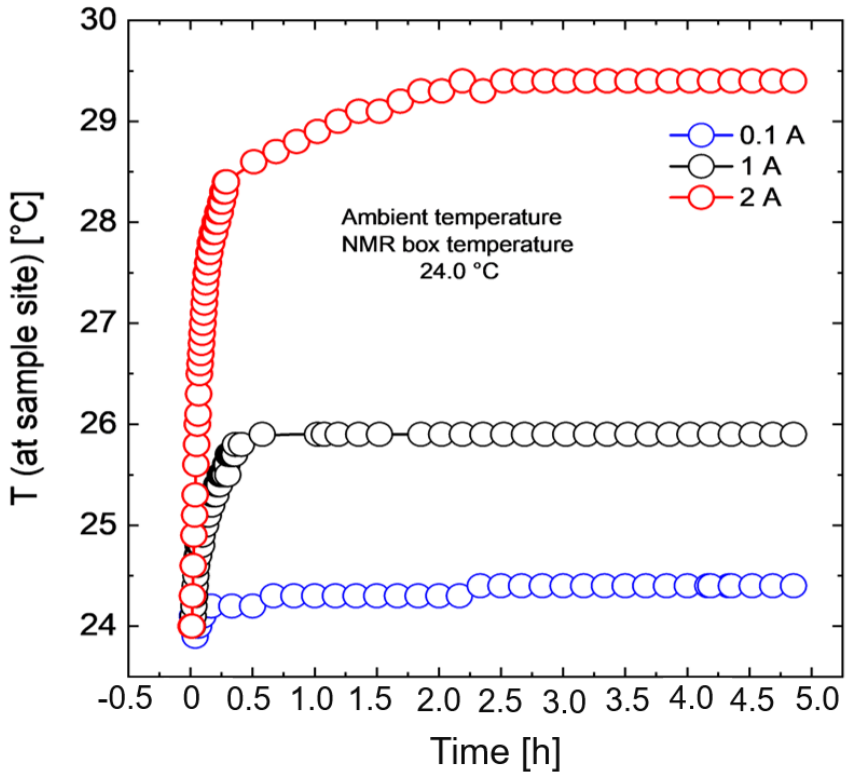

Figure 4.14: Temperature changes at the sample site during operation of the electrical shim system at currents of 0.1 A, 1.0 A, and 2.0 A per shim channel, illustrating the effectiveness of heat dissipation from the sample site.

4.2 Low-field NMR spectrometer

4.2.1 Planar NMR probehead

The NMR probe (Figure 4.15a) was constructed on a printed circuit board made of glass-reinforced epoxy laminate (RT4) with a double copper layer, each with a thickness of 35 µm [167]. The layout of the resonance circuit and the RF BNC copper tracks were created on the NMR probehead board using UV lithography. The NMR resonator is a solenoidal coil with a copper wire diameter (D) of 200 µm, consisting of 11 turns wound around a high-resolution NMR glass tube with an outer diameter (OD) of 3 mm and an inner diameter (ID) of 2.4 mm. The solenoidal coil accounts for a major part of the inductance (approximately 0.70 µH), while the onboard copper track connectors contribute about 0.15 µH to the resonance circuit (Figure 4.15b). Bonding wires and connection points introduce impedance discontinuities, leading to increased transmission loss and signal reflection [168], particularly as resonance frequency increases [169], even at low-field NMR. Therefore, the NMR probe was designed as a

solenoidal mini coil integrated into a planar design to enhance sensitivity, minimize B_1 inhomogeneity, and reduce the impact of bonding wires and connection points on impedance discontinuity and signal transmission loss. Nonmagnetic trim multi-turn and ceramic chip capacitors (Voltronics Corp., Salisbury, MD, USA) were used to tune and match the resonance circuit to 29.93 MHz.

The nutation spectrum (Figure 4.15c) obtained for the solenoid mini-coil mounted in the probe-head highlights the uniformity and intensity of the RF field generated by the system. The probe-head demonstrated a hard pulse length of approximately 1.6 µs at a power level of 2 W, indicating efficient RF energy delivery. This performance aligns with the design objectives for high-resolution NMR applications, ensuring precise excitation of nuclear spins. Sample temperature was monitored using a Pt100 sensor positioned near the sample to maintain stable operating conditions. The calibration of the temperature response for the electrical circuit components of the NMR probe-head, including the matching and tuning capacitors, is illustrated in Figure 4.15b.

The sensitivity of the homebuilt planar NMR probe in the NMR experiment at a magnetic field strength of 0.703 T (29.93 MHz for ^{1}H) is determined using the signal-to-noise ratio (SNR), typically defined as the ratio of the height of a resonance of interest to the root-mean-square of the noise level.

In this study, the SNR of the anomeric proton of sucrose was measured to quantify the sensitivity of the planar NMR probe, following a typical protocol in the literature [170].

The sucrose sample had a volume of approximately 35 µL at a concentration of 21.8 mM in D_2O, but the SNR is directly proportional to the volume fraction occupied by the sample within the coil, making the effective sample volume around 14 µL. With an experiment time of 8 accumulation scans, each taking 1.9 seconds per scan, and an SNR of 116, the limit of detection ($n\mathrm{LOD}_m$) is calculated using the formula $n\mathrm{LOD}_m = 79\ nmol\ s^{1/2}$ at 29.93 MHz, calculated from the formula $n\mathrm{LOD}_m = 3n\sqrt{t_{exp}}/\mathrm{SNR}$ where n [mol] refers to the portion of the sample within the 14 µL detection volume, and t_{exp} is the total experiment time (accumulated over 8 scans). To compare this measurement to one conducted at an NMR frequency of 600.13 MHz, the result was normalized by multiplying it by a factor of 189, following the scaling relationship $[\omega_L]^{7/4}$ [171, 172]. LOD falls within the range of 15-30 mg/L.

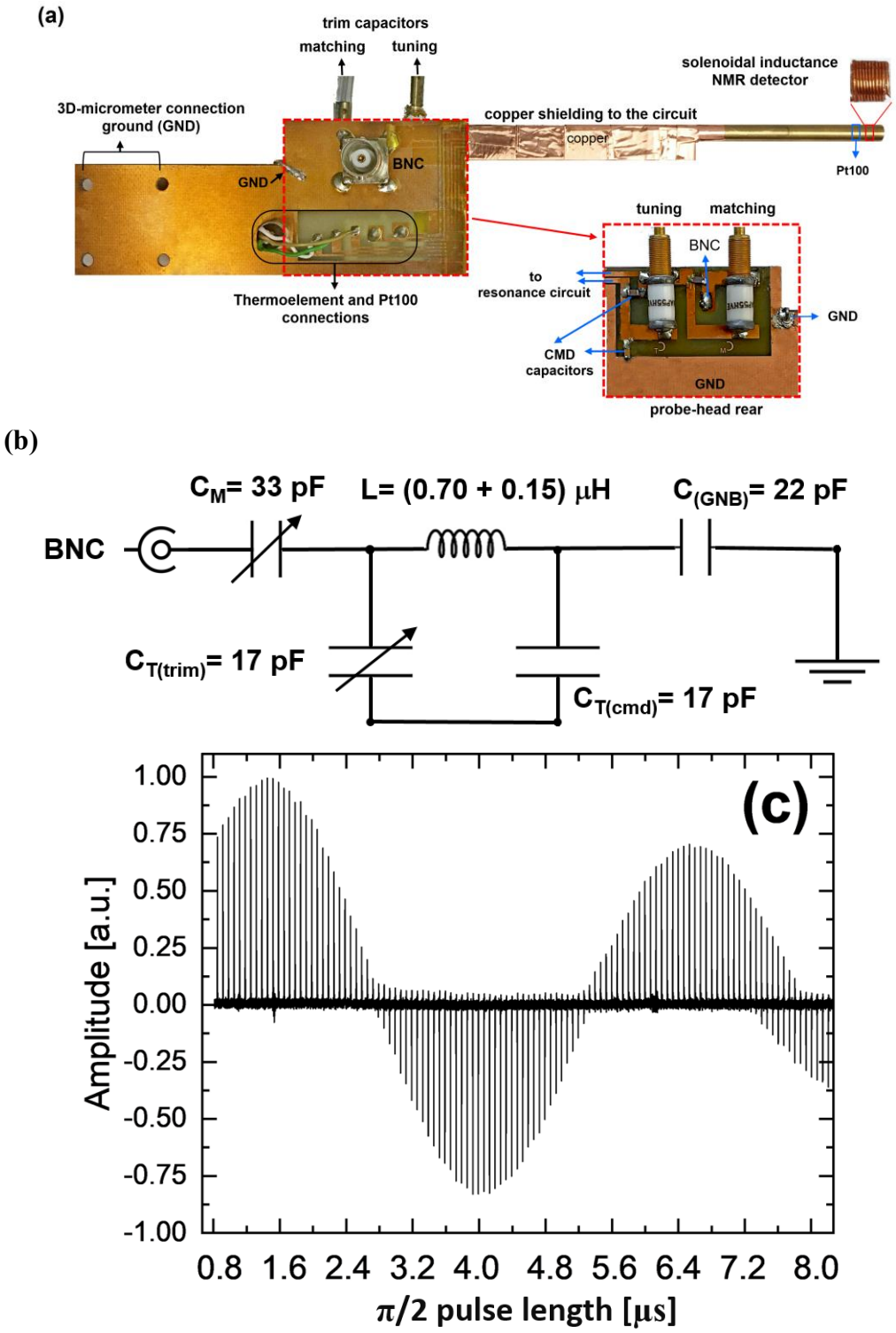

Figure 4.15: (a) Solenoidal-based NMR resonator (probehead) including thermal elements, a BNC RF connector, and electrical connections. **(b)** The electrical circuit of the NMR probehead tuned and matched at 29.93 MHz, showing the tuning and matching capacitors and the ohmic resistance of the circuit. The coil consists of 11 turns, with a 3.4 mm OD, 3 mm ID, and an inductance of approximately 0.70 µH, using a copper wire with a diameter (D) of 0.2 mm. The inductance of the onboard copper strip line connectors is approximately 0.15 µH. **(c)** The nutation curve obtained with the probehead in (a).

4.2.2 The radiofrequency shielded and thermally isolated NMR box

An aluminum box with a thickness of 2 mm served as RF shielding, and it was thermally insulated and controlled using a polyurethane foam jacket (Figure 4.16a), as per the methodology outlined in the literature [63]. The temperature control system for both the magnet and the NMR probe was housed in a homebuilt RF shielded box made of 2 mm thick aluminum (Figure 4.16b). This box was thermally insulated with a formfitting polyurethane foam jacket and equipped with a heating system. Temperature regulation was achieved through a standalone programmable commercial temperature controller. Passive vibration isolation measures were implemented to suppress mechanical vibrations.

A high-precision 3-axis stage micrometer was utilized to locate the magnet's sweet spot. Additionally, a high-precision rotation stage, adjustable in 1° increments (Thorlabs Inc.), was employed to rotate the entire magnet relative to the probe-head, enhancing the alignment perfectly between the magnet (B_0) and the probehead to ensure ($B_0 \perp B_1$).

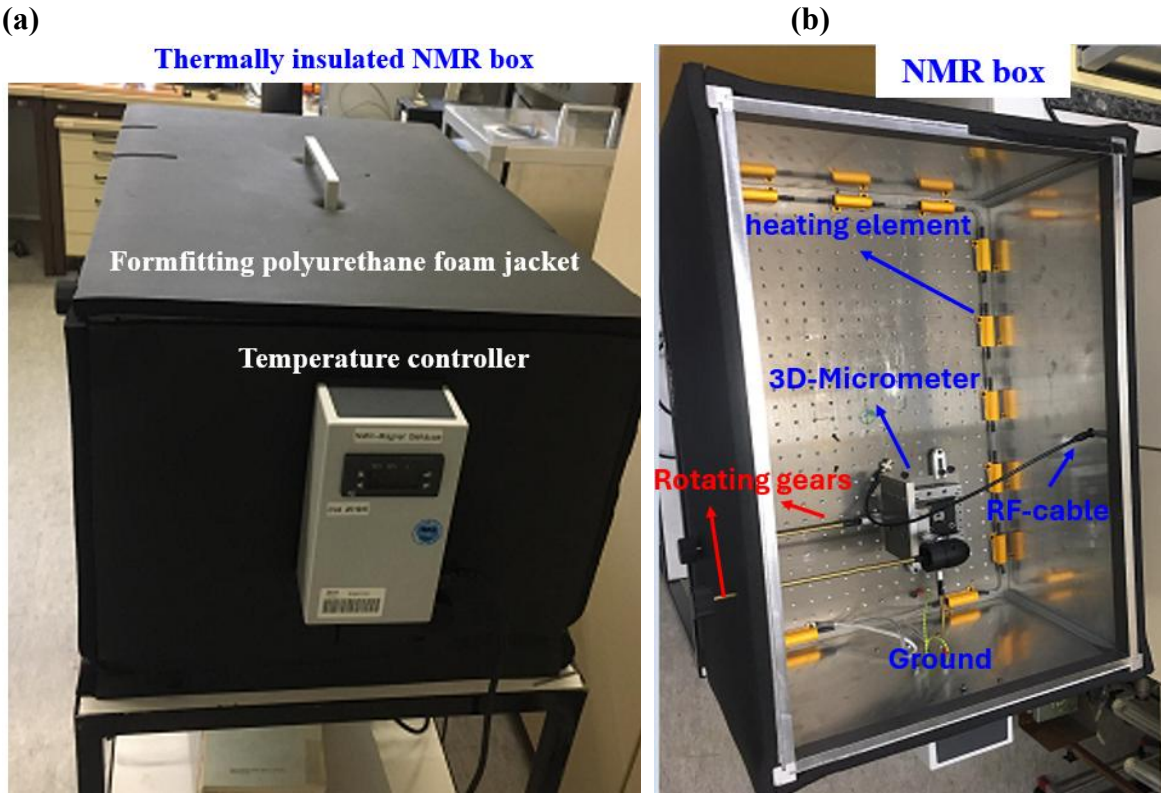

Figure 4.16: (a) The radiofrequency shielded and thermally isolated NMR box, showing the heating elements, electrical connections and the 3D positioning micrometer and the rotational micrometer. **(b)** The side view of the NMR box showing the temperature controlling unit and the formfitting polyurethane foam jacket and equipped with a heating system.

4.2.3 Assembling and operation

The homebuilt LF-NMR spectrometer (Figure 4.17) was assembled using an MLHB magnet operating at 29.93 MHz. Instrument control employed the Pulse Blaster interpreter (SpinCore Technologies, Inc., Gainesville, FL, USA), and amplitude-modulated pulses were generated via a Radio Processor board (SpinCore Technologies, Inc., Gainesville, FL, USA).

The magnetic field strength of the MLHB magnet can be adjusted within the range of 0.5-0.77 T based on the thickness of the ferromagnetic cylindrical filler in the magnet's cavity (as explained in section 4.1). Consequently, the spectrometer can operate at frequencies ranging from 21.25 MHz to 32.78 MHz for protons, requiring appropriate tuning and matching of the NMR probehead.

The magnet used in this study is described in Section 4.1.3. The fabricated NMR probehead was mounted on a high-precision 3-axis micrometer stage to precisely locate the sweet spot of the magnet. Additionally, a high-precision rotation stage, adjustable in 1° increments (Thorlabs Inc.), was employed to rotate the entire magnet relative to the probe-head, enhancing the alignment between the magnet and the probehead. This alignment improvement contributed experimentally to achieving a narrower linewidth.

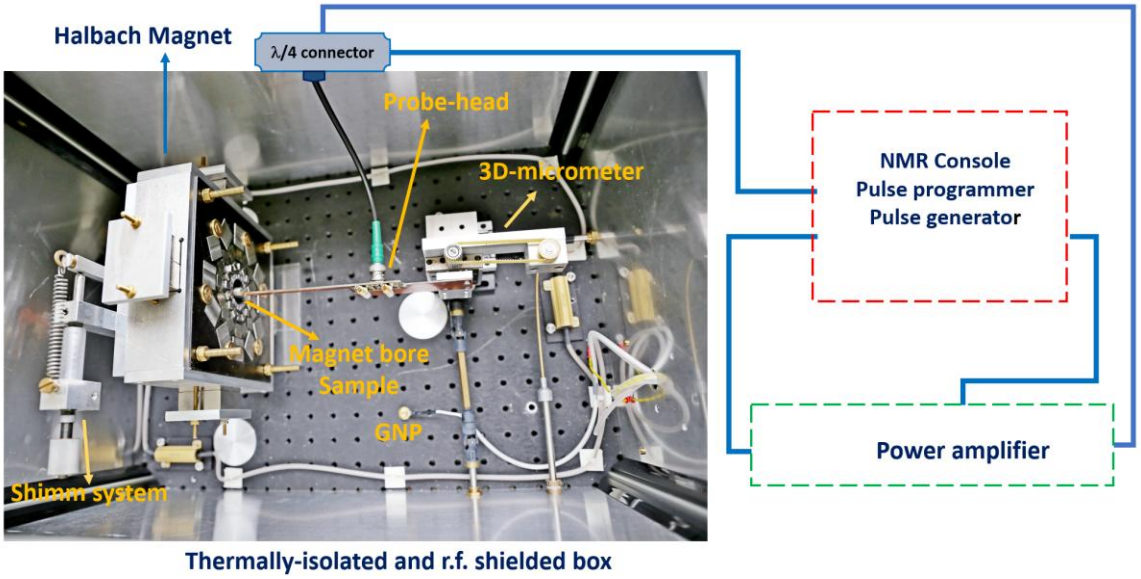

Figure 4.17: The homebuilt LF-NMR system equipped with an MLHB magnet, labeled with its components: NMR probe-head, ground coupling (GND), multilayer Halbach magnet (MLHB), mechanical shim system, 3D-stage micrometer, thermally isolated and RF-shielded box, NMR console (pulse programmer and pulse generator), and power amplifier.

For the operation of the low-field NMR spectrometer and to validate the mechanical and electrical shimming, we conducted several NMR measurements using a water sample. These measurements were acquired on the same water sample by changing the sample position

until optimizing the signal. Subsequently, the mechanical shimming was performed by rotating the mechanical shimming ring within ±15°, as mentioned in section 4.x, until the signal was optimized and ready for fine shimming using the electrical shimming within the available 7 shimming axes (Z^2, Z, X, Y, ZX, ZY, XY).

Low-field ^{1}H-NMR spectra were acquired using the iSpin-NMR 2U portable console from SpinCore Technologies Inc. The data were processed and analyzed using ACD/Labs Software V.11. Additionally, for several measurements, the low-field spectrometer was connected to the Bruker console.

The water signals were acquired using the onboard NMR probe within a 3.0 mm outer diameter (OD) and 2.4 mm inner diameter (ID) NMR glass tube, with a length of 3 mm, as shown in Figure 4.18. The spectrum shown in black represents data obtained without any shimming system, resulting in a linewidth of 15.3 Hz and a non-pure Lorentzian line shape due to B_0 magnetic field inhomogeneity. In contrast, the spectrum shown in blue, acquired with mechanical shimming alone (without electrical shimming), demonstrates a noticeable improvement, with a reduced linewidth of approximately 11.6 Hz and a mostly Lorentzian shape. The spectrum shown in red, obtained with both mechanical and electrical shimming, exhibits further enhancement, with a linewidth reduction to 4.5 Hz and a purely Lorentzian signal shape, indicating significantly improved B_0 magnetic field homogeneity.

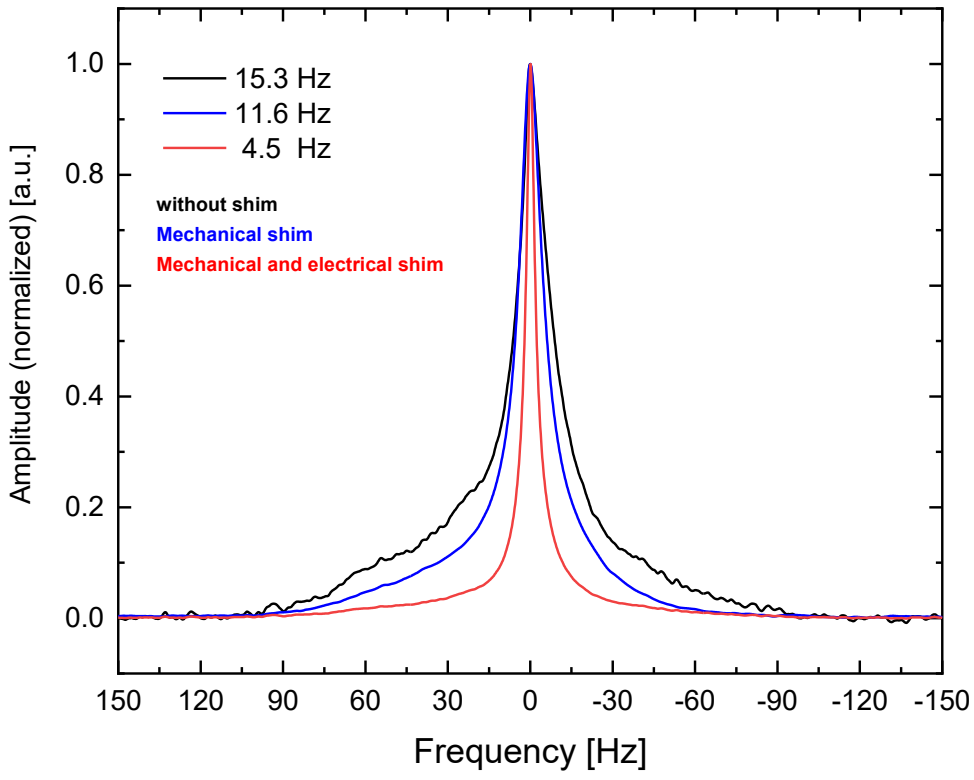

Figure 4.18: Water signals acquired without a shimming system (black), with mechanical shimming (blue), and with combined mechanical and electrical shimming (red).

Optimization of the NMR signal amplitude was conducted in response to changes in the power of 90° pulses (with a fixed pulse duration separately optimized at 1.6 ms) and the central resonance frequency (O1) of B_0. The analysis aimed to determine parameters for effective and optimized NMR measurements, revealing that a power range of 1.9-2.5 W and a central resonance frequency within ±5 Hz yielded optimal results. This approach resulted in only a 7% decrease in amplitude, even at off-resonance frequencies within this specified range. The results are visualized in a 3D plot in Figure 4.19.

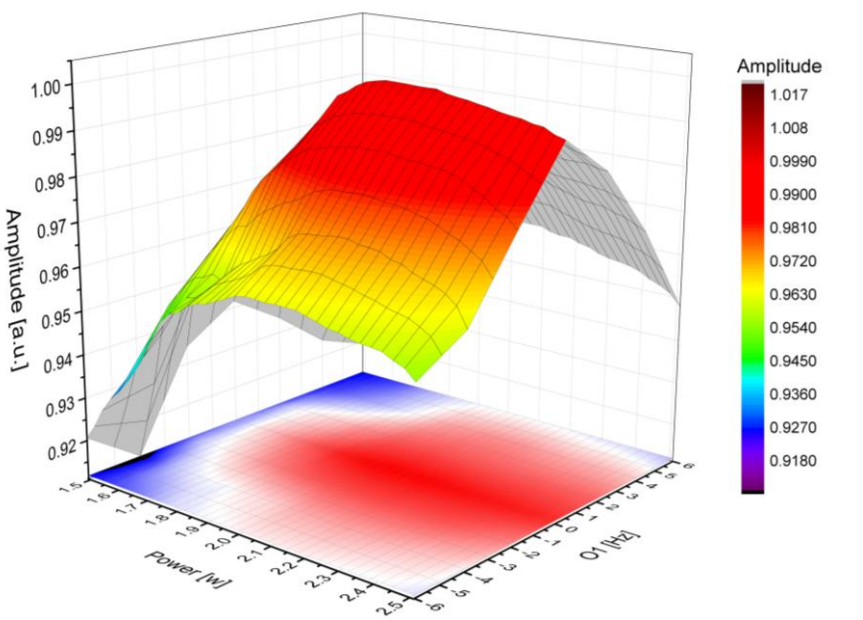

Figure 4.19: A 3D plot illustrating the experimentally obtained variations in NMR signal amplitude as a function of B_1 power (power of the 90° hard pulse) and central resonance frequency (O1) of B_0.

5 Optimal Control in NMR Spectroscopy: Applications and Evaluations

In this work, spin system editing is achieved using the Krotov algorithm from optimal control theory, which is applied to enhance the selectivity and efficiency of pulses in low-field NMR experiments. The algorithm employs a gradient-based approach to improve the objective function monotonically at each iteration [54] and incorporates second-order derivatives to accelerate convergence, particularly near the optimal solution [63, 173].

The performance of the Krotov algorithm is demonstrated on four distinct systems: neat acetic acid, cyclopentenone, and two metabolite pairs.

- Acetic acid and cyclopentenone: These systems are employed to demonstrate spectral editing in which specific NMR lines within the spectra of these molecules are selectively excited or eliminated. Acetic acid, devoid of spin coupling, offers a straightforward system for testing the fundamental effectiveness of the Krotov algorithm. Conversely, cyclopentenone, which exhibits more complex spin couplings, presents a greater challenge, providing a rich environment for editing spectra with multiple spin interactions. By comparing these two molecules, we assess the algorithm's performance in both simple and complex systems, highlighting its ability to manipulate spectral lines in the presence and absence of spin coupling.

- Metabolite systems: These systems are used to demonstrate the excitation or elimination of full molecular NMR lines. The first pair, a benzoic acid (BA) and alanine (Ala) mixture, and the second pair, phenylalanine (Phe) and taurine (Tau), involve more intricate spin interactions. In these systems, the focus shifts from editing individual spin transitions to selectively targeting and modifying the entire molecular spectral lines, which is essential for accurate metabolic analysis. These metabolite pairs provide an opportunity to test the Krotov algorithm in more challenging scenarios, where overlapping signals demand highly selective pulse control.

5.1 Selective excitation pulse for non-coupled system

Neat acetic acid, exhibiting a distinct 9.8 ppm difference between the hydroxyl and methyl proton signals, provides an ideal system for assessing the Krotov algorithm’s performance in spectral editing. In acetic acid, the methyl group consists of three equivalent spins, all of which resonate at the same NMR frequency. Therefore, they can be treated as a single spin. This approach reduces the complexity of calculations, promoting faster convergence. But in this simple example of acetic acid, we treat all the three methyl spins separately to obtain the NMR signal intensity of lines corresponds to the number of protons.

The Hamiltonian for neat acetic acid is as follows:

$$H_1 = 2\pi(\nu_1^a A_z + \nu_1^b B_z + \nu_1^c C_z + \nu_2^d D_z), \quad (5.1)$$

where *a, b* and *c* represent the spins of the methyl group, while d represents the spin of the hydroxyl group of acetic acid. The spin matrices are denoted as A_i to D_i with i corresponding to the x, y and z. The resonance frequencies for methyl group are $\nu_1^a = \nu_1^b = \nu_1^c = -140.8$ Hz, and for hydroxyl group it is $\nu_2^d = 140.2$ Hz.

The calculations were conducted to determine optimal RF pulses for specific quantum state-to-state transfers within the spin system. These transfers involve the evolution of the spin system from an initial operator to a defined terminal operator, as described below:

Spin group 1 (Methyl group excitation):

Initial operator 1: $I_{ini}^{(1)} = A_z + B_z + C_z.$ (5.2)

Initial operator 2: $I_{ini}^{(2)} = D_z.$ (5.3)

Terminal operator 1: $TO_1 = A_x + B_x + C_x.$ (5.4)

Terminal operator 2: $TO_2 = D_z.$ (5.5)

Spin group 2 (Hydroxyl group)

Initial operator 1: $I_{ini}^{(1)} = A_z + B_z + C_z.$ (5.6)

Initial operator 2: $I_{ini}^{(2)} = D_z.$ (5.7)

Terminal operator 1: $TO_1 = A_z + B_z + C_z.$ (5.8)

Terminal operator 2: $TO_2 = D_x.$ (5.9)

The fidelity of the calculation (U_1 and U_2 represent the calculated pulse propagators for spin systems 1 and 2, respectively) is determined by:

$$\textit{fidelity} = \text{real}(\text{Trace}(TO_1' U_1 I_{ini}^{(1)} U_1')) + \text{real}(\text{Trace}(TO_2' U_2 I_{ini}^{(2)} U_2')). \quad (5.10)$$

The pulses were designed using a Krotov-based algorithm, as described in [53, 54], and implemented in MATLAB using code adapted from Maximov et al. [53], which is based on the formulation of Tannor et al. [174]. The optimal control pulses had a duration of 50 ms, with convergence typically achieved after 1000 iterations of the algorithm. The computation time was in the order of several minutes when executed on an Intel Core i7 system with 8 GB of RAM. Experimental ^{1}H-NMR spectra were acquired using hard pulses and selective excitation pulses, with LF-NMR measurements conducted at a magnetic field strength of approximately 0.7 T.

The corresponding simulated and experimental spectra are shown in Figure 5.1(a1, a2, and a3) and Figure 5.1(b1, b2, b3), respectively. The simulation (Figure 5.1a3) reveals some crosstalk from the COOH proton, along with a slight phase error in the methyl signal. The NMR signal of the hydroxyl group in acetic acid shifts toward the average chemical shift between the hydroxyl group in neat acetic acid (11.8 ppm) and the water signal (4.75 ppm), considering the relative proton concentrations [175]. Experimentally, the signals appear at 2.05 ppm (methyl) and 11.67 ppm (hydroxyl), separated by approximately 9.62 ppm (about 285 Hz at an NMR frequency of 29.93 MHz) (Figure 5.1b1). Gaussian selective excitation is effective for spectral editing of acetic acid, as the methyl and hydroxyl signals are well-separated. However, the application of OC pulses on acetic acid signals in this study demonstrates efficient excitation and suppression of both the desired and unwanted signals, without interference, in low-field NMR, even though Gaussian selective excitation alone could be sufficient.

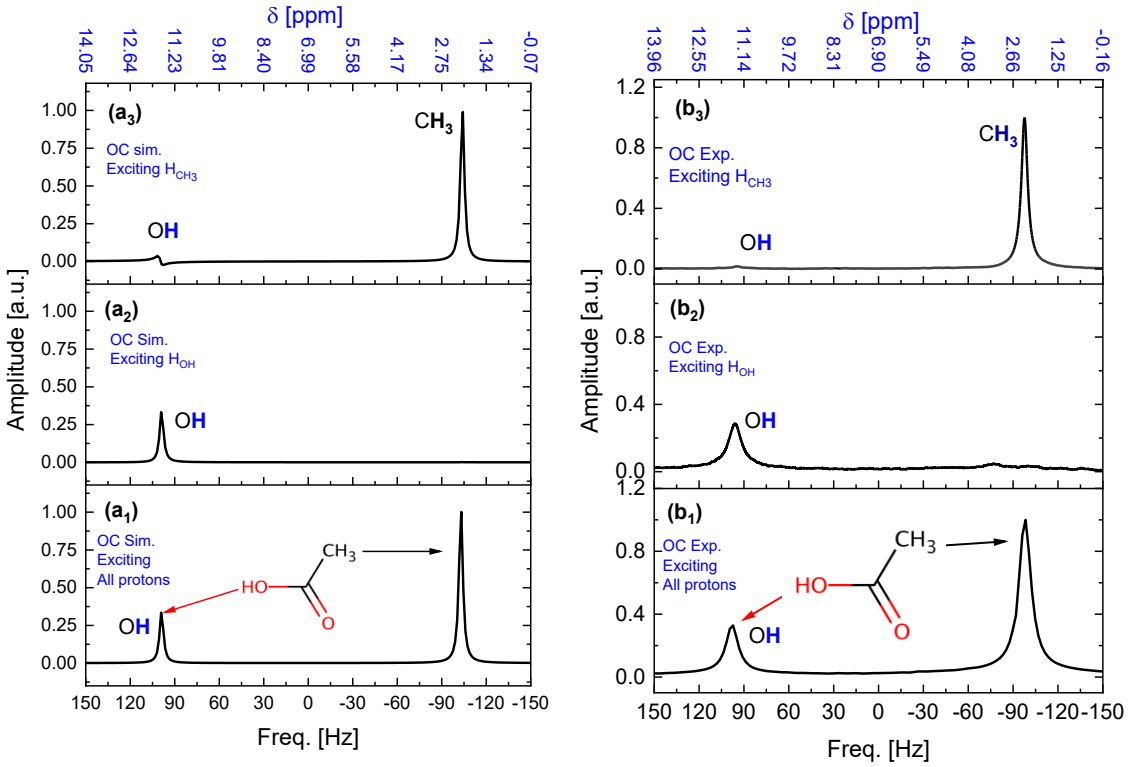

Figure 5.1: Simulated and experimental ^{1}H-NMR spectra at 29.93 MHz of neat acetic acid using optimal control (OC) pulses to excite (**a**$_1$ and **b**$_1$) all protons, (**a**$_2$ and **b**$_2$) hydroxyl protons, and (**a**$_3$ and **b**$_3$) methyl protons. The OC pulses were calculated using amplitude and phase modulation based on the Krotov algorithm.

The applied Gaussian pulse had a 1% cutoff, was offset to the targeted signal, had a maximum power level of 4.25 µW, and a pulse length of 20.4 ms. Excitation and suppression factors (EF and SF) for both Krotov and Gaussian pulses were calculated based on the absolute

integration of hydroxyl and methyl proton signals relative to the absolute integration obtained after applying hard pulses, as shown in Table 5.1.

Table 5.1: EF and SF factors for signal groups excited with Gaussian and OC (Krotov) pulses. EF and SF factors are calculated based on the absolute integration of the desired and undesired signals, respectively, in comparison to the absolute integration of these signals after excitation with a hard pulse.

Factor	**Hydroxyl proton OH group**		**Methyl protons CH_3 group**	
	Krotov	Gaussian	Krotov	Gaussian
EF	0.80	0.62	0.82	0.64
SF	0.04	0.03	0.06	0.05

The Gaussian pulse suppressed the unwanted signal with an SF of 0.03, like the Krotov selective pulse (SF = 0.04). However, the EF values for the desired signals using a Gaussian pulse (averaging 0.63) differ significantly from those achieved with OC pulses (averaging 0.81). Moreover, Gaussian pulses can only be applied over a continuous range of frequencies, while Krotov selective pulses can target any signal [63]. Notably, the EF is less than 1 because OC pulses operate at much lower power (0.08-0.1 W) compared to hard pulses (1.9-2.2 W). This study demonstrates the feasibility of applying optimal control pulses for subspectral editing at a field strength as low as 0.7 T, enabling selective excitation pulses to target individual components in multicomponent mixtures within the context of low-field NMR (LF-NMR).

5.2 Selective excitation pulse for coupled system

The proton NMR hard pulse spectrum of neat cyclopentenone taken at 600.13 MHz is shown in Figure 5.2b. In the high-resolution NMR spectrum at 600.13 MHz, the multiplets are well resolved, see Figure 5.2a. The same sample was measured with the home-built low-field NMR at 21.25 MHz (Figure 5.2c). The signals at -1464.85 Hz and -1232.25 Hz at 600.13 MHz appear as one signal at 21.25 MHz due to the low resolution. The linewidth of the low-frequency NMR signal is approximately 16 Hz.

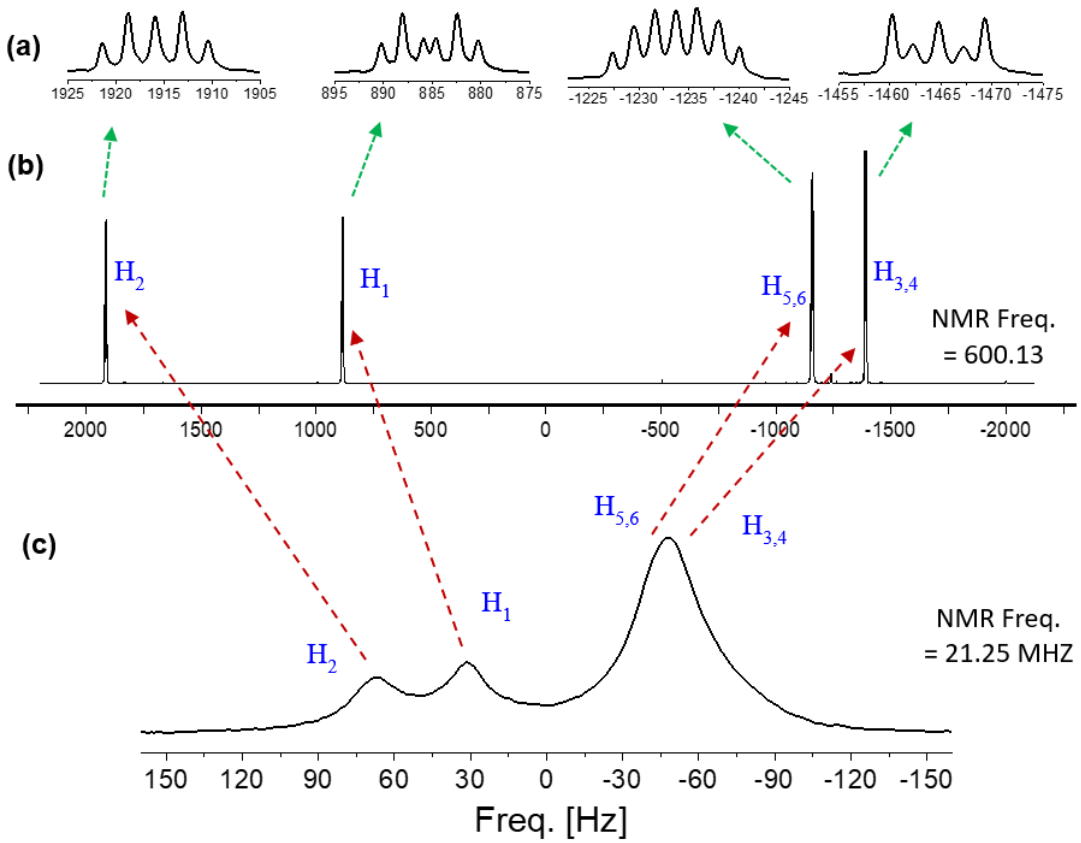

Figure 5.2: (a) Signal expansions of the NMR hard pulse spectra of cyclopentenone at 600.13 MHz **(b)** The full spectrum at 600.13 MHz **(c)** Spectrum at 21.25 MHz measured using the home-built portable NMR spectrometer.

The frequency at which the NMR line appears, along with the coupling constants for both NMR frequencies, was experimentally determined from the high-resolution NMR spectrum (Figure 5.2a) of cyclopentenone, as shown in Figure 5.3, where the protons and couplings are annotated. The frequency of the NMR line at 21.25 MHz was also obtained from the experimental spectrum and validated by comparing it with the resonance frequency derived by downscaling from 600.13 MHz to 21.25 MHz. All these frequencies and coupling constants are listed in Table 5.2.

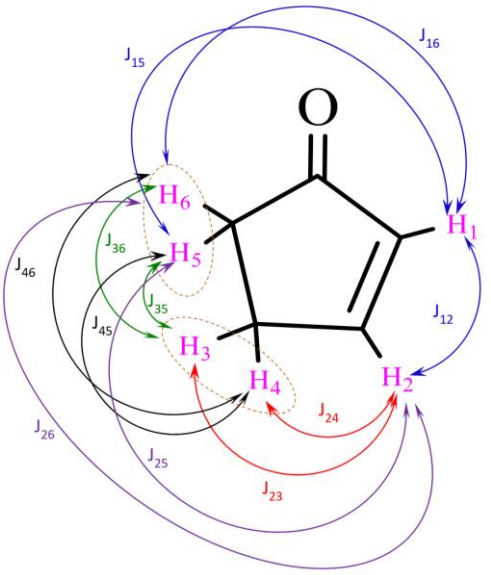

Figure 5.3: Visualization of the signal assignments and the coupling network of cyclopentenone. Numerical values are given in Table 5.2.

Table 5.2: Numerical values of the resonance frequencies and J-coupling of the coupling network of cyclopentenone shown in Figure 5.3.

J coupling [Hz]	**Resonance frequencies [Hz]**	
	600.13 MHz	21.25 MHz
$J_{12} = 5.65$ $J_{15} = J_{16} = 2.20$ $J_{23} = J_{24} = 2.60$ $J_{25} = J_{26} = 2.30$ $J_{35} = J_{36} = 2.68$ $J_{45} = J_{46} = 4.54$	$\nu_1 = 885.26$ $\nu_2 = 1915.89$ $\nu_3 = \nu_4 = -1464.85$ $\nu_5 = \nu_6 = -1232.25$	$\nu_1 = 31.34$ $\nu_2 = 67.83$ $\nu_3 = \nu_4 = -51.86$ $\nu_5 = \nu_6 = -43.63$

The hard pulse spectrum of cyclopentenone is shown in Figure 5.4a, with the frequency scale set to 0 Hz in the center of the spectrum. Every stack plot of an optimal control pulse spectrum consists of two NMR spectra; the upper spectrum is the simulated one while the lower spectrum is the experimental one. The experimental spin-spin relaxation time (T_2) values for cyclopentenone (650 ms and 430 ms at 600.13 MHz and 21.25 MHz, resp.) have been used in the simulations.

Four optimal control pulses were generated by employing the Krotov algorithm at 21.25 MHz to excite protons in the cyclopentenone sequentially during a series of experiments as indicated in Figure 5.4 (b-e).

The optimal control pulse for the excitation of the coupled selected protons were calculated in a non-robust way (SFI=RFI=0) with two control amplitudes corresponding to both phase and amplitude modulation.

The system Hamiltonian of the cyclopentenone spin system is:

$$H_{cyc} = 2\pi \sum_{i=1}^{6} \nu_i^{cyc}\ I_{zH_i}^{cyc} + 2\pi \sum_{i=1}^{6} \sum_{K=i+1}^{6} J_{ik}^{cyc}\ \hat{\mathbf{I}}_{H_i}^{cyc} \cdot\ \hat{\mathbf{I}}_{H_k}^{cyc}$$

$$(J_{13}^{cyc} = J_{14}^{cyc} = J_{56}^{cyc} = 0,\ \ \hat{\mathbf{I}} = I_x, I_y, I_z), \tag{5.11}$$

where $(H_i, i = 1..6)$ denote the ^{1}H spins. The corresponding resonance frequencies ($\nu_i^{cyc}, i = 1..6$) of cyclopentenone are indicated in Figure 5.3. The spin matrices are denoted $\hat{\mathbf{I}}_{H_i}^{cyc}$ with $i = 1..6$ and $\hat{\mathbf{I}} = (I_x, I_y, I_z)$.

The calculation was run as a state-to-state transfer with the initial and target operators for all spins chosen as follows:

The initial operator is given as follows,

$$I_{ini}^{cyc} = \sum_{i=1}^{6} I_{z_{H_i}}^{cyc}. \tag{5.12}$$

Target operators (TO_0^{cyc}, TO_1^{cyc}, TO_2^{cyc}, TO_3^{cyc} and TO_4^{cyc}) to generate optimal control pulses (0, 1, 2, 3 and 4) to excite proton group 0 ($H_1, H_2, H_3, H_4, H_5\ and\ H_6$ in Figure 5.4a, hard pulse), group1 ($H_3,\ H_4, H_5\ and\ H_6$ in Figure 5.4b), group 2 ($H_1\ and\ H_2$ in Figure 5.4c), group3 ($H_1, H_3, H_4, H_5\ and\ H_6$ in Figure 5.4d) and group 4 ($H_2, H_3,\ H_4,\ H_5\ and\ H_6$ in Figure 5.4e) were chosen as in Equations (5.13-5.17).

By introducing the abbreviations: $I_{z_{H_i}}^{cyc} = Z_i\ and\ I_{x_{H_i}}^{cyc} = X_i$, and skipping the sum sign, the target operators can be written as follows.

$$TO_0^{cyc} = X_1 X_2 X_3 X_4 X_5 X_6 \tag{5.13}$$

$$TO_1^{cyc} = Z_1 Z_2 X_3 X_4 X_5 X_6 \tag{5.14}$$

$$TO_2^{cyc} = X_1 X_2 Z_3 Z_4 Z_5 Z_6 \tag{5.15}$$

$$TO_3^{cyc} = X_1 Z_2 X_3 X_4 X_5 X_6 \tag{5.16}$$

$$TO_4^{cyc} = Z_1 X_2 X_3 X_4 X_5 X_6. \tag{5.17}$$

The quality factor of the calculation (U denotes the calculated pulse propagator) for e.g., the excitation of the signals of protons in group 1 is given by:

$$\emptyset = real\ (Trace\ (TO_1'\ U\ I_{ini}^{cyc}\ U'\ )). \tag{5.18}$$

The imaginary part is zero within the limits of precision of the calculation.

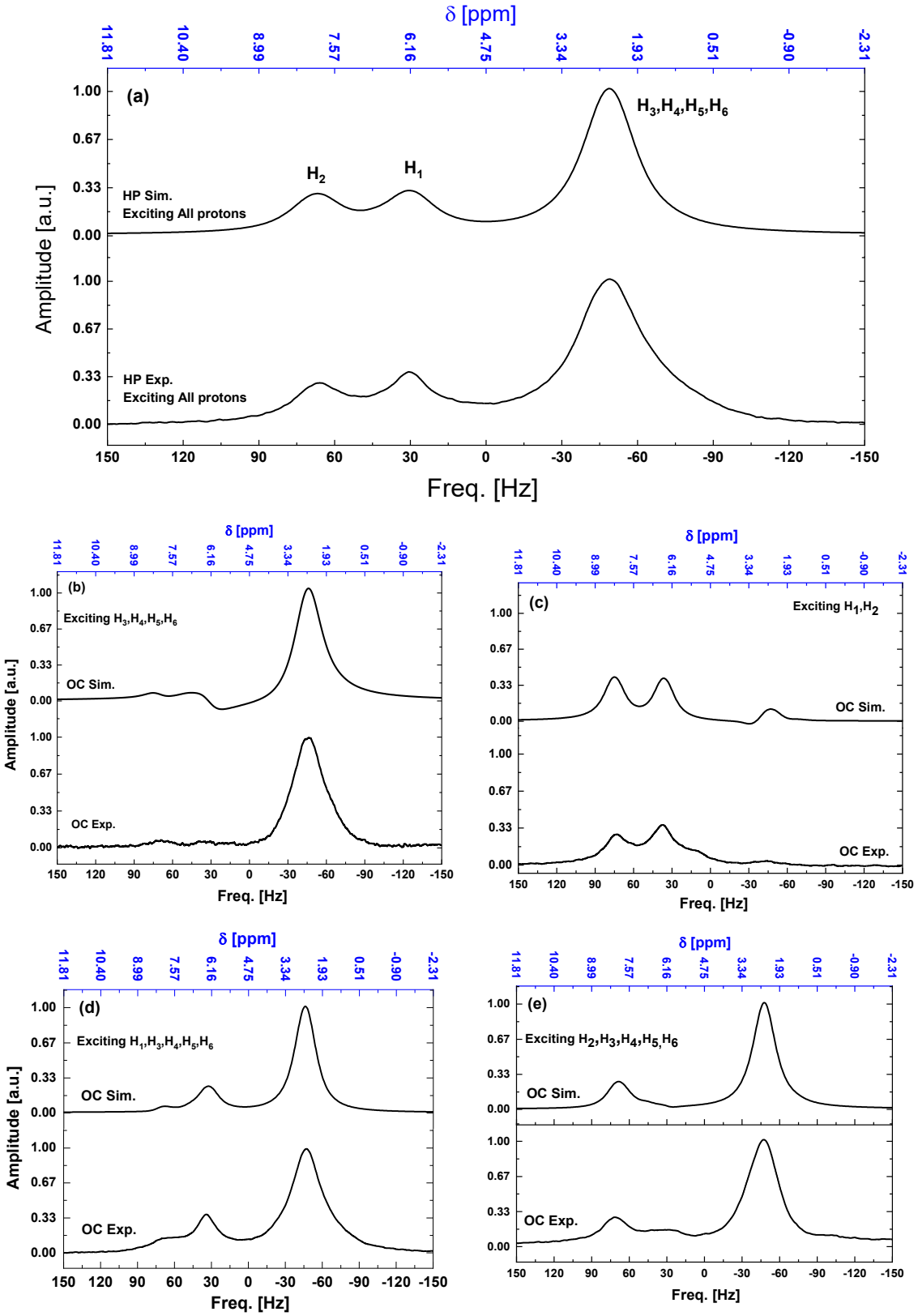

Figure 5.4: Simulated (upper spectrum of every stack plot) and experimental (lower spectrum of every stack plot) ^{1}H-NMR spectra (21.25 MHz) of cyclopentenone generated by **(a)** a hard pulse and the simulated and the experimental spectra using optimal control pulses to excite **(b)** group1 (H_3, H_4, H_5 and H_6), **(c)** group 2 (H_1 and H_2), **(d)** group3 (H_1, H_3, H_4, H_5 and H_6) and **(e)** group 4 (H_2, H_3, H_4, H_5 and H_6).

An excitation factor (EF) has been introduced to quantify the magnitude of the excited (wanted) signal after applying the optimal control pulses with respect to the full excitation using a hard pulse; the ideal excitation factor should be equal to 1. Likewise, a suppression factor (SF) serves to quantify the magnitude of the suppressed (unwanted) signal with respect to the same signal that is excited with a hard pulse; the ideal suppression factor should be equal to zero. EF and SF are shown in Figure 5.4, providing direct information about the quality of the optimal control pulses in both exciting the desired signal and suppressing the unwanted signal in experimental data.

Figure 5.5 shows the amplitude and the phase of the calculated OC pulse for the excitation of the (H_1, H_3, H_4, H_5 *and* H_6) proton groups in cyclopentenone. Remarkably, there is a 2 rad jump of the phase at times below 2.5 ms. A possible smoothing procedure [54] was tested to deal with this jump in phase by using an FT of the control amplitude vectors, setting the high frequency components to zero and then performing an inverse FT to return to the control amplitudes. We found that the performance of these smoothed pulses is much poorer than the performance of their unsmoothed counterparts. For this reason, we decided to use unsmoothed pulses throughout this investigation.

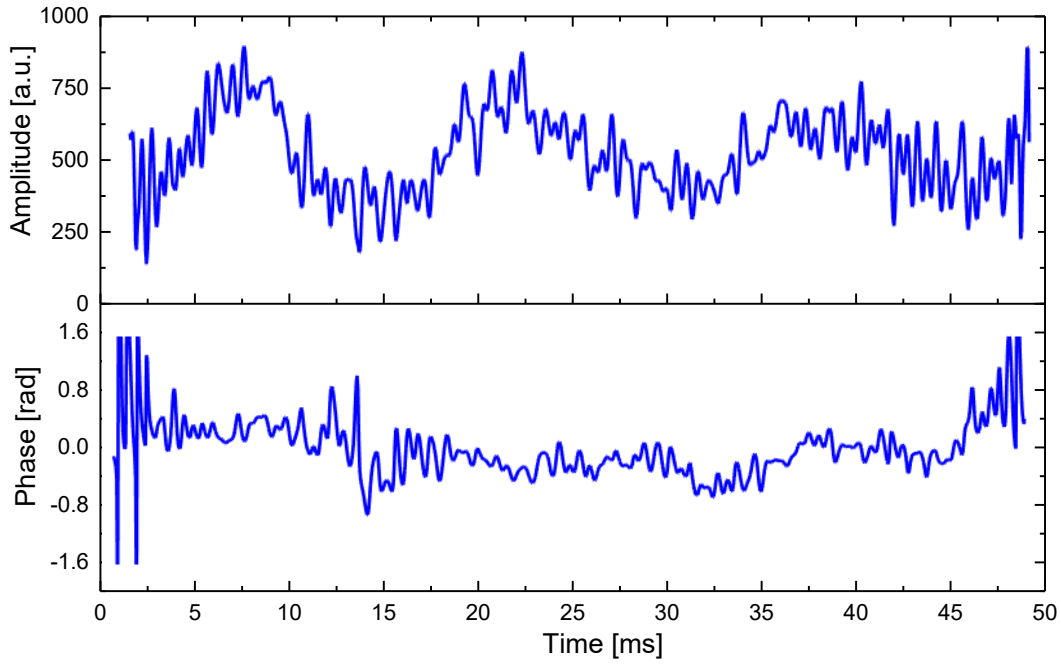

Figure 5.5: Pulse shape (amplitude (top) and phase (down)) of a cyclopentenone OC pulse for (H_1, H_3, H_4, H_5 and H_6) excitation.

The chart (Figure 5.6(a-c)) shows the performance of an OC pulse for cyclopentenone that is acting on group2 spins which is to suppress the signals of (H_3, H_4, H_5 and H_6) and to excite the signals of (H_1 and H_2) as a function of the OC pulse power.

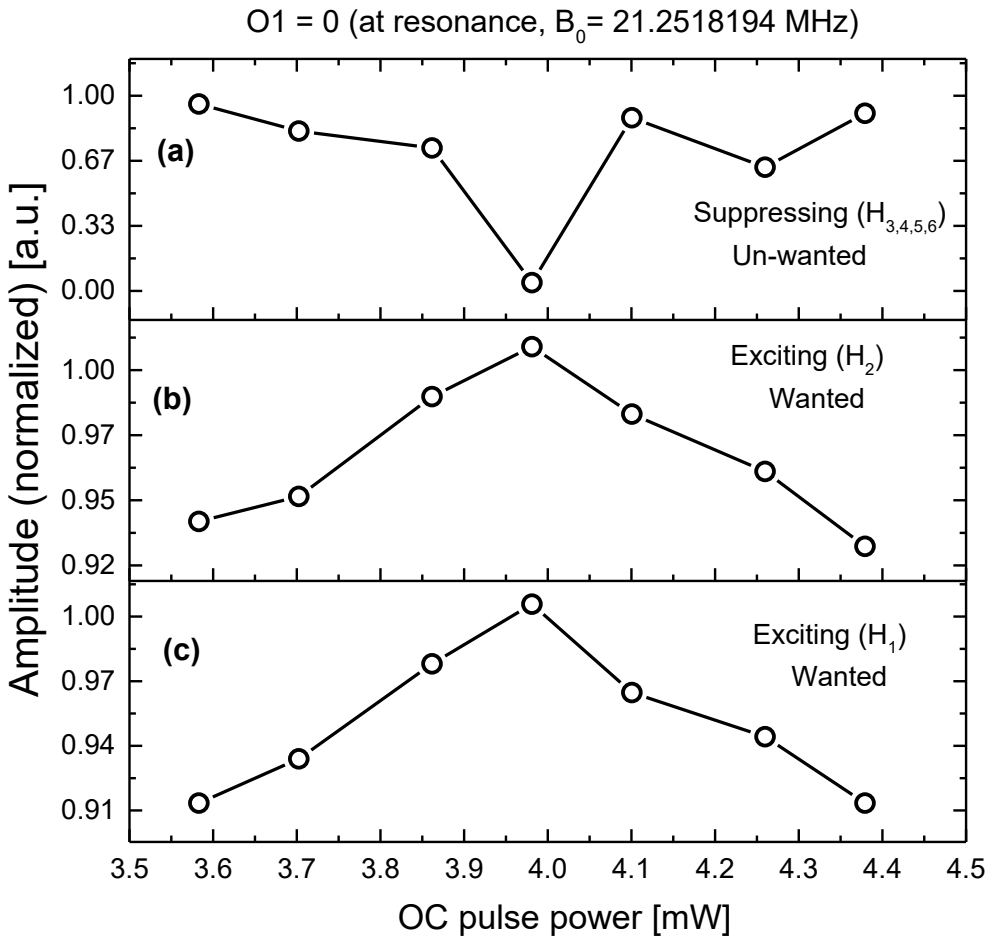

Figure 5.6: Performance of an OC pulse for cyclopentenone that is to suppress the signals of (H_3, H_4, H_5 and H_6) and to excite the signals of (H_1 and H_2) as a function of the OC pulse power.

The targeted signal can still be excited with 90% of its nominal amplitude at power levels that are 10% lower or higher than the optimum power level. However, the suppression of unwanted signal fails completely at power levels 10% higher or lower than the nominal one. The optimized optimal control (OC) power levels for groups 1, 2, 3, and 4 are 0.316 mW, 3.981 mW, 0.502 mW, and 0.199 mW, respectively and the center frequency set at resonance ($O_1 = 0$ Hz, B_0 =0.4991328 T, corresponding to an NMR frequency of 21.2518194 MHz).

To optimize the Gaussian pulses for selective excitation, the process begins by launching the pulse shape analysis tool in TopSpin using the command stdisp [155, 176]. In the new window, users can explore various options under the "Shapes" and "Analysis" menus. By selecting the folder icon in the upper left, opening "Gauss1.1000," and adjusting the shape size (with the default set to 1000 points), the amplitude plot reveals a Gaussian shape with constant phase. The user can then select "Analysis" followed by "Integrate Shape" and update the pulse length from previous calibration, which is typically set for a 90-degree hard

pulse. For example, after setting the pulse length to 27,000 µs for a 90-degree excitation, the system provides the power level difference between the shaped Gaussian pulse and the reference attenuation from prior hard-pulse calibration. This will indicate the adjusted power level required for this pulse (e.g., -164.5 dB, derived from an 11.5 dB baseline). Further, users can perform a simulation by selecting "Analysis" and "Simulation," updating the pulse parameters to 27,000 µs/90 degrees, and visualizing the excitation profile. After obtaining the x, y, and z profiles for the first pulse, the process can be repeated by adjusting the rotation angle to 270 degrees and the pulse length to 80,000 µs, allowing the user to print the new profiles [155]. These steps provide crucial information on optimizing the Gaussian pulse for targeted excitations.

In this study, Gaussian pulses were applied to cyclopentenone experiments alongside optimal control (OC) pulses for comparison. The Gaussian pulse used in the experiments had a 1% cutoff, offset at the targeted signal, with a maximum power level of 3.16 mW and a pulse length of 21.2 ms. The excitation and suppression factors obtained for both the Gaussian and OC pulses are presented in Table 5.3.

Table 5.3: The EF and SF factors of the signal groups excited using Gaussian and OC (Krotov) pulses. EF and SF Factors calculated using the absolute integration of the wanted and unwanted signal, resp. with respect to the absolute integration of the same signals after excitation with a hard pulse.

Cyclopentenone								
Factor	**group1** H_3, H_4, H_5 and H_6		**group 2** H_1 and H_2		**group 3** H_1, H_3, H_4, H_5 and H_6		**group 4** H_2, H_3, H_4, H_5 and H_6	
	OC Krotov	Gaussian	OC Krotov	Gaussian	OC Krotov	Gaussian	OC Krotov	Gaussian
EF	0.80	0.52	0.76	n.p.	0.74	n.p.	0.78	n.p.
SF	0.03	0.03	0.06	n.p.	0.05	n.p.	0.03	n.p.

n.p.: Not possible, as the signals fall within a frequency range where other desired signals also appear, making it impossible to selectively suppress the unwanted signals. Gaussian pulses can only excite or suppress a continuous range of frequencies.

Gaussian pulses suppress unwanted signals with a suppression factor (SF) of 0.03, comparable to the performance of Krotov selective pulses. However, the enhancement factor (EF) for the targeted signals is lower with Gaussian pulses, averaging 0.5, compared to 0.77 for OC pulses. Since Gaussian pulses operate over a continuous frequency range, they are unsuitable for metabolic profiling, where metabolites often have signals spanning a wide

range of frequencies with overlaps. As a result, Gaussian pulses are not ideal for selectively targeting individual metabolites in NMR studies.

5.3 Selective excitation in dual-system mixture

5.3.1 Example I: Benzoic acid and Alanine

An equimolar benzoic acid (BA) and alanine (Ala) mixture was used for demonstrating sub-spectral editing (of either BA or Ala signals) using OC pulses.

The proton NMR hard pulse spectra of the BA/Ala mixture taken at 21.25 MHz and 600.13 MHz and the enlargements of the resolved multiples at 600.13 MHz are shown in Figure 5.7a, 5.7b and 5.7c, respectively.

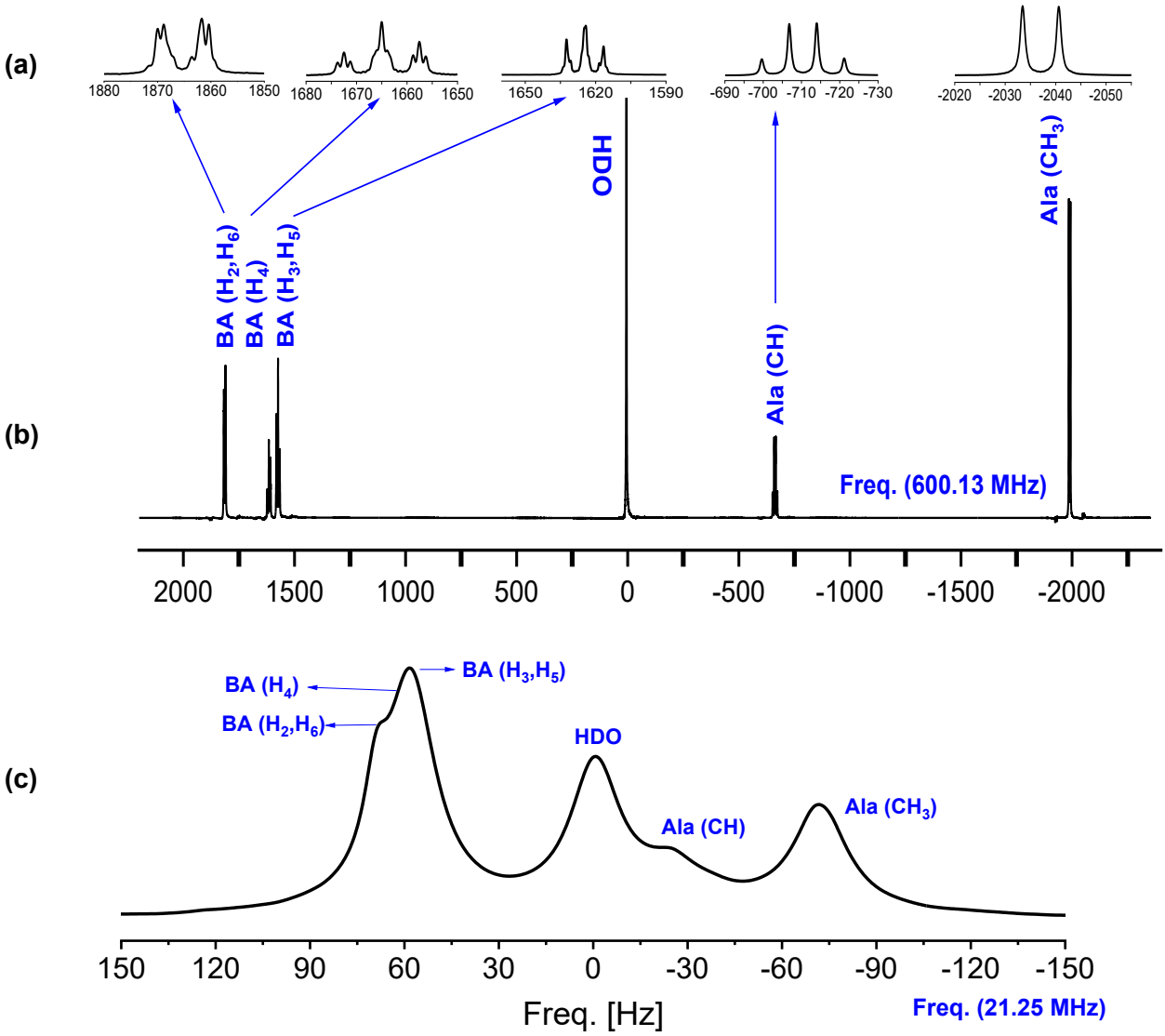

Figure 5.7: (a) Enlargements of the signals in the 600.13 MHz NMR spectrum showing the splitting patterns. **(b)** The full 600.13 MHz NMR spectrum. **(c)** The proton NMR hard pulse spectrum of a BA and Ala mixture measured at 21.25 MHz with the home-built low-frequency NMR spectrometer.

The three multiplet signals of the BA spectrum appeared as one broad signal with a shoulder at 21.25 MHz because their chemical shift differences are smaller than the linewidth (while they are well resolved at 600.13 MHz). The two Ala spectral lines appeared as two separate signals, the Ala CH-signal appearing at -22.5 Hz showed, however, a partial superposition with the water signal.

Like the analysis of cyclopentenone, the chemical shifts and the coupling constants of BA and Ala were determined from a first order analysis (Figure 5.8) of the spectrum at 600.13 MHz. Afterwards, the resonance frequencies at 21.25 MHz were obtained by downscaling the resonance frequencies to 21.25 MHz.

Benzoic acid

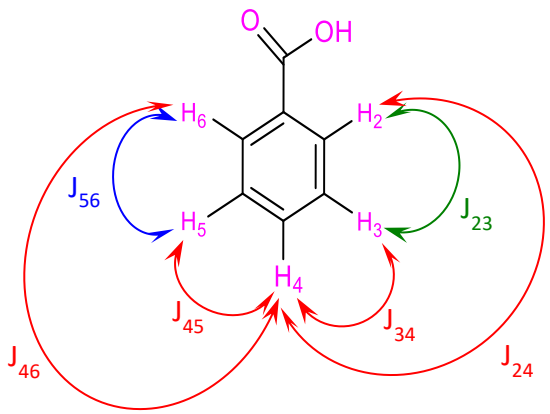

Alanine

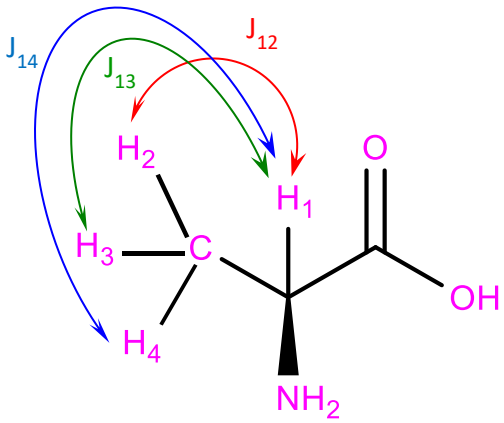

J-coupling [Hz]	NMR resonance positions [Hz] at	
	600.13 MHz	21.25 MHz
J_{23} = J_{56} = 8.44	$\nu_2 = \nu_6$ = 1864.74	$\nu_2 = \nu_6$ = 67.70
$J_{24} = J_{46}$ =1.6	$\nu_3 = \nu_5$ = 1624.58	$\nu_3 = \nu_5$ = 57.50
$J_{34} = J_{45}$ = 7.44	ν_4 = 1665.71	ν_4 = 60.30

J-coupling [Hz]	NMR resonance positions [Hz] at	
	600.13 MHz	21.25 MHz
$J_{12} = J_{13}$ = J_{14} = 7.2	ν_1 = -710.44 $\nu_2 = \nu_3 = \nu_4$ = -2037.31	ν_1 = -22.50 $\nu_2 = \nu_3 = \nu_4$ = -72.10

Figure 5.8: Visualization of the resonance frequencies and the coupling network of BA and Ala annotated on the 2D chemical structure. The two tables list the J-coupling, and the NMR resonance positions deduced from the NMR spectra at Figure 5.7 at two high-field NMR (600.13 MHz) and low-field NMR (21.25 MHz) for both amino acids BA and Ala respectively.

Optimal control pulses were calculated to excite either BA or Ala as a spectral editing experiment. To speed up the calculations, a system approach was applied, i.e., two systems

corresponding to the two compounds were chosen. The strong coupling Hamiltonian of the system 1 (BA) is given by

$$H_{BA} = 2\pi \sum_{i=2}^{6} \nu_i^1 \; I_{zH_i}^1 + 2\pi \sum_{i=2}^{6} \sum_{K=i+1}^{6} \mathrm{J}_{ik}^1 \, \hat{\mathbf{I}}_{H_i}^1 \cdot \hat{\mathbf{I}}_{H_k}^1$$

$$(\mathrm{J}_{25}^1 = \mathrm{J}_{26}^1 = \mathrm{J}_{35}^1 = \mathrm{J}_{36}^1 = 0, \; \hat{\mathbf{I}} = I_x, I_y, I_z), \tag{5.19}$$

where $(H_i, i = 2..6)$ denote the spins, and the corresponding resonance frequencies $(\nu_i^1, i = 2..6)$ of BA and are indicated in Figure 5.8. The corresponding spin matrices are denoted $\hat{\mathrm{I}}_{H_i}^1$ with $i = 2..6$ and $(\hat{\mathrm{I}} = I_x, I_y, I_z)$.

The Hamiltonian of system 2 (Ala) is given by:

$$H_{Ala}^2 = 2\pi \textstyle\sum_{i=2}^{4} \nu_i^2 \; I_{zH_i}^2 + 2\pi \sum_{i=1}^{3} \mathrm{J}_{1i}^2 \, \hat{\mathrm{I}}_{H_1}^2 \cdot \hat{\mathrm{I}}_{H_{i+1}}^2 \qquad (\hat{\mathrm{I}} = I_x, I_y, I_z), \tag{5.20}$$

where $(H_i, i = 1..4)$ denote the spins of Ala and are indicated in Figure 5.8. The corresponding spin operators are denoted $\hat{\mathrm{I}}_{H_i}^2$ with $i = 1..4$ and $(\hat{\mathrm{I}} = I_x, I_y, I_z)$. The resonance frequencies $(\nu_i^2, \; i = 1..4)$ are indicated as well in Figure 5.8 for both NMR frequencies.

The calculation was run as a state-to-state transfer with the initial operators for both systems being as follows:

$$I_{ini_{BA}}^1 = \textstyle\sum_{i=2}^{6} I_{zH_i}^1 \qquad (Initial\ operator\ 1) \tag{5.21}$$

$$I_{ini_{Ala}}^2 = \textstyle\sum_{i=1}^{4} I_{zH_i}^2. \qquad (Initial\ operator\ 2) \tag{5.22}$$

Target operators (TO_1, TO_2) to generate optimal control pulses to excite spin system 1 (BA) and spin system 2 (Ala) (Figure 5.9a) are denoted as follows:

$$TO_1 = \textstyle\sum_{i=2}^{6} I_{xH_i}^1 \qquad (\text{Target operator 1}) \tag{5.23}$$

$$TO_2 = \textstyle\sum_{i=1}^{4} I_{xH_i}^2 \, . \qquad (\text{Target operator 2}) \tag{5.24}$$

And to excite system 1 (BA) (Figure 5.9b):

$$TO_1 = \textstyle\sum_{i=2}^{6} I_{xH_i}^1 \qquad (\text{Target operator 1}) \tag{5.25}$$

$$TO_2 = \textstyle\sum_{i=1}^{4} I_{zH_i}^2. \qquad (\text{Target operator 2}) \tag{5.26}$$

And to excite system 2 (Ala) (Figure 5.9c):

$$TO_1 = \textstyle\sum_{i=2}^{6} I_{zH_i}^1 \qquad (\text{Target operator 1}) \tag{5.27}$$

$$TO_2 = \textstyle\sum_{i=1}^{4} I_{xH_i}^2. \qquad (\text{Target operator 2}) \tag{5.28}$$

The quality factor of the calculation (U_1 and U_2 denote the calculated pulse propagators for system 1 and system 2, resp.) is given by:

$$\emptyset = real\ (Trace\ (TO_1'\ U_1\ I_{ini}^1\ U_1')) + real\ (Trace\ (TO_2'\ U_2\ I_{ini}^1\ U_2')). \quad (5.29)$$

The imaginary part is zero within the limits of precision of the calculations.

Three optimal control pulses were calculated, simulated and performed at 21.25 MHz. The simulated and measured ^{1}H-NMR spectra using the first optimal control pulse at 21.25 MHz to excite both systems (BA and Ala) as a hard pulse (HP) are shown in Figure 5.9a. The second optimal control pulse was calculated to excite the BA proton spectrum while suppressing the Ala proton spectrum. Conversely, the third optimal control pulse was designed to excite Ala and suppress BA. The obtained simulated and experimental spectra are shown in Figures 5.9b and 5.9c, respectively.

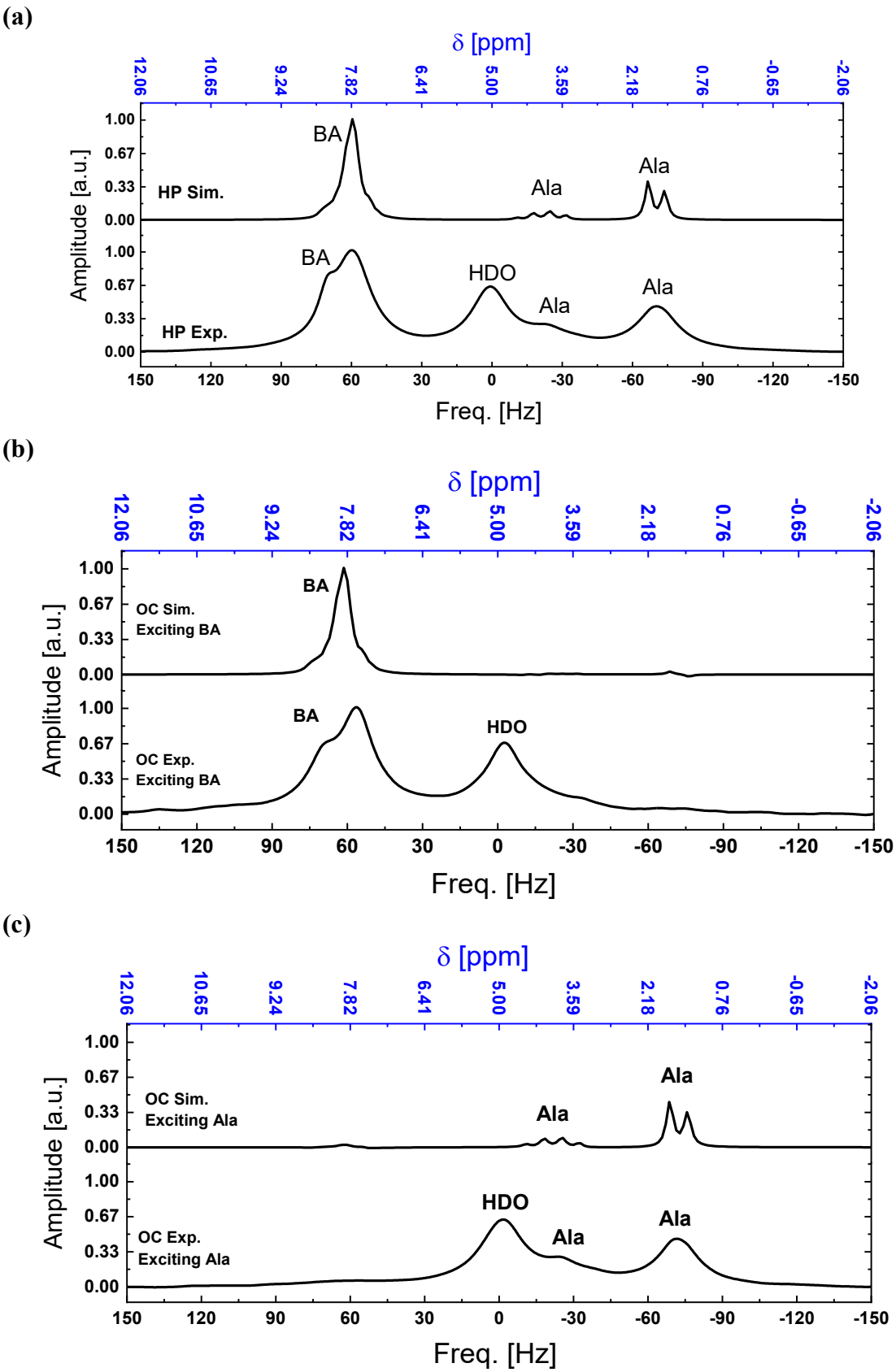

Figure 5.9: Simulated (upper spectrum of every stack plot) and experimental (lower spectrum of every stack plot) ^{1}H-NMR spectra (21.25 MHz) of BA and Ala mixture **(a)** both systems (Ba and Ala) are excited by OC pulse resulting as a hard pulse (HP), **(b)** spin system 1 (BA) and **(c)** spin system 2 (Ala). Signal of HDO appeared in the experimental spectra but not in the simulation.

To illustrate the effectiveness and benefits of optimal control (OC) pulses for manipulating entire spin systems (such as BA or Ala) compared to selective excitation with Gaussian pulses, experiments involving BA-Ala were conducted using both OC and Gaussian pulses. The excitation and suppression factors for both Gaussian and OC (Krotov) pulses are illustrated in Table 5.4. These factors, denoted as EF and SF, respectively, were computed based on the absolute integration of the desired and undesired signals relative to their integration after excitation with a hard pulse. The OC pulses proved effective even at low field strengths, down to 0.5 T, where strong coupling conditions prevail. By applying the Krotov algorithm to a mixture of benzoic acid and alanine, compound-selective excitation pulses were generated. These pulses selectively excite either the benzoic acid or alanine signals with minimal crosstalk, approximately 5%.

Table 5.4: EF and SF Factors for signal groups excited using Gaussian and OC (Krotov) pulses. EF and SF factors are calculated based on the absolute integration of the desired and undesired signals, respectively, relative to their integration after excitation with a hard pulse.

Factor	**Benzoic Acid**		**Alanine**	
	OC (Krotov)	Gaussian	OC (Krotov)	Gaussian
EF	0.78	0.55	0.77	0.53
SF	0.05	0.02	0.04	0.03

In the full proton system, even with proton coupling, the signals from five proton groups in BA are detected, primarily originating from α-protons attached to the central carbon atom in the benzyl group (3 protons in the methyl group) and from β-protons attached to the carbon atom adjacent to the nitrogen atom. All protons of BA together can be selectively excited with minimal interference from unwanted Ala, which was intentionally suppressed. Similarly, the three proton groups in Ala, including α-protons attached to the central carbon atom (3 protons in the methyl group), β-protons attached to the carbon atom adjacent to the carboxyl group, and γ-protons attached to the carbon atom adjacent to the amino group, can be selectively excited together with minimal residual signals from unwanted BA, which was also suppressed intentionally. This capability enables the application of selective excitation pulses for individual components in multi-component mixtures, expanding the utility of low-field NMR for various applications, including targeted metabolomics. Furthermore, with a library of spectral editing pulses, cost-effective and compact NMR spectrometers could be deployed in point-of-care settings such as medical offices or intensive care units, thereby enhancing the throughput of clinical sample analysis [21].

5.3.2 Example II: Phenylalanine -Taurine

A homogenous solution comprising of phenylalanine (Phe) and taurine (Tau) with equal molar concentrations in water was investigated to showcase the utilization of optimal control (OC) pulses for selective excitation and selective excitation. Figure 5.10 shows the ^{1}H-NMR spectra of Phe-Tau mixture in water acquired at low-field (29.93 MHz) and high-field (600.13 MHz) and the resonance frequencies of the signals are summarized in Figure 5.11. The high-field ^{1}H-NMR spectrum of Tau presents two characteristic triplets, positioned at 3.25 and 3.42 ppm, corresponding to the coupled protons (H_3, H_4) and (H_1, H_2) of $CH_2 - CH_2$ taurine backbone, respectively [177, 178]. Notably, these two triplets are unresolved by the low-field NMR (29.93 MHz) and are manifested as broad overlapping signals [179, 180].

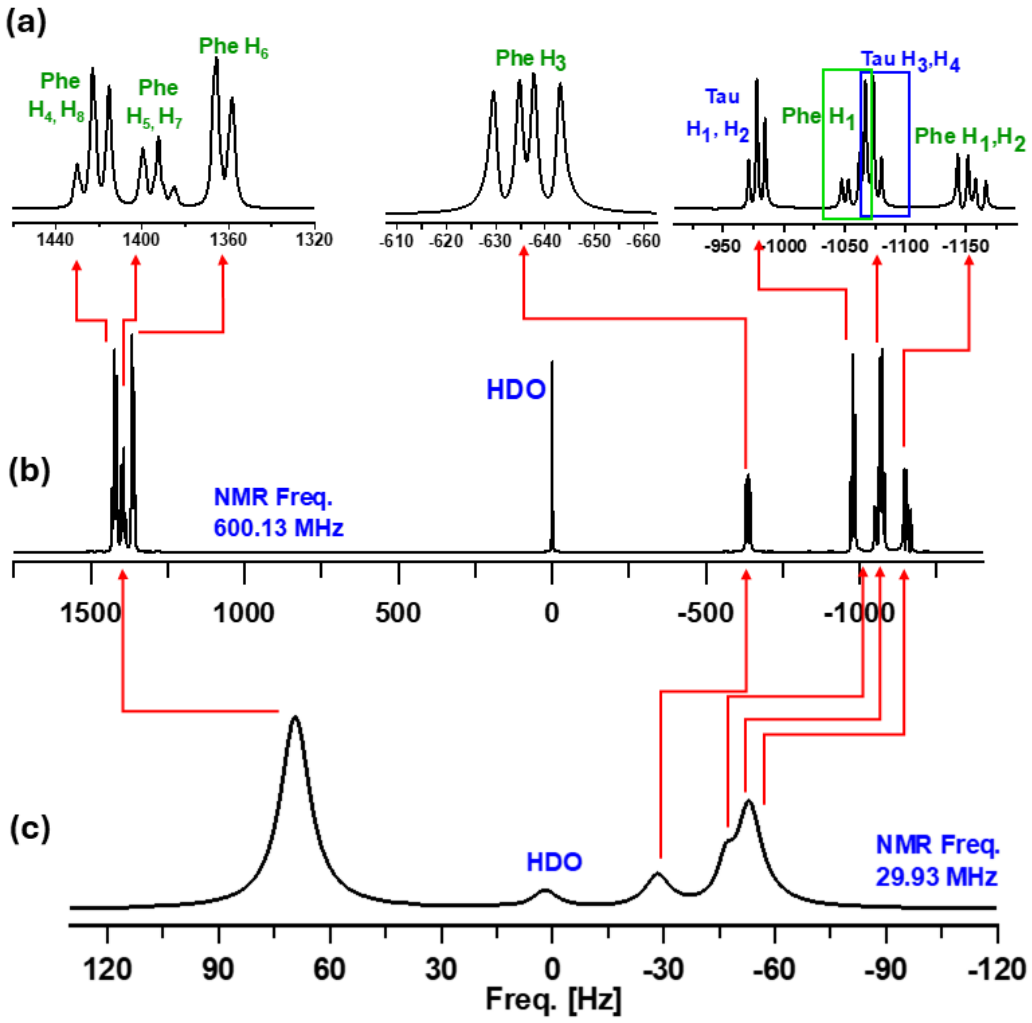

Figure 5.10: (a) Magnified views of the signals in the 600.13 MHz NMR spectrum reveal the multiplet splitting patterns. The ^{1}H-NMR spectra of a homogeneous mixture of Phe and Tau at equal molarities were obtained at **(b)** 600.13 MHz and **(c)** 29.93 MHz. High-field and low-field NMR measurements were performed using a Bruker AVANCE III NMR spectrometer and an in-house manufactured spectrometer, respectively.

The high-field ^{1}H-NMR spectrum of Phe-Tau mixture displays eight multiplet signals associated with the coupled protons. By setting the water signal at 0 Hz, the central resonance peaks of Phe appear at (-1057, -1154, -636, 1359, 1420, 1390 Hz) while for Tau appeared at (-977, -1070 Hz). At low-field NMR, Phe-Tau mixture exhibit three distinct peaks: (i) -52 Hz, which corresponds to the overlapped NMR signals of H_1, H_2, H_3, H_4 in the Tau molecule with the addition of H_1 and H_2 from the Phe molecule, all corresponding in high-field to the frequency range from -1166 to -970 Hz in the high-field spectrum; (ii) -30 Hz, corresponding to the overlapped NMR signals of H_3 in Phe, which corresponds to the frequency range -630 to -643 Hz in the high-filed spectrum; and (iii) 69.5 Hz, corresponding to the overlapped Phe NMR signals of H_4, H_5, H_6, H_7, and H_8 in the Tau-Phe mixture.

The chemical shifts (in Hz) and coupling constants (in Hz) of Phe and Tau were determined experimentally using first-order analysis of the 600.13 MHz NMR spectrum of a Phe-Tau mixture, with TSP as the reference (Figure 5.11).

To perform a selective excitation experiment, optimal control (OC) pulses were calculated to selectively excite either Phe or Tau. The strong coupling Hamiltonians for each spin system are described by Equations (5.30) and (5.31), corresponding to Phe and Tau, respectively.

$$H_{Phe} = 2\pi \sum_{i=1}^{8} v_i^1 I_{zH_i}^1 + 2\pi \sum_{i=1}^{7} \sum_{j=2}^{8} J_{ij}^1 I_{zH_i}^1 \cdot I_{zH_j}^1 \tag{5.30}$$

$$H_{Tau} = 2\pi \sum_{i=1}^{4} v_i^2 I_{zH_i}^2 + 2\pi \sum_{i=1}^{2} \sum_{j=3}^{4} J_{ij}^2 I_{zH_i}^2 \cdot I_{zH_j}^2, \tag{5.31}$$

where the spins $(H_i, i = 2,\ldots,6)$ and $(H_i, i = 1,\ldots,4)$ are assigned to the Phe and Tau molecules, respectively. Subsequently, three optimal control pulses are applied at 29.93 MHz.

Taurine (Tau)			Phenylalanine (Phe)		
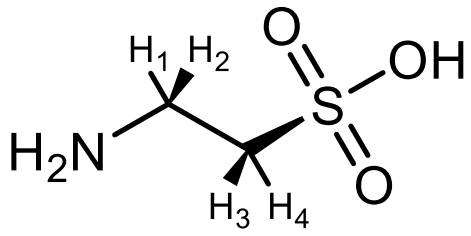			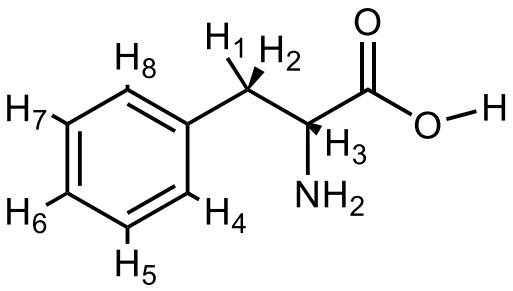		
J-Coupling [Hz]	NMR frequencies [Hz]		Coupling [Hz]	NMR frequencies [Hz]	
	600.13 MHz	29.93 MHz		600.13 MHz	29.93 MHz
$J_{13} = 6.74$ $J_{14} = 6.46$ $J_{23} = 6.40$ $J_{24} = 6.79$	$\nu_1 = \nu_2 = -977$ $\nu_3 = \nu_4 = -1070$	$\nu_1 = \nu_2 = -49$ $\nu_3 = \nu_4 = -53$	$J_{12} = -14.57$ $J_{13} = 8.01$ $J_{23} = 5.21$ $J_{46} = 1.59$ $J_{68} = 0.97$ $J_{45} = 7.91$ $J_{78} = 7.35$ $J_{67} = 7.53$ $J_{47} = 0.49$ $J_{56} = 5.21$ $J_{57} = 0.99$ $J_{48} = 1.42$	$\nu_1 = -1057$ $\nu_2 = -1154$ $\nu_3 = -636$ $\nu_4 = \nu_8 = 1359$ $\nu_5 = \nu_7 = 1420$ $\nu_6 = 1390$	$\nu_1 = -53$ $\nu_2 = -58$ $\nu_3 = -32$ $\nu_4 = \nu_8 = 68$ $\nu_5 = \nu_7 = 71$ $\nu_6 = 69$

Figure 5.11: Resonance frequencies and J-couplings of Phe and Tau at 29.93 and 600.13 MHz represented visually.

Pulse optimization: Optimal control pulses often exhibit highly variable, noise-like shapes, which can cause distortions and reduced fidelity if the hardware is not perfectly linear. Therefore, smoothness constraints were applied by filtering the pulses at each iteration and suppressing components far from resonance which produced relatively smooth pulses with experimental performance closely matching theoretical predictions. Additionally, suppressing non-resonant components lowered the total energy and reduced the specific absorption rate. This was demonstrated by the pulse shapes (phase and amplitude) used to selectively excite Phe while not exciting Tau, and vice versa, at an NMR frequency 600.13 MHz in Figure 5.12a, and at 29.93 MHz in Figure 5.12b.

During the evaluation, a significant 2 rad phase jump was observed in the pulse calculations. A smoothing procedure was tested but resulted in poorer performance compared to the unsmoothed pulses. Consequently, unsmoothed pulses were preferred for their effectiveness in resolving overlapping signals and ensuring better fidelity, particularly in low-field NMR applications.

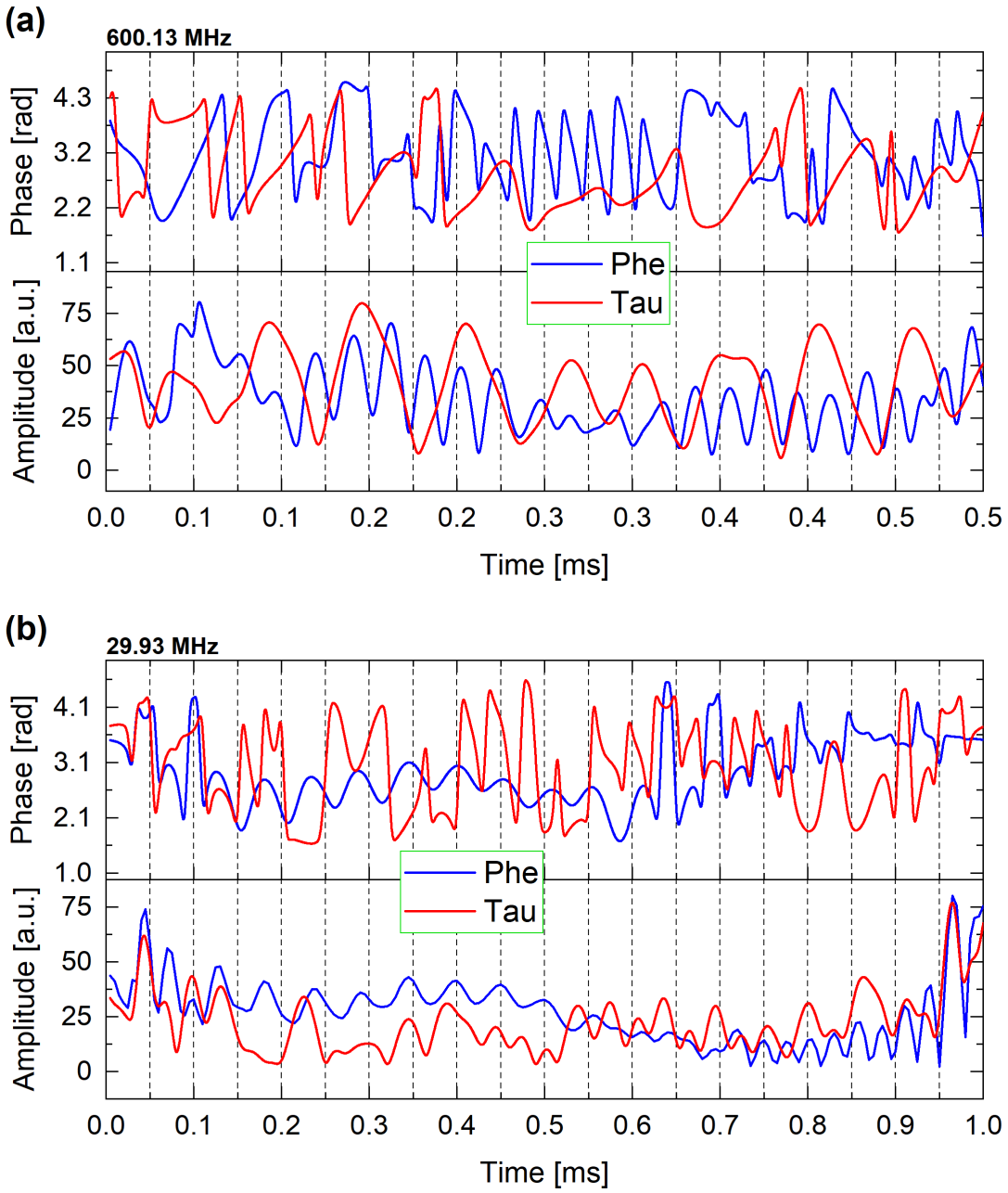

Figure 5.12: Pulse shapes (amplitude and phase) of the optimal controlled pulses to selectively excite Phe and Tau molecules at **(a)** low-field NMR (29.93 MHz) and **(b)** high-field NMR (600.13 MHz).

The initial OC pulse (Figure 5.13a) acquired at low LF-NMR (29.93 MHz) is tailored to induce excitation in both Phe and Tau molecules, and the resulting ^{1}H-NMR spectra, both

measured and simulated, are provided. Subsequently, the second and third optimal control pulses are computed to selectively stimulate either the Phe or Tau spectra while concurrently suppressing the other, as depicted in Figures 5.13b and 5.13c, respectively. In experimental validation (Figure 5.13e) demonstrates the implementation of the pulse designed to excite both Phe and Tau molecules, while Figures 5.13f and 5.13g exhibit the experimental outcomes of employing selective excitation pulses calculated to stimulate either the Phe or Tau spectra while suppressing the other, respectively.

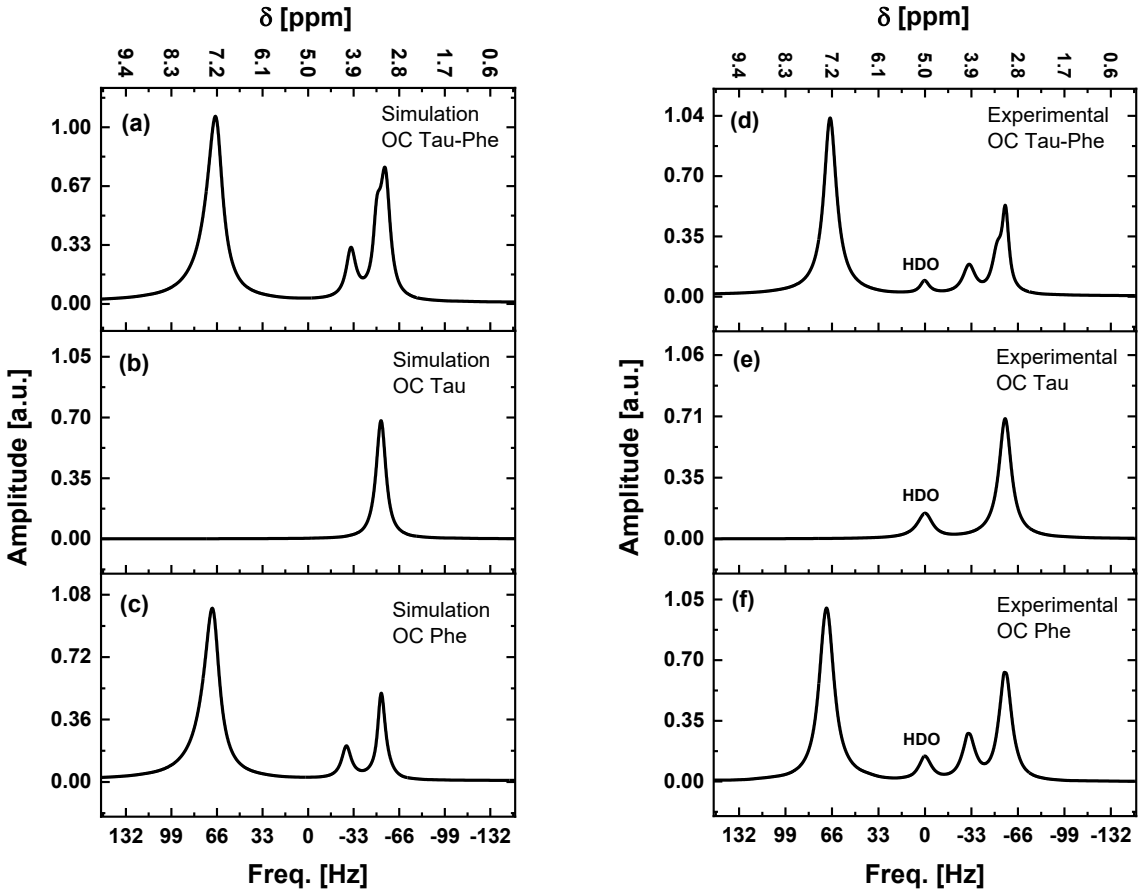

Figure 5.13: Stack plots of ^{1}H-NMR spectra (29.93 MHz) obtained from simulations (left spectra) and experiments (right spectra) of a homogeneous mixture of Phe and Tau, generated by optimal control pulses to excite: **(a** and **d)** both systems (Phe and Tau) using a hard pulse (HP); **(b** and **e)** spin system 1 (Phe); and **(c** and **f)** spin system 2 (Tau). The HDO signal is present in the experimental spectra but absent in the simulations, as HDO was not included in the simulation.

Gaussian pulses (GP) are widely used for selective excitation due to their defined frequency profiles. However, their effectiveness relies on signals being distributed across successive, non-overlapping frequency ranges throughout the spectrum. In cases where spectral components exhibit significant overlap or appear in non-successive frequency ranges—such as in the Phe-Tau spectrum within 1000-1100 Hz—GP fails to achieve the desired selectivity.

This limitation extends to many other systems with overlapping signals distributed across non-successive spectral regions. Nevertheless, to assess the efficacy of both Gaussian pulses and off-resonance irradiation with a carrier frequency (OC) pulse, experiments were conducted using GP with a 1% cutoff, offset at the targeted signal, a maximum power level of 3.16 μW, and a pulse duration of 21.2 ms. Notably, these experiments were conducted solely within the resolved frequency regions of the Phe-Tau spectrum. The excitation and suppression factors for both types of pulses were measured and presented in Table 5.5. The results indicate that Gaussian pulses achieved a suppression factor (SF) of 0.03 for the unwanted signal, which is comparable to the performance of Krotov optimized pulses. However, the excitation factor (EF) values for the targeted signals obtained using Gaussian pulses, averaging 0.55 for phenylalanine and 0.53 for taurine, were significantly lower than those achieved with OC pulses, which averaged 0.78 for phenylalanine and 0.77 for taurine.

Table 5.5: The EF and SF factors for the signal groups excited using GP and OC pulses. The EF and SF factors were calculated by comparing the absolute integrals of the target and interfering signals, respectively, to the absolute integrals of the same signals generated using a hard pulse.

Factor	Phenylalanine		Taurine	
	OC (Krotov)	Gaussian	OC (Krotov)	Gaussian
EF	0.78	0.55	0.77	0.53
SF	0.05	0.02	0.04	0.03

The Gaussian pulse exhibits a suppression factor (SF) of 0.03 for the unwanted signal, which is comparable to the performance of a Krotov selective pulse. However, the excitation factor (EF) values for the targeted signals obtained using Gaussian pulses (0.5 on average) differ significantly from those obtained using OC pulses (0.77 on average).

5.4 Challenges and solutions in NMR water suppression

In the analysis of organic samples, effective suppression of the dominant water signal is crucial to prevent it from overwhelming solute signals and compromising quantitative accuracy [181]. Techniques such as excitation sculpting and pulsed-field gradients are effective but require specialized pulse sequences and equipment [72]. Pre-saturation pulse sequences represent another alternative, but they may lead to incomplete suppression and transfer of pre-saturation effects to exchangeable protons, complicating their quantification [182-184]. Furthermore, pre-saturation can cause partial saturation near the saturated resonance, leading to erroneous quantification, as exemplified by the anomeric protons of α- and β-glucose, which resonate at 5.23 ppm and 4.67 ppm, respectively.

Ideally, NMR spectra should exhibit a flat baseline both below and above the water resonance, with adjustable signal levels achieved through phase corrections. To emphasize the importance of obtaining consistent NMR signals after water suppression, particularly in low-field NMR where challenges are more pronounced compared to high-field NMR, we present an experimental case focused on the NMR analysis of a phenylalanine and taurine (Phe-Tau) metabolite mixture under various conditions for comparative analysis (Figure 5.14).

Figure 5.14a shows the NMR spectrum acquired using hard pulse excitation without water suppression. The dominant water signal obscures other spectral features, making it impossible to extract spectral information or perform quantitative analysis of the Phe and Tau metabolites. Figure 5.14b presents the results obtained with hard pulse excitation and a pre-saturation water suppression protocol. Although the water signal was suppressed with minimal residual effects, the NMR signals of Phe-Tau in the -30 Hz range were attenuated due to their proximity to the water signal. Signals centered around -52 Hz and 69.5 Hz experienced less attenuation.

Figure 5.14c shows the NMR spectrum of the same sample dissolved in natural D_2O, effectively removing the water signal without the need for additional suppression techniques. This spectrum reveals clear Phe and Tau signals with amplitude ratios like those obtained using optimal control pulses for water suppression, demonstrating the effectiveness of this non-invasive approach. While pre-saturation techniques are effective, they often lead to longer measurement times and introduce delays between successive acquisitions. These delays can be particularly problematic in in-situ NMR studies, where rapid data collection is essential. To address these challenges, we developed a non-invasive, straightforward water suppression technique using optimal control pulses (selective excitation). This method effectively mitigates the water signal, producing clear NMR spectra of phenylalanine and taurine with amplitude ratios comparable to those obtained using D_2O, as shown in Figure 5.14c.

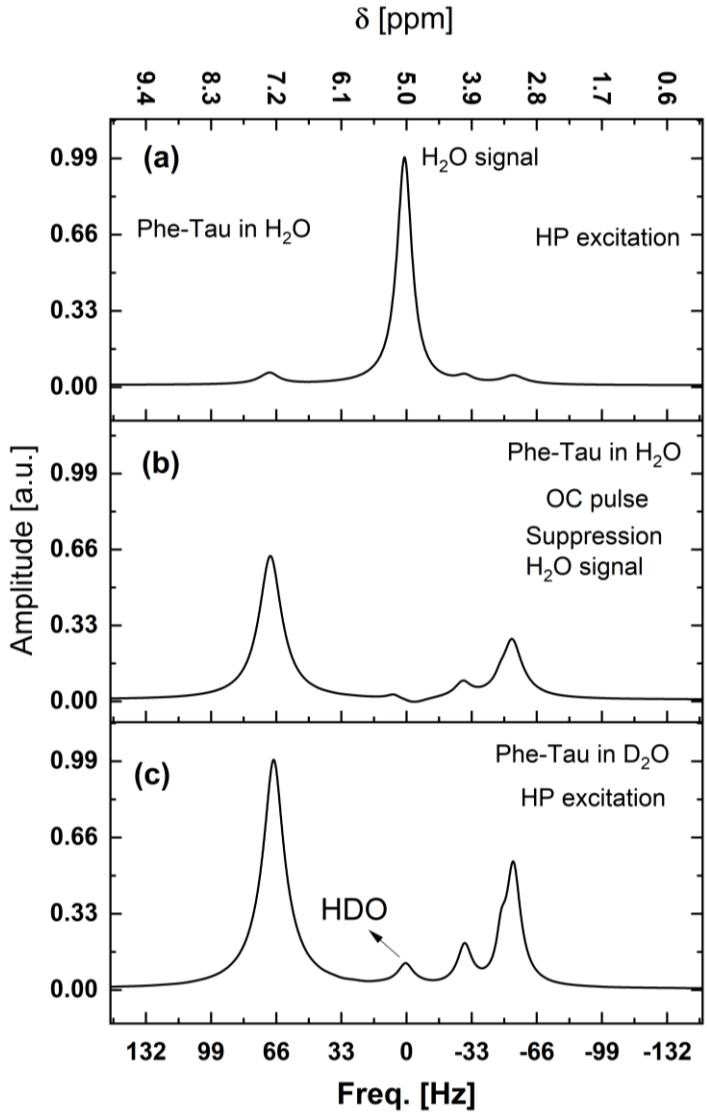

Figure 5.14: ^{1}H-NMR spectra of Phe-Tau in $H_2O - D_2O$ (with 10% D_2O) recorded at a frequency of 29.93 MHz. The NMR spectra were acquired using **(a)** hard pulse excitation, **(b)** hard pulse excitation with included water suppression, and **(c)** hard pulse excitation of the same Phe-Tau system, dissolved in pure D_2O to eliminate the water signal for comparative analysis.

We present a simple and robust water suppression technique based on an optimal control pulse that allows the acquisition of high-quality ^{1}H-NMR spectra of metabolites in both high- and low-field NMR spectroscopy. The Hamiltonian used for water suppression is provided below.

$$H_{water} = 2\pi \sum_{i=-3}^{3} v_i^3 I_{zH_i}^3 \; (v_i^3 = -6, -4, -2, 0, 2, 4, 6\, Hz; i = -3, -2, -1, 0, 1, 2, 3). \quad (5.32)$$

The Phe-Tau sample was prepared in a solvent containing 10% H_2O and 90% D_2O with a volume of 500 µL.

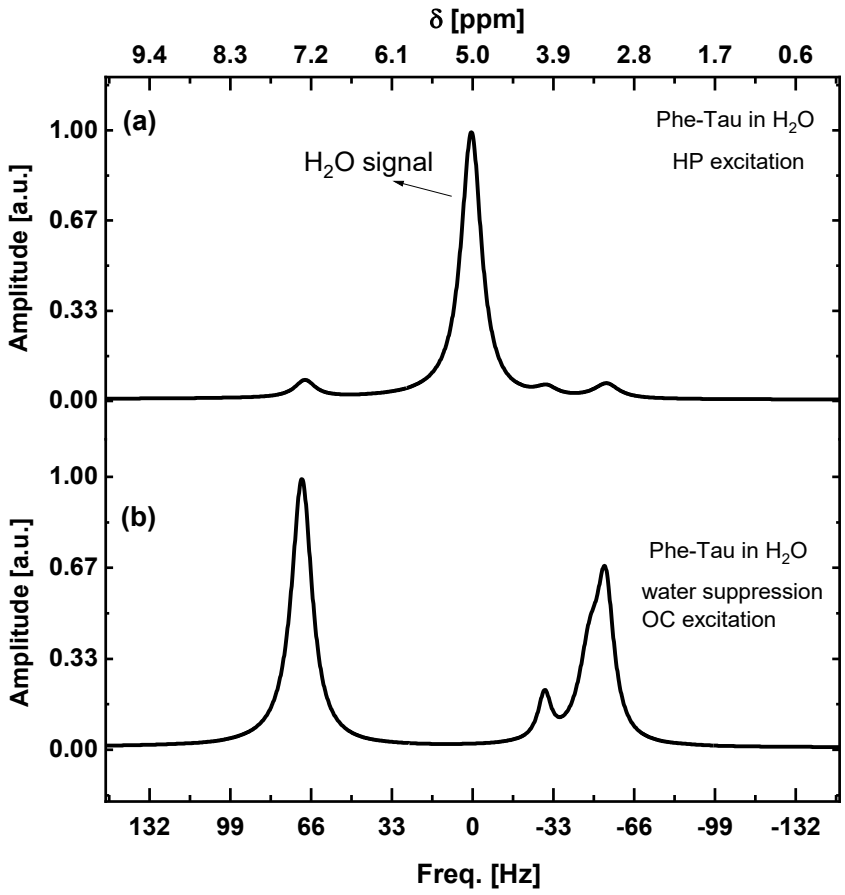

Figure 5.15: ^{1}H-NMR spectra of Phe-Tau in $H_2O - D_2O$ (with 10% D_2O) measured at a frequency of 29.93 MHz. The NMR spectra were obtained using two excitation methods: **(a)** conventional hard pulse excitation and **(b)** optimized control pulse excitation, where the water signal was selectively suppressed, and only the Phe and Tau signals were excited.

Evidently, in Figure 5.15a, the water signal dominates the solute signals (Phe-Tau). However, employing optimal control pulse excitation allowed specific suppression of the water signal (Figure 5.15b), achieving efficient signal excitation without increasing the experiment duration. This suppression was accomplished by aligning water magnetization along the z-axis. Additionally, the receiver amplification was tuned to match the magnitude of the solute signals, avoiding interference from the water signal.

The amplitude and integrated area of the Phe and Tau signals, following water suppression with optimal control pulses, are comparable to those in the spectrum in Figure 5.14, in which the analytes were measured in D_2O.

5.5 Dipolar decoupling: WAHUHA

The primary objective of this work is to enhance the analytical capabilities of low-field nuclear magnetic resonance (NMR) spectroscopy for characterizing complex organic mixtures by addressing challenges such as spectral broadening and signal overlap. In low-field NMR, reduced chemical shift dispersion and magnetic field inhomogeneities contribute to broader signals, leading to overlapping peaks and decreased resolution. Dipolar couplings, typically averaged out in solution-state NMR, may re-emerge in systems with restricted motion, further causing broadening. This work examines the impact of spectral broadening on low-field NMR lineshapes and explores strategies to mitigate these effects. Additionally, the limited spectral range in low-field NMR results in significant signal overlap, complicating metabolite identification and structural determination [107-109].

NMR signal broadening in liquid-state samples arises from factors such as magnetic field inhomogeneities, J-couplings, and chemical exchange. In highly viscous samples, such as biological fluids, restricted molecular tumbling prevents the complete averaging of dipole-dipole couplings [185, 186]. While magic angle spinning (MAS) NMR is a common method for reducing these anisotropic interactions, it requires specialized hardware and sample preparation, making it costly and complex. Furthermore, adapting MAS for low-field NMR poses additional challenges, such as the need for wider bore magnets, which compromise the achievable field strength.

To address these limitations, homonuclear decoupling sequences such as WAHUHA, FSLG, PMLG, and DUMBO are used to mitigate spectral broadening without requiring MAS [187]. These sequences employ phase cycling to average dipolar couplings, enhancing resolution. In this study, we applied multiple-pulse WAHUHA line-narrowing to a Phe-Tau sample embedded in agarose gel. The agarose gel restricts molecular motion, allowing residual dipolar couplings to persist, which mimics the behavior of biological tissues and other highly viscous samples.

The WAHUHA sequence was implemented using Bruker's Topspin software, with pulse parameters, including timing, phasing, and looping, detailed in Figure 5.16. This method effectively reduced line broadening and provided high-resolution spectra of the Phe-Tau sample, demonstrating the technique's potential for improving resolution in low-field NMR applications.

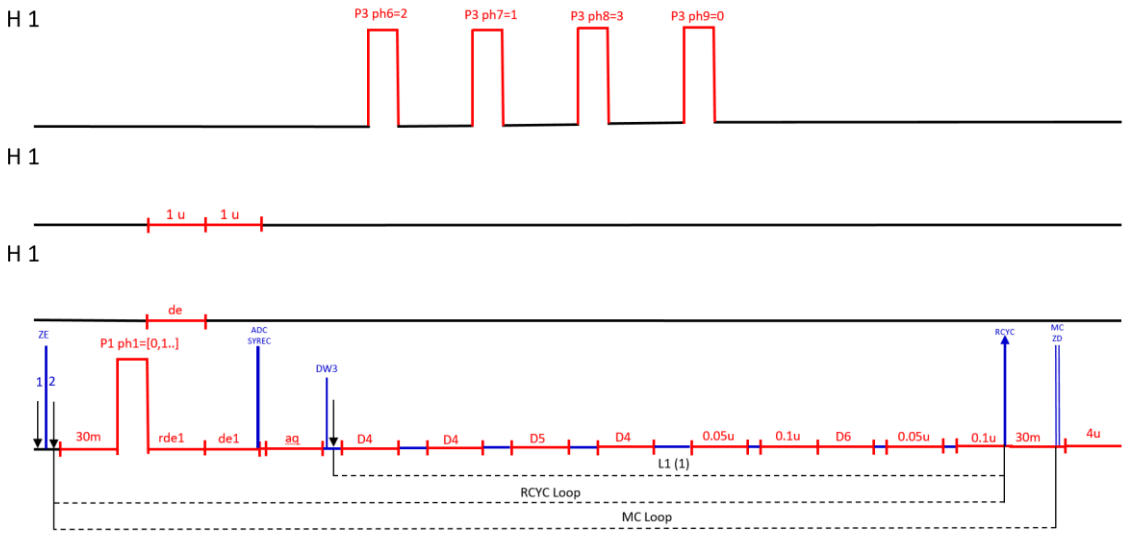

Figure 5.16: Schematic representation of the multiple-pulse WAHUHA sequence implemented using the AU programming language of Bruker.

The parameters conform to standard Bruker nomenclature: "D" indicates delay time in microseconds (e.g., D4, D5, D6), "P" represents the applied RF pulse, and "ph (1…n)" denotes the phase of the applied RF pulse. "H1" designates the proton channel, "RECY loop" indicates looping, and "u" signifies the unit in microseconds. The notation "30m" stands for a duration of 30 milliseconds.

Before applying the sequence of π/2 pulses with acquisitions, there is a 30 ms delay. Correction times in microseconds are added to the waiting times to achieve refocusing. At the end of the first loop, there is another 30 ms delay before starting the looping process again (MC loop). Looping is divided into three types based on the starting time: L1, RECY loop, and MC loop. This division is essential for achieving final refocusing and preventing additional broadening.

Agarose gel (1.5 wt.%) was selected as the material, serving as an intermediate between solid-state and liquid-state NMR, to investigate the performance of the WAHUHA sequence. The viscosity of the agarose gel was adjusted based on the curve in Figure 5.17 to achieve an approximate linewidth of 20 Hz, making it a suitable approximation for biological tissue.

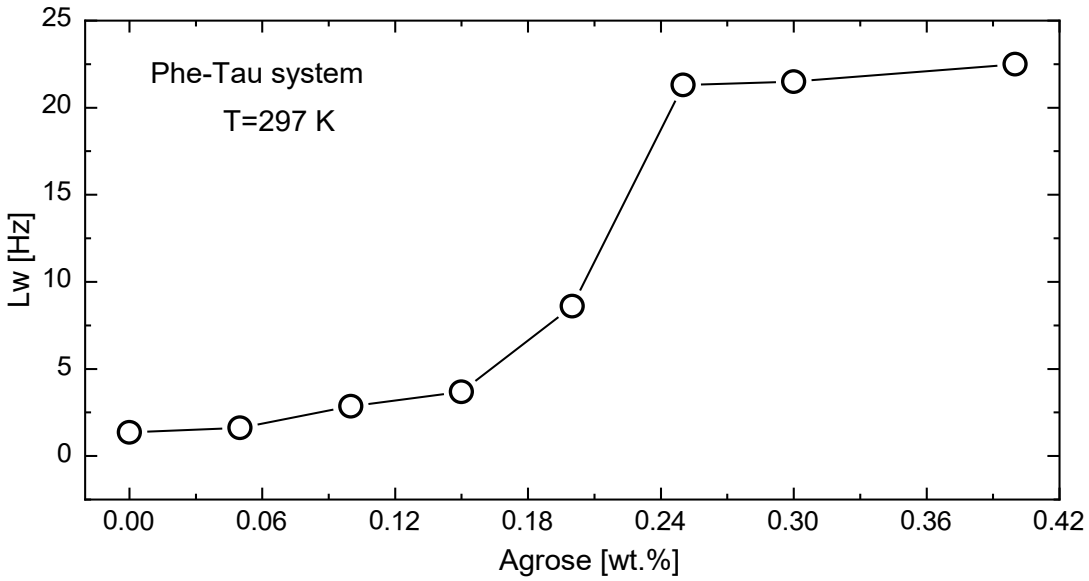

Figure 5.17: Relationship between NMR line broadening and agarose gel concentration in wt.% at 297 K.

The implementation of the WAHUHA sequence for acquiring Phe-Tau NMR spectra at a frequency of 29.93 MHz resulted in a significant reduction in the linewidth at half maximum, decreasing from 20 Hz to 15 Hz (Figures 5.18a and 5.18b). Furthermore, applying the WAHUHA sequence to the Phe-Tau sample in combination with agarose gel at high-field NMR (600.13 MHz) reduced the average linewidth from 8 Hz to 3 Hz (as demonstrated in Figures 5.18c and 5.18d). In general, multiple-pulse sequences such as WAHUHA not only average the dipolar Hamiltonian but also influence other Hamiltonians, including chemical shift anisotropies (CSA), to an extent determined by the specific sequence. Notably, the WAHUHA sequence scales CSA by a factor of $1/\sqrt{3}$. To account for this scaling effect, the chemical shifts were corrected post-WAHUHA application using the internal reference compound TSP.

In comparison, the linewidth of Phe-Tau in D_2O without agarose gel was approximately 16 Hz at low-field NMR (Figure 5.18). When the multiple-pulse WAHUHA sequence was applied, it resulted in a linewidth reduction of approximately 63% at high-field NMR and 25% at low-field NMR. These reductions, evident from the changes in the NMR spectra, highlight the effectiveness of the WAHUHA sequence in minimizing linewidth broadening at both field strengths, although the impact is more pronounced at high-field NMR.

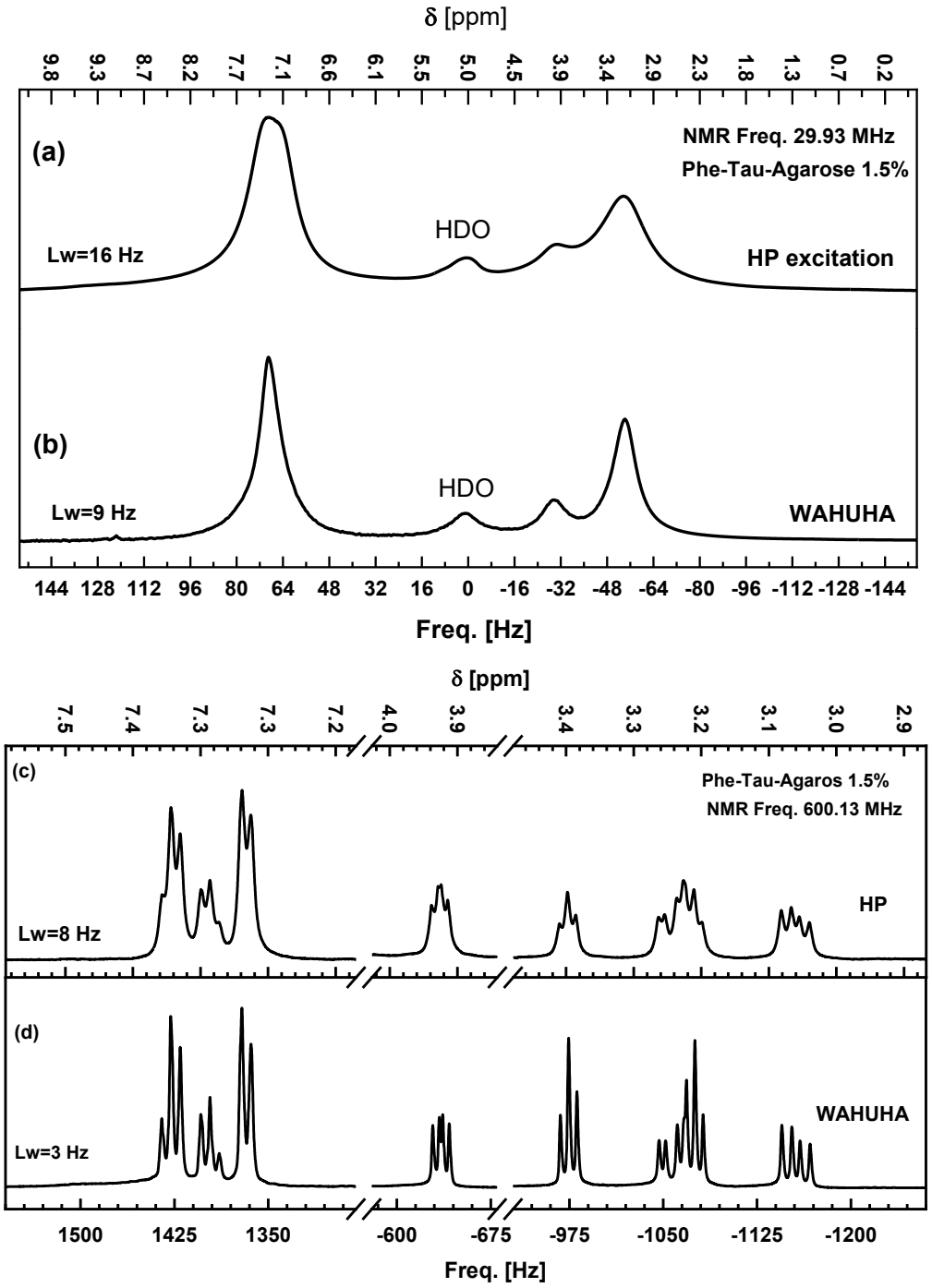

Figure 5.18: Comparison of ^{1}H-NMR spectra for Phe-Tau in D_2O and agarose gel (1.5 wt.%) measured at NMR frequencies of 29.93 MHz and 600.13 MHz, respectively. The spectrum in **(a)** corresponds to standard hard pulse excitation, while **(b)** shows the spectrum acquired using the multiple-pulse WAHUHA sequence, which effectively eliminates homonuclear dipolar coupling. The spectrum in **(c)** represents the Phe-Tau sample in D_2O, and **(d)** demonstrates the Phe-Tau sample in agarose gel using the same WAHUHA sequence at high magnetic field.

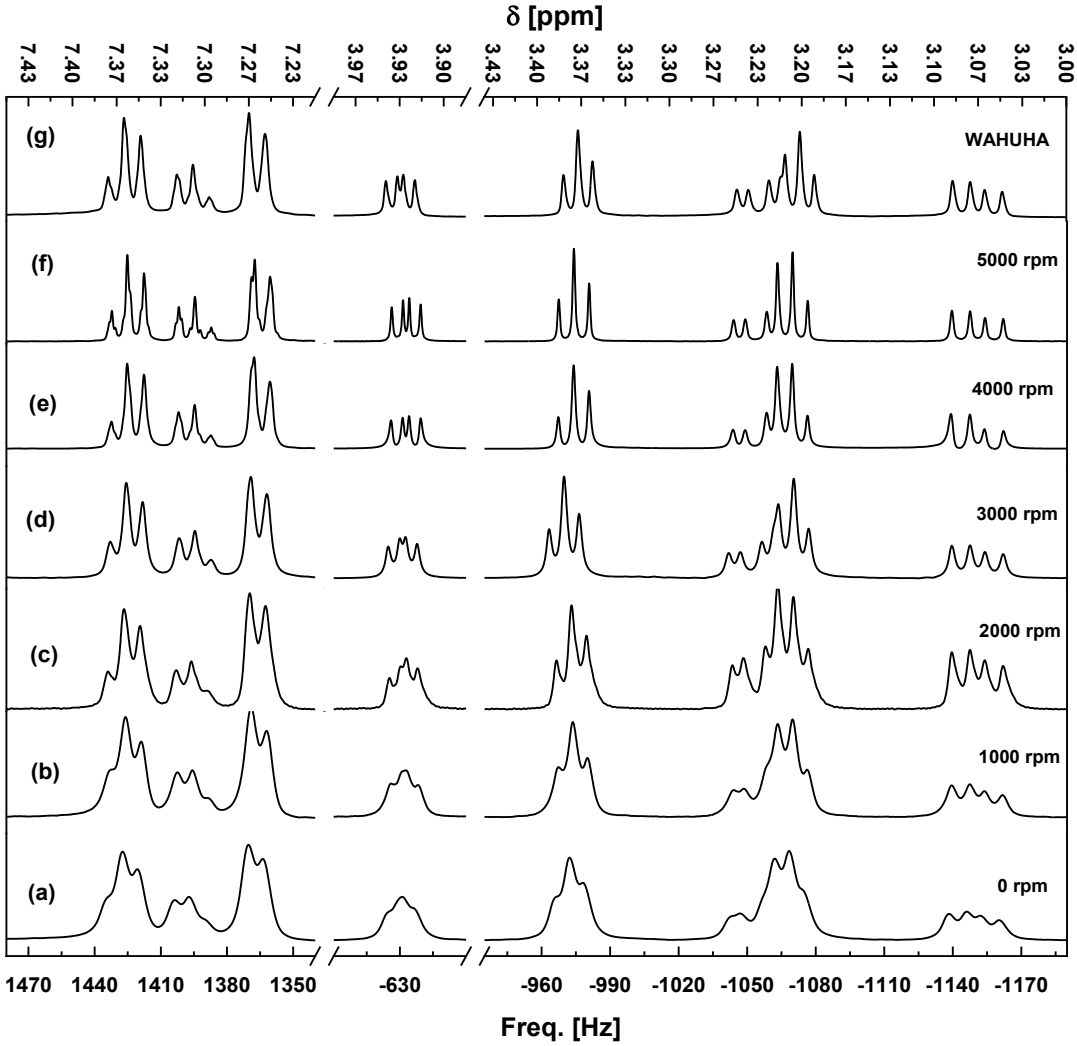

Figure 5.19: Comparison of ^{1}H-NMR high-resolution magic angle spinning (HRMAS) spectra of Phe-Tau in D_2O and agarose gel (1.5 wt.%) acquired at an NMR frequency of 600.13 MHz. The spectra were measured at different spinning rates: **(a)** 0 rpm, **(b)** 1000 rpm, **(c)** 2000 rpm, **(d)** 3000 rpm, **(e)** 4000 rpm, and (f) 5000 rpm. The effectiveness of the multiple-pulse WAHUHA sequence in eliminating homonuclear dipolar coupling is comparable to the HRMAS spectra obtained at spinning rates between 2000 and 3000 rpm.

The effectiveness of this process was validated by comparing its performance to that of magic angle spinning (MAS) NMR. A series of high-resolution magic angle spinning (HRMAS) measurements were performed using the same sample as in the WAHUHA experiments. The HRMAS spectra, shown in Figure 5.19, were acquired at different spinning rates. Specifically, the spectra in Figure 5.19c and Figure 5.19d correspond to spinning rates of 2000 rpm and 3000 rpm, respectively. These spectra exhibited an average linewidth reduction of approximately 5 Hz compared to the measurement taken without spinning (0 rpm). This reduction in linewidth at spinning rates of 2000 rpm and 3000 rpm is comparable to the improvement achieved with the WAHUHA sequence, demonstrating the equivalence of these two methods in minimizing linewidth broadening.

6 Summary and conclusions

This study introduces a low-field NMR (LF-NMR) spectrometer with a multilayer Halbach magnet, integrated mechanical and electrical shimming systems, and a compact probehead. Operating at frequencies of 21.25 MHz and 29.93 MHz, the LF-NMR spectrometer was designed, validated, and successfully used for metabolic mixture measurements. It demonstrated notable capabilities in selective excitation, dipolar decoupling, and optimal control (OC) water suppression.

The Halbach magnet, consisting of three nested cylindrical magnets with an inner mechanical shimming layer, improved field homogeneity. The magnet's design, combined with sophisticated shimming and an onboard NMR probehead, advanced portable and low-field NMR technologies. The rotatable array facilitated magnetic field shimming in the z-y plane, improving homogeneity compared to conventional dipolar permanent magnets.

A compact, integrated probehead optimized impedance discrepancies and signal loss to a minimum. The implementation of OC pulses, guided by the Krotov algorithm, proved effective in molecular and sub-spectral excitations, exemplified by spectral editing of acetic acid, highlighting the spectrometer's versatility, even with its limited pulse programming capabilities.

This study demonstrates the potential of low-field NMR for targeted analysis of overlapping spectral lines, positioning benchtop NMR as an efficient tool for process analytics. Applications of the LF-NMR system could expand into various fields, including analytical chemistry and process monitoring.

To compare OC pulses with Gaussian pulses, experiments on cyclopentenone showed that while both pulses achieved a similar signal suppression factor (SF) of 0.03, the excitation factors (EF) differed significantly: 0.5 for Gaussian pulses versus 0.77 for OC pulses. This highlights the limitations of Gaussian pulses for targeted metabolic profiling, especially when signals are widely spread.

Further validation confirmed that OC pulses are effective for sub-spectral editing at low field strengths (0.5 and 0.7 T), under strong coupling conditions. Using the Krotov algorithm, we calculated selective excitation pulses for a benzoic acid and alanine mixture, achieving minimal crosstalk (5% from alanine and 4% from benzoic acid). For cyclopentenone, signals from aliphatic and olefinic protons were edited with low crosstalk.

Combining this approach with a Halbach magnet offering a large homogeneous volume could expand the application of low-field NMR, particularly in targeted metabolomics. A low-cost, space-efficient NMR spectrometer with a library of spectral editing pulses could be used in

point-of-care settings, such as doctors' offices or ICUs, increasing the throughput of clinical samples.

The study demonstrates that OC pulses enable spectral editing in both low-field (29.93 MHz) and high-field (600.13 MHz) NMR. Furthermore, the Krotov selective excitation pulse was successfully applied to a phenylalanine and taurine mixture, exciting specific resonances despite severe overlap.

The WAHUHA sequence on a 2.0% agarose Phe-Tau sample reduced homonuclear dipolar coupling by 63% in high-field and 25% in low-field NMR, like the effect achieved at an HRMAS spinning rate of 2000-3000 rpm. Additionally, water suppression was achieved using OC pulses, treating water molecules as an independent system within the multi-component mixture. This work underscores the potential of low-field NMR, supported by OC pulses and the WAHUHA sequence, to function as a programmable detector.

References

[1] R. Saborano *et al.*, "A framework for tracer-based metabolism in mammalian cells by NMR," *Scientific reports,* vol. 9, no. 1, pp. 1-13, 2019.

[2] B. Blümich, "Low-field and benchtop NMR," *Journal of Magnetic Resonance,* vol. 306, pp. 27-35, 2019.

[3] P. Blümler and F. Casanova, "Hardware developments: Halbach magnet arrays," *Mobile NMR and MRI: developments and applications,* vol. 133, 2015.

[4] J. Anders and K. Lips, "MR to go," *Journal of Magnetic Resonance,* vol. 306, pp. 118-123, 2019.

[5] M. Grootveld *et al.*, "Progress in low-field benchtop NMR spectroscopy in chemical and biochemical analysis," *Analytica chimica acta,* vol. 1067, pp. 11-30, 2019.

[6] B. Luy, "Towards Portable High-Resolution NMR Spectroscopy," *Angewandte Chemie International Edition,* vol. 50, no. 2, pp. 354-356, 2011.

[7] L. H. Antonides *et al.*, "Rapid identification of novel psychoactive and other controlled substances using low-field ^{1}H NMR spectroscopy," *Acs Omega,* vol. 4, no. 4, pp. 7103-7112, 2019.

[8] G. Assemat *et al.*, "Diffusion-ordered spectroscopy on a benchtop spectrometer for drug analysis," *Journal of pharmaceutical and biomedical analysis,* vol. 160, pp. 268-275, 2018.

[9] J. Duffy, A. Urbas, M. Niemitz, K. Lippa, and I. Marginean, "Differentiation of fentanyl analogues by low-field NMR spectroscopy," *Analytica chimica acta,* vol. 1049, pp. 161-169, 2019.

[10] D. Fallaise, H. Balkwill Tweedie, J. Konzuk, C. Cheyne, E. E. Mack, and J. G. Longstaffe, "Practical application of ^{1}H benchtop NMR spectroscopy for the characterization of a nonaqueous phase liquid from a contaminated environment," *Magnetic Resonance in Chemistry,* vol. 57, no. 2-3, pp. 93-100, 2019.

[11] M. Leutzsch, A. J. Sederman, L. F. Gladden, and M. D. Mantle, "In situ reaction monitoring in heterogeneous catalysts by a benchtop NMR spectrometer," *Magnetic resonance imaging,* vol. 56, pp. 138-143, 2019.

[12] D. Gołowicz, K. Kazimierczuk, M. Urbańczyk, and T. Ratajczyk, "Monitoring hydrogenation reactions using benchtop 2D NMR with extraordinary sensitivity and spectral resolution," *ChemistryOpen,* vol. 8, no. 2, p. 196, 2019.

[13] B. Gouilleux, N. V. Christensen, K. G. Malmos, and T. Vosegaard, "Analytical evaluation of low-field 31P NMR spectroscopy for lipid analysis," *Analytical chemistry,* vol. 91, no. 4, pp. 3035-3042, 2019.

[14] M. K. Sørensen, N. M. Balsgart, O. Jensen, N. C. Nielsen, and T. Vosegaard, "Fast wide-line solid-state NMR on a low-cost benchtop spectrometer," *ChemPhysChem,* vol. 19, no. 22, pp. 2985-2988, 2018.

[15] B. Blümich, "Introduction to compact NMR: A review of methods," *TrAC Trends in Analytical Chemistry,* vol. 83, pp. 2-11, 2016.

[16] K. Saalwächter, "Applications of NMR in Polymer Characterization–An Introduction," 2019.

[17] L. O. Sillerud *et al.*, "^{1}H NMR Detection of superparamagnetic nanoparticles at 1 T using a microcoil and novel tuning circuit," *Journal of Magnetic Resonance,* vol. 181, no. 2, pp. 181-190, 2006.

[18] D. P. Cistola and M. D. Robinson, "Compact NMR relaxometry of human blood and blood components," *TrAC Trends in Analytical Chemistry,* vol. 83, pp. 53-64, 2016.

[19] C. A. Michal, "Low-cost low-field NMR and MRI: Instrumentation and applications," *Journal of Magnetic Resonance,* vol. 319, p. 106800, 2020.

[20] K.-M. Lei *et al.*, "Portable NMR with parallelism," *Analytical chemistry,* vol. 92, no. 2, pp. 2112-2120, 2020.

[21] G. Assemat *et al.*, "Benchtop low-field ^{1}H Nuclear Magnetic Resonance for detecting falsified medicines," *Talanta,* vol. 196, pp. 163-173, 2019.

[22] D. Fallaise, J. Konzuk, C. Cheyne, E. E. Mack, and J. G. Longstaffe, "Nontargeted Analysis of a Non-Aqueous-Phase Liquid From a Chemical Manufacturing Site Using Nuclear Magnetic Resonance Spectroscopy," *Environmental toxicology and chemistry,* vol. 38, no. 5, pp. 947-955, 2019.

[23] D. Gołowicz, P. Kasprzak, V. Orekhov, and K. Kazimierczuk, "Fast time-resolved NMR with non-uniform sampling," *Progress in nuclear magnetic resonance spectroscopy,* vol. 116, pp. 40-55, 2020.

[24] D. Bouillaud *et al.*, "Using benchtop NMR spectroscopy as an online non-invasive in vivo lipid sensor for microalgae cultivated in photobioreactors," *Process Biochemistry,* vol. 93, pp. 63-68, 2020.

[25] S. Bukkapatna Chakrapani, "Multicomponent Polymer Systems: Polymer Compositional Analysis using Low-Field ^{1}H-NMR Spectroscopy and Tuning the Compositional Drift in Styrene/Isoprene Anionic Copolymerizations," 2019.

[26] E. Mylonakis *et al.*, "T2 magnetic resonance assay for the rapid diagnosis of candidemia in whole blood: a clinical trial," *Clinical Infectious Diseases,* vol. 60, no. 6, pp. 892-899, 2015.

[27] B. C. Percival *et al.*, "Low-field, benchtop NMR spectroscopy as a potential tool for point-of-care diagnostics of metabolic conditions: Validation, protocols and computational models," *High-throughput,* vol. 8, no. 1, p. 2, 2019.

[28] Q. Gong, A. Gordji-Nejad, B. Blümich, and S. Appelt, "Trace analysis by low-field NMR: breaking the sensitivity limit," *Analytical chemistry,* vol. 82, no. 17, pp. 7078-7082, 2010.

[29] T. Castaing-Cordier, D. Bouillaud, P. Bowyer, O. Gonçalves, P. Giraudeau, and J. Farjon, "Highly Resolved Pure-Shift Spectra on a Compact NMR Spectrometer," *ChemPhysChem,* vol. 20, no. 5, pp. 736-744, 2019.

[30] E. R. McCarney, R. Dykstra, and P. Galvosas, "Evaluation of benchtop NMR Diffusion Ordered Spectroscopy for small molecule mixture analysis," *Magnetic resonance imaging,* vol. 56, pp. 103-109, 2019.

[31] S. Chinthalapalli, A. Bornet, T. F. Segawa, R. Sarkar, S. Jannin, and G. Bodenhausen, "Ultrahigh-resolution magnetic resonance in inhomogeneous magnetic fields: two-dimensional long-lived-coherence correlation spectroscopy," *Physical Review Letters,* vol. 109, no. 4, p. 047602, 2012.

[32] N. Doğan, R. Topkaya, H. Subaşi, Y. Yerli, and B. Rameev, "Development of Halbach magnet for portable NMR device," *Journal of physics: conference series,* vol. 153, no. 1, p. 012047, 2009.

[33] N. Doğan, R. Topkaya, H. Subaşi, Y. Yerli, and B. Rameev, "Development of Halbach magnet for portable NMR device," in *Journal of Physics: Conference Series*, 2009, vol. 153, no. 1: IOP Publishing, p. 012047.

[34] J. A. Aguilar, S. Faulkner, M. Nilsson, and G. A. Morris, "Pure shift ^{1}H NMR: a resolution of the resolution problem?," *Angewandte Chemie International Edition,* vol. 49, no. 23, pp. 3901-3903, 2010.

[35] K. Zangger and H. Sterk, "Homonuclear broadband-decoupled NMR spectra," *Journal of Magnetic Resonance,* vol. 124, no. 2, pp. 486-489, 1997.

[36] X. Chen, G. Bertho, C. Caradeuc, N. Giraud, and C. Lucas-Torres, "Present and future of pure shift NMR in metabolomics," *Magnetic Resonance in Chemistry,* vol. 61, no. 12, pp. 654-673, 2023.

[37] K. Halbach, "Strong rare earth cobalt quadrupoles," *IEEE Transactions on Nuclear Science,* vol. 26, no. 3, pp. 3882-3884, 1979.

[38] K. Halbach, "Design of permanent multipole magnets with oriented rare earth cobalt material," *Nuclear instruments and methods,* vol. 169, no. 1, pp. 1-10, 1980.

[39] J. Mallinson, "One-sided fluxes--A magnetic curiosity?," *IEEE Transactions on magnetics,* vol. 9, no. 4, pp. 678-682, 1973.

[40] H. Raich and P. Blümler, "Design and construction of a dipolar Halbach array with a homogeneous field from identical bar magnets: NMR Mandhalas," *Concepts in Magnetic Resonance Part B: Magnetic Resonance Engineering: An Educational Journal,* vol. 23, no. 1, pp. 16-25, 2004.

[41] R. Bjørk, C. R. H. Bahl, A. Smith, and N. Pryds, "Comparison of adjustable permanent magnetic field sources," *Journal of Magnetism and Magnetic Materials,* vol. 322, no. 22, pp. 3664-3671, 2010.

[42] C. W. Windt, H. Soltner, D. Van Dusschoten, and P. Blümler, "A portable Halbach magnet that can be opened and closed without force: The NMR-CUFF," *Journal of Magnetic Resonance,* vol. 208, no. 1, pp. 27-33, 2011.

[43] G. Moresi and R. Magin, "Miniature permanent magnet for table-top NMR," *Concepts in Magnetic Resonance Part B: Magnetic Resonance Engineering: An Educational Journal,* vol. 19, no. 1, pp. 35-43, 2003.

[44] A. Sarwar, A. Nemirovski, and B. Shapiro, "Optimal Halbach permanent magnet designs for maximally pulling and pushing nanoparticles," *Journal of magnetism and magnetic materials,* vol. 324, no. 5, pp. 742-754, 2012.

[45] B. Hills, K. Wright, and D. Gillies, "A low-field, low-cost Halbach magnet array for open-access NMR," *Journal of Magnetic Resonance,* vol. 175, no. 2, pp. 336-339, 2005.

[46] M. W. Vogel, A. Giorni, V. Vegh, R. Pellicer-Guridi, and D. C. Reutens, "Rotatable small permanent magnet array for ultra-low field nuclear magnetic resonance instrumentation: A concept study," *PloS one,* vol. 11, no. 6, p. e0157040, 2016.

[47] L. Isolan and M. Sumini, "Magnetic quadrupole simulations for focusing the electron beams emitted by a plasma focus device," *Radiation Physics and Chemistry,* vol. 174, p. 108970, 2020.

[48] S. Zaremba and W. Kleeven, "Cyclotrons: magnetic design and beam dynamics," *arXiv preprint arXiv:1804.08961,* 2018.

[49] N. Khaneja, T. Reiss, C. Kehlet, T. Schulte-Herbrüggen, and S. J. Glaser, "Optimal control of coupled spin dynamics: design of NMR pulse sequences by gradient ascent algorithms," *Journal of magnetic resonance,* vol. 172, no. 2, pp. 296-305, 2005.

[50] Z. Tošner, T. Vosegaard, C. Kehlet, N. Khaneja, S. J. Glaser, and N. C. Nielsen, "Optimal control in NMR spectroscopy: Numerical implementation in SIMPSON," *Journal of Magnetic Resonance,* vol. 197, no. 2, pp. 120-134, 2009.

[51] K. Chen, "A Practical Review of NMR Lineshapes for Spin-1/2 and Quadrupolar Nuclei in Disordered Materials," *International Journal of Molecular Sciences,* vol. 21, no. 16, p. 5666, 2020.

[52] Y. Maday, "Reduced basis method for the rapid and reliable solution of partial differential equations," 2006.

[53] I. I. Maximov, Z. Tošner, and N. C. Nielsen, "Optimal control design of NMR and dynamic nuclear polarization experiments using monotonically convergent algorithms," *The Journal of Chemical Physics,* vol. 128, no. 18, p. 05B609, 2008.

[54] I. I. Maximov, J. Salomon, G. Turinici, and N. C. Nielsen, "A smoothing monotonic convergent optimal control algorithm for nuclear magnetic resonance pulse sequence design," *The Journal of chemical physics,* vol. 132, no. 8, p. 084107, 2010.

[55] M. Holbach, J. Lambert, and D. Suter, "Optimized multiple-quantum filter for robust selective excitation of metabolite signals," *Journal of Magnetic Resonance,* vol. 243, pp. 8-16, 2014.

[56] M. Holbach, J. Lambert, S. Johst, M. E. Ladd, and D. Suter, "Optimized selective lactate excitation with a refocused multiple-quantum filter," *Journal of Magnetic Resonance,* vol. 255, pp. 34-38, 2015.

[57] R. Freeman and G. A. Morris, "The 'DANTE'experiment," *Journal of Magnetic Resonance,* vol. 213, no. 2, pp. 244-246, 2011.

[58] C. Bauer, R. Freeman, T. Frenkiel, J. Keeler, and A. Shaka, "Gaussian pulses," *Journal of Magnetic Resonance (1969),* vol. 58, no. 3, pp. 442-457, 1984.

[59] J. S. Waugh, L. M. Huber, and U. Haeberlen, "Approach to high-resolution NMR in solids," *Physical Review Letters,* vol. 20, no. 5, p. 180, 1968.

[60] J. Choi, H. Zhou, H. S. Knowles, R. Landig, S. Choi, and M. D. Lukin, "Robust dynamic hamiltonian engineering of many-body spin systems," *Physical Review X,* vol. 10, no. 3, p. 031002, 2020.

[61] M. H. Goerz *et al.*, "Krotov: A Python implementation of Krotov's method for quantum optimal control," 2019.

[62] O. Beckonert *et al.*, "High-resolution magic-angle-spinning NMR spectroscopy for metabolic profiling of intact tissues," *Nature protocols,* vol. 5, no. 6, pp. 1019-1032, 2010.

[63] A. Bahti, A. Telfah, J. Lambert, R. Hergenröder, and D. Suter, "Optimal control pulses for subspectral editing in low field NMR," *Journal of Magnetic Resonance,* vol. 328, p. 106993, 2021.

[64] M. J. Shapiro and J. S. Gounarides, "High resolution MAS-NMR in combinatorial chemistry," *Biotechnology and bioengineering,* vol. 71, no. 2, pp. 130-148, 2000.

[65] R. A. Wind and J. Z. Hu, "In vivo and ex vivo high-resolution ^{1}H NMR in biological systems using low-speed magic angle spinning," Pacific Northwest National Lab.(PNNL), Richland, WA (United States …, 2006.

[66] J. Waugh, L. Huber, and U. Haeberlen, "Approach to high-resolution NMR in solids," *Physical Review Letters,* vol. 20, no. 5, p. 180, 1968.

[67] M. Renault, L. Shintu, M. Piotto, and S. Caldarelli, "Slow-spinning low-sideband HR-MAS NMR spectroscopy: delicate analysis of biological samples," *Scientific reports,* vol. 3, no. 1, pp. 1-5, 2013.

[68] H. Gogiashvili, "Based Quantitative Metabolomics in Breast Cancer," ed: Metabolites.

[69] Y. Huang, Z. Zhang, H. Chen, J. Feng, S. Cai, and Z. Chen, "A high-resolution 2D J-resolved NMR detection technique for metabolite analyses of biological samples," *Scientific Reports,* vol. 5, no. 1, pp. 1-9, 2015.

[70] F. M. Paruzzo and L. Emsley, "High-resolution ^{1}H NMR of powdered solids by homonuclear dipolar decoupling," *Journal of Magnetic Resonance,* vol. 309, p. 106598, 2019.

[71] J. H. Bothwell and J. L. Griffin, "An introduction to biological nuclear magnetic resonance spectroscopy," *Biological Reviews,* vol. 86, no. 2, pp. 493-510, 2011.

[72] T.-L. Hwang and A. Shaka, "Water suppression that works. Excitation sculpting using arbitrary wave-forms and pulsed-field gradients," *Journal of Magnetic Resonance, Series A,* vol. 112, no. 2, pp. 275-279, 1995.

[73] Y. Maday, J. Salomon, and G. Turinici, "Monotonic time-discretized schemes in quantum control," *Numerische Mathematik,* vol. 103, no. 2, pp. 323-338, 2006.

[74] D. M. Grant and R. K. Harris, "Encyclopedia of nuclear magnetic resonance, volume 9, advances in nmr," *Spectroscopy,* 1996.

[75] A. D. Bain, "Chemical exchange in NMR," *Progress in nuclear magnetic resonance spectroscopy,* vol. 43, no. 3-4, pp. 63-103, 2003.

[76] L. M. Silva, G. Elenilson Filho, A. J. Simpson, M. R. Monteiro, and T. Venâncio, "Comprehensive multiphase NMR spectroscopy: A new analytical method to study the effect of biodiesel blends on the structure of commercial rubbers," *Fuel,* vol. 166, pp. 436-445, 2016.

[77] J. Keeler, in *Understanding NMR Spectroscopy*. United kingdom: Wiley, 2002, p. 211.

[78] M. H. Levitt, "Larmor Frequency," in *Spin dynamics*. Chichester: John Wiley & Sons Ltd, 2008, pp. 29-35.

[79] F. Professor Dieter, "Spectroscopy for Physicists," in *Nuclear Magnetic Resonance*. Leipzig, 2006, ch. 4, pp. 1-29.

[80] H. Guenter, in *NMR Spectroscopy: Basic Principles, Concepts and Applications in Chemistry, 3rd Edition*: Wiley-VCH, 2013, p. 736.

[81] M. H. Levitt, *Spin dynamics: basics of nuclear magnetic resonance*. John Wiley & Sons, 2013.

[82] J. A. Koutcher and C. T. Burt, "Principles of nuclear magnetic resonance," *Journal of Nuclear Medicine,* vol. 25, no. 1, pp. 101-111, 1984.

[83] J. Keeler, "Relaxation," in *Understanding NMR spectroscopy*. Camcridge: Wiley, 2002, pp. 8-1 to 8-25.

[84] H. An and W. Lin, "Spin Density, T 1, T 2, T 2* Relaxation and Bloch Equations," *Current Protocols in Magnetic Resonance Imaging,* no. 1, pp. B3. 1.1-B3. 1.10, 2001.

[85] D. S. Wu, "Basic theory of NMR," in *1D and 2D NMR experiment methods*. Atlanta, 2011, p. 8 to 17.

[86] M. Olaf Dietrich, "Is T2 necessarily shorter than T1?," no. 2, pp. 1-4, 2003.

[87] M. H. Levitt, "Nuclear Magnetism," in *Spin dynamics*. West Sussex PO19 8SQ: John Wiley & Sons Ltd, 2008, pp. 5-59.

[88] C. Slichter, "Principles of Magnetic Resonance Springer-Verlag, Berlin," *Heidelberg, New York,* 1980.

[89] A. Abragam, *The Principles of Nuclear Magnetism*. Oxford University Press, 1961.

[90] D. C. McCain and R. J. Myers, "Spin-lattice and spin-spin relaxation times for VO2+ in aqueous solution," *The Journal of Physical Chemistry,* vol. 71, no. 1, pp. 192-200, 1967.

[91] M. H. Levitt, "Magnetism," in *Spin dynamics*. West sussex: Wiley-VCH Verlag GmbH, Boschstr. 12, D-69469 Weinheim, Germany, 2008, p. 23 to 36.

[92] D. S. Wu, "1D and 2D NMR Experiment Methods," pp. 18-27, June 2011.

[93] N. Hu, D. Wu, K. J. Cross, and D. W. Schaefer, "Structural Basis of the ^{1}H-Nuclear Magnetic Resonance Spectra of Ethanol–Water Solutions Based on Multivariate Curve Resolution Analysis of Mid-Infrared Spectra," *Applied Spectroscopy,* vol. 64, no. 3, pp. 337-342, 2010, doi: 10.1366/000370210790918373.

[94] E. Brunner, D. Freude, B. Gerstein, and H. Pfeifer, "Residual linewidths of NMR spectra of spin-12 systems under magic-angle spinning," *Journal of Magnetic Resonance (1969),* vol. 90, no. 1, pp. 90-99, 1990.

[95] H. Günther, *NMR spectroscopy: basic principles, concepts and applications in chemistry*. John Wiley & Sons, 2013.

[96] V. Mlynárik, "Introduction to nuclear magnetic resonance," *Analytical Biochemistry,* vol. 529, pp. 4-9, 2017.

[97] A. A. Pavlov *et al.*, "A Synergy and Struggle of EPR, Magnetometry and NMR: A Case Study of Magnetic Interaction Parameters in a Six-Coordinate Cobalt (II) Complex," *Inorganic Chemistry,* vol. 59, no. 15, pp. 10746-10755, 2020.

[98] R. J. Abraham and M. Mobli, "The prediction of ^{1}H NMR chemical shifts in organic compounds," *Spectroscopy Europe,* vol. 16, no. 4, pp. 16-22, 2004.

[99] J. Vaara, J. Jokisaari, R. E. Wasylishen, and D. L. Bryce, "Spin–spin coupling tensors as determined by experiment and computational chemistry," *Progress in Nuclear Magnetic Resonance Spectroscopy,* vol. 41, no. 3, pp. 233-304, 2002.

[100] H. Gunther and H. Gunther, *NMR spectroscopy: basic principles, concepts, and applications in chemistry*. John Wiley & Sons Chichester, UK, 1994.

[101] D. Marion and K. Wüthrich, "Application of phase sensitive two-dimensional correlated spectroscopy (COSY) for measurements of ^{1}H-^{1}H spin-spin coupling constants in proteins," *Biochemical and biophysical research communications,* vol. 113, no. 3, pp. 967-974, 1983.

[102] G. E. Maciel, "Line-broadening influences and line-narrowing techniques in solid state NMR," in *Magnetic Resonance*: Springer, 1984, pp. 71-110.

[103] A. A. Malär *et al.*, "Quantifying proton NMR coherent linewidth in proteins under fast MAS conditions: a second moment approach," *Physical Chemistry Chemical Physics,* vol. 21, no. 35, pp. 18850-18865, 2019.

[104] L. Qinying, L. Shiyu, L. Yongkang, and H. Xiaotao, "Pulsed-field nuclear magnetic resonance: status and prospects," *Matter and Radiation at Extremes,* vol. 6, no. 2, p. 024201, 2021.

[105] C. Eccles, "Low field NMR methods and applications," *Encyclopedia of Spectroscopy and Spectrometry,* pp. 1357-1371, 2010.

[106] J.-C. Guo, H.-Y. Zhou, J. Zeng, K.-J. Wang, J. Lai, and Y.-X. Liu, "Advances in low-field nuclear magnetic resonance (NMR) technologies applied for characterization of pore space inside rocks: a critical review," *Petroleum Science,* vol. 17, no. 5, pp. 1281-1297, 2020.

[107] C. P. Slichter, *Principles of magnetic resonance*. Springer Science & Business Media, 2013.

[108] C. Dybowski, "Zeeman Interaction in Nuclear Magnetic Resonance," *Encyclopedia of Analytical Chemistry: Applications, Theory and Instrumentation,* 2006.

[109] F. Dalitz, M. Cudaj, M. Maiwald, and G. Guthausen, "Process and reaction monitoring by low-field NMR spectroscopy," *Progress in nuclear magnetic resonance spectroscopy,* vol. 60, pp. 52-70, 2012.

[110] H. Soltner and P. Blümler, "Dipolar Halbach magnet stacks made from identically shaped permanent magnets for magnetic resonance," *Concepts in magnetic resonance part a,* vol. 36, no. 4, pp. 211-222, 2010.

[111] M. Amjadian and A. K. Agrawal, "Planar arrangement of permanent magnets in design of a magneto-solid damper by finite element method," *Journal of Intelligent Material Systems and Structures,* vol. 31, no. 7, pp. 998-1014, 2020.

[112] P. Blümler and H. Soltner, "Practical Concepts for Design, Construction and Application of Halbach Magnets in Magnetic Resonance," *Applied Magnetic Resonance,* vol. 54, no. 11, pp. 1701-1739, 2023.

[113] A. Bakenecker, J. Schumacher, P. Blümler, K. Gräfe, M. Ahlborg, and T. Buzug, "A concept for a magnetic particle imaging scanner with Halbach arrays," *Physics in Medicine & Biology,* vol. 65, no. 19, p. 195014, 2020.

[114] O. Tretiak, P. Blümler, and L. Bougas, "Variable single-axis magnetic-field generator using permanent magnets," *AIP Advances,* vol. 9, no. 11, 2019.

[115] M. L. Johns, E. O. Fridjonsson, S. J. Vogt, and A. Haber, *Mobile NMR and MRI: developments and applications*. Royal Society of Chemistry, 2015.

[116] H. Leupold, E. Potenziani II, and M. Abele, "Applications of yokeless flux confinement," *Journal of Applied Physics,* vol. 64, no. 10, pp. 5994-5996, 1988.

[117] D. Grass, J. P. Caulkins, G. Feichtinger, G. Tragler, and D. A. Behrens, "Optimal control of nonlinear processes," *Berlino: Springer,* 2008.

[118] P. de Fouquieres, S. G. Schirmer, S. J. Glaser, and I. Kuprov, "Second order gradient ascent pulse engineering," *Journal of Magnetic Resonance,* vol. 212, no. 2, pp. 412-417, 2011.

[119] O. V. Morzhin and A. N. Pechen, "Krotov method for optimal control of closed quantum systems," *Russian Mathematical Surveys,* vol. 74, no. 5, p. 851, 2019.

[120] D. D'alessandro and M. Dahleh, "Optimal control of two-level quantum systems," *IEEE Transactions on Automatic Control,* vol. 46, no. 6, pp. 866-876, 2001.

[121] R. Heule, C. Bruder, D. Burgarth, and V. M. Stojanović, "Local quantum control of Heisenberg spin chains," *Physical Review A,* vol. 82, no. 5, p. 052333, 2010.

[122] G. F. Pauli, T. Godecke, B. U. Jaki, and D. C. Lankin, "Quantitative ^{1}H NMR. Development and potential of an analytical method: an update," *Journal of natural products,* vol. 75, no. 4, pp. 834-851, 2012.

[123] H. R. Contreras and C. García, "Inter-species variability of okadaic acid group toxicity in relation to the content of fatty acids detected in different marine vectors," *Food Additives & Contaminants: Part A,* vol. 36, no. 3, pp. 464-482, 2019.

[124] M. Goerz *et al.*, "Krotov: A Python implementation of Krotov's method for quantum optimal control," *SciPost physics,* vol. 7, no. 6, p. 080, 2019.

[125] V. F. Krotov, "A technique of global bounds in optimal control theory," *Control and Cybernetics,* vol. 17, no. 3, pp. 2-3, 1988.

[126] W. Zhu and H. Rabitz, "A rapid monotonically convergent iteration algorithm for quantum optimal control over the expectation value of a positive definite operator," *The Journal of Chemical Physics,* vol. 109, no. 2, pp. 385-391, 1998.

[127] M. S. Vinding, D. L. Goodwin, I. Kuprov, and T. E. Lund, "Optimal control gradient precision trade-offs: Application to fast generation of DeepControl libraries for MRI," *Journal of Magnetic Resonance,* vol. 333, p. 107094, 2021.

[128] Y. Maday, J. Salomon, and G. Turinici, "Monotonic time-discretized schemes in quantum control," *Numerische Mathematik,* vol. 103, pp. 323-338, 2006.

[129] G. Strang, "Accurate partial difference methods I: Linear Cauchy problems," *Archive for Rational Mechanics and Analysis,* vol. 12, no. 1, pp. 392-402, 1963.

[130] N. Ramsey and E. Purcell, "Interactions between nuclear spins in molecules," *Physical Review,* vol. 85, no. 1, p. 143, 1952.

[131] A. C. Sauerwein, "Estimations of dipolar couplings in multiple-spin systems by solid state NMR," University of Southampton, 2010.

[132] T. Gullion and J. Schaefer, "Rotational-echo double-resonance NMR," *Journal of Magnetic Resonance (1969),* vol. 81, no. 1, pp. 196-200, 1989.

[133] J. R. Garbow and T. Gullion, "Improvements in REDOR NMR spectroscopy. Minimizing resonance-offset effects," *Journal of Magnetic Resonance (1969),* vol. 95, no. 2, pp. 442-445, 1991.

[134] T. M. Alam and J. E. Jenkins, "HR-MAS NMR spectroscopy in material science," *Advanced aspects of spectroscopy,* vol. 10, p. 279, 2012.

[135] J. Farjon, W. Bermel, and C. Griesinger, "Resolution enhancement in spectra of natural products dissolved in weakly orienting media with the help of ^{1}H homonuclear dipolar decoupling during acquisition: application to ^{1}H–^{13}C dipolar

couplings measurements," *Journal of Magnetic Resonance,* vol. 180, no. 1, pp. 72-82, 2006.

[136] J. Miller, D. Cory, and A. Garroway, "Multiple Pulse Line Narrowing: Approaches for Solid State NMR Imaging," *Review of Progress in Quantitative Nondestructive Evaluation,* pp. 649-654, 1992.

[137] P. Jackson and R. K. Harris, "A practical guide to combined rotation and multiple-pulse NMR spectroscopy of solids," *Magnetic Resonance in Chemistry,* vol. 26, no. 11, pp. 1003-1011, 1988.

[138] R. T. McKay, "Recent advances in solvent suppression for solution NMR: a practical reference," *Annual reports on NMR spectroscopy,* vol. 66, pp. 33-76, 2009.

[139] A. J. Simpson and S. A. Brown, "Purge NMR: effective and easy solvent suppression," *Journal of Magnetic Resonance,* vol. 175, no. 2, pp. 340-346, 2005.

[140] M. Liu, X.-a. Mao, C. Ye, H. Huang, J. K. Nicholson, and J. C. Lindon, "Improved WATERGATE pulse sequences for solvent suppression in NMR spectroscopy," *Journal of Magnetic Resonance,* vol. 132, no. 1, pp. 125-129, 1998.

[141] J. Tanner, "Pulsed field gradients for NMR spin-echo diffusion measurements," *Review of Scientific Instruments,* vol. 36, no. 8, pp. 1086-1087, 1965.

[142] M. Canton, R. Roe, S. Poigny, J.-H. Renault, and J.-M. Nuzillard, "Multiple solvent signal presaturation in 13 C NMR," 2020.

[143] J. DeRuiter, "Carboxylic acid structure and chemistry: part 1," *Principles of drug action,* vol. 1, pp. 1-10, 2005.

[144] S. J. Weininger, "Delayed reaction: The tardy embrace of physical organic chemistry by the German chemical community," *Ambix,* vol. 65, no. 1, pp. 52-75, 2018.

[145] F. B. A. Descallar and S. Matsukawa, "Change of network structure in agarose gels by aging during storage studied by NMR and electrophoresis," *Carbohydrate polymers,* vol. 245, p. 116497, 2020.

[146] M. D. Torres, N. Flórez-Fernández, and H. Domínguez, "Integral utilization of red seaweed for bioactive production," *Marine drugs,* vol. 17, no. 6, p. 314, 2019.

[147] B. Dai and S. Matsukawa, "Elucidation of gelation mechanism and molecular interactions of agarose in solution by ^{1}H NMR," *Carbohydrate Research,* vol. 365, pp. 38-45, 2013.

[148] M. D. Mitchell, H. L. Kundel, L. Axel, and P. M. Joseph, "Agarose as a tissue equivalent phantom material for NMR imaging," *Magnetic resonance imaging,* vol. 4, no. 3, pp. 263-266, 1986.

[149] H. G. Lee and M. K. Cowman, "An agarose gel electrophoretic method for analysis of hyaluronan molecular weight distribution," *Analytical biochemistry,* vol. 219, no. 2, pp. 278-287, 1994.

[150] W. P. Power, "High resolution magic angle spinning-applications to solid phase synthetic systems and other semi-solids," *ANNUAL REPORTS OF NMR SPECTROSCOPY,* vol. 51, pp. 261-296, 2003.

[151] E. Andrew, "Magic angle spinning," *International Reviews in Physical Chemistry,* vol. 1, no. 2, pp. 195-224, 1981.

[152] R. S. Macomber, "A complete introduction to modern NMR spectroscopy," *Nova York,* 1998.

[153] A. Broberg and L. Kenne, "Use of high-resolution magic angle spinning nuclear magnetic resonance spectroscopy for in situ studies of low-molecular-mass compounds in red algae," *Analytical Biochemistry,* vol. 284, no. 2, pp. 367-374, 2000.

[154] T. Polenova, R. Gupta, and A. Goldbourt, "Magic angle spinning NMR spectroscopy: a versatile technique for structural and dynamic analysis of solid-phase systems," ed: ACS Publications, 2015.

[155] J. S. Harwood and H. Mo, *Practical NMR Spectroscopy Laboratory Guide: Using Bruker Spectrometers*. Academic Press, 2015.

[156] P. Yu *et al.*, "Theoretical foundation for designing multilayer Halbach array magnets for benchtop NMR and MRI," *Journal of Magnetic Resonance,* vol. 344, p. 107322, 2022.

[157] S. Jang, S. Cha, S. Lee, B. Kim, H. Sung, and H. Cho, "Analysis of characteristic linear Halbach array," in *Proceedings of the KIEE Conference*, 2001: The Korean Institute of Electrical Engineers, pp. 892-894.

[158] S. Jang, J. Seo, and S. Choi, "Charateristics Analysis on the Field System of Halbach Array by the Permanent Magnet," in *Proceedings of the KIEE Conference*, 1997: The Korean Institute of Electrical Engineers, pp. 24-26.

[159] S. Huang, Z. H. Ren, S. Obruchkov, J. Gong, R. Dykstra, and W. Yu, "Portable low-cost MRI system based on permanent magnets/magnet arrays," *Investigative Magnetic Resonance Imaging,* vol. 23, no. 3, pp. 179-201, 2019.

[160] G. Shamuilov, "Lattices for a 4th-Generation Synchrotron Light Source," in *Journal of Physics: Conference Series*, 2018, vol. 1067, no. 3: IOP Publishing, p. 032009.

[161] T. Koppel, P. Ross, and I. Vilcane, "Shielding static magnetic fields from Magnetic Resonance Imaging units by ferromagnetic material," in *EMBEC & NBC 2017*: Springer, 2017, pp. 743-746.

[162] P. Nath, C. Chandrana, D. Dunkerley, J. Neal, and D. Platts, "The “Shim-a-ring” magnet: Configurable static magnetic fields using a ring magnet with a concentric ferromagnetic shim," *Applied Physics Letters,* vol. 102, no. 20, p. 202409, 2013.

[163] J.-M. Wu, Z. Xu, P. Guo, J.-F. Qi, and Y.-C. He, "Shim coil design for Halbach magnet by equivalent magnetic dipole method," *Chinese Physics B,* vol. 27, no. 10, p. 104101, 2018.

[164] Y. Xu, F. Wang, Y. Wang, P. Yu, J. Zhang, and X. Yang, "Active shim coils design for Halbach magnet based on inverse boundary element method," *Magnetic Resonance Letters,* 2022.

[165] B. De Vos, P. Fuchs, T. O'Reilly, A. Webb, and R. Remis, "Gradient coil design and realization for a Halbach-based MRI system," *IEEE Transactions on Magnetics,* vol. 56, no. 3, pp. 1-8, 2020.

[166] S. Ghosh, D. Teweldebrhan, J. Morales, J. Garay, and A. Balandin, "Thermal properties of the optically transparent pore-free nanostructured yttria-stabilized zirconia," *Journal of applied physics,* vol. 106, no. 11, p. 113507, 2009.

[167] M. Gupta, C. Safvan, K. Singh, D. Lobiyal, P. Yadav, and S. Singh, "Radio Frequency Planar Coil-Based On-Chip Probe for Portable Nuclear Magnetic Resonance," *IEEE Sensors Journal,* vol. 19, no. 7, pp. 2500-2508, 2018.

[168] F. Alimenti, P. Mezzanotte, L. Roselli, and R. Sorrentino, "Modeling and characterization of the bonding-wire interconnection," *IEEE Transactions on Microwave Theory and Techniques,* vol. 49, no. 1, pp. 142-150, 2001.

[169] I. Ndip, A. Öz, H. Reichl, K.-D. Lang, and H. Henke, "Analytical models for calculating the inductances of bond wires in dependence on their shapes, bonding parameters, and materials," *IEEE Transactions on Electromagnetic Compatibility,* vol. 57, no. 2, pp. 241-249, 2014.

[170] M. E. Lacey, R. Subramanian, D. L. Olson, A. G. Webb, and J. V. Sweedler, "High-resolution NMR spectroscopy of sample volumes from 1 nL to 10 μL," *Chemical reviews,* vol. 99, no. 10, pp. 3133-3152, 1999.

[171] D. I. Hoult and R. Richards, "The signal-to-noise ratio of the nuclear magnetic resonance experiment," *Journal of Magnetic Resonance (1969),* vol. 24, no. 1, pp. 71-85, 1976.

[172] P. Lepucki, A. P. Dioguardi, D. Karnaushenko, O. G. Schmidt, and H.-J. Grafe, "The normalized limit of detection in NMR spectroscopy," *Journal of Magnetic Resonance,* vol. 332, p. 107077, 2021.

[173] S. Machnes *et al.*, "Comparing, optimizing, and benchmarking quantum-control algorithms in a unifying programming framework," *Physical Review A,* vol. 84, no. 2, p. 022305, 2011.

[174] D. J. Tannor, R. Kosloff, and S. A. Rice, "Coherent pulse sequence induced control of selectivity of reactions: Exact quantum mechanical calculations," *The Journal of chemical physics,* vol. 85, no. 10, pp. 5805-5820, 1986.

[175] I. Jum'h, A. Telfah, J. Lambert, M. Gogiashvili, H. Al-Taani, and R. Hergenröder, "^{13}C and ^{1}H NMR measurements to investigate the kinetics and the mechanism of acetic acid (CH3CO2H) ionization as a model for organic acid dissociation dynamics for polymeric membrane water filtration," *Journal of Molecular Liquids,* vol. 227, pp. 106-113, 2017.

[176] J. Friedrich, S. Davies, and R. Freeman, "Shaped selective pulses for coherence-transfer experiments," *Journal of Magnetic Resonance (1969),* vol. 75, no. 2, pp. 390-395, 1987.

[177] R. H. Simoyi, K. Streete, C. Mundoma, and R. Olojo, "Complex kinetics in the reaction of taurine with aqueous bromine and acidic bromate: a possible cytoprotective role against hypobromous acid," *South African Journal of Chemistry,* vol. 55, 2002.

[178] D. S. Wishart *et al.*, "HMDB 5.0: the human metabolome database for 2022," *Nucleic Acids Research,* vol. 50, no. D1, pp. D622-D631, 2022.

[179] C. A. Meriles, D. Sakellariou, H. Heise, A. J. Moulé, and A. Pines, "Approach to high-resolution ex situ NMR spectroscopy," *Science,* vol. 293, no. 5527, pp. 82-85, 2001.

[180] J. Perlo *et al.*, "High-resolution NMR spectroscopy with a portable single-sided sensor," *Science,* vol. 308, no. 5726, pp. 1279-1279, 2005.

[181] M. Guéron, P. Plateau, and M. Decorps, "Solvent signal suppression in NMR," *Progress in nuclear magnetic resonance spectroscopy,* vol. 23, no. 2, pp. 135-209, 1991.

[182] M. Canton, R. Roe, S. Poigny, J.-H. Renault, and J.-M. Nuzillard, "Multiple solvent signal presaturation and decoupling artifact removal in ^{13}C {^{1}H} nuclear magnetic resonance," *Magnetic Resonance,* vol. 1, no. 2, pp. 155-164, 2020.

[183] L. M. Botana, *Seafood and freshwater toxins: pharmacology, physiology, and detection*. Crc Press, 2014.

[184] A. S. Altieri and R. A. Byrd, "Randomization approach to water suppression in multidimensional NMR using pulsed field gradients," *Journal of Magnetic Resonance, Series B,* vol. 107, no. 3, pp. 260-266, 1995.

[185] O. Anisimov, A. Nikitaev, K. I. Zamaraev, and Y. N. Molin, "Separation of exchange and dipole-dipole broadening on the basis op viscosity changes in ESR spectra," *Theoretical and Experimental Chemistry,* vol. 7, pp. 556-559, 1974.

[186] M. E. H. El Nokab and P. C. Van Der Wel, "Use of solid-state NMR spectroscopy for investigating polysaccharide-based hydrogels: A review," *Carbohydrate polymers,* vol. 240, p. 116276, 2020.

[187] L. Calucci and C. A. Veracini, "Liquid Crystals and Liquid Crystal Solutions Studied by NMR," in *Encyclopedia of Spectroscopy and Spectrometry*: Academic Press, 1999, pp. 1179-1186.